

TECHNISCHE UNIVERSITÄT
CHEMNITZ

**HED-TIE: A wafer-scale approach for fabricating hybrid
electronic devices with trench isolated electrodes and its
application in sensing devices**

Dissertation

Von der Fakultät für Naturwissenschaften der Technischen Universität Chemnitz genehmigte
Dissertation zur Erlangung des akademischen Grades

Doctor rerum naturalium

(Dr. rer. Nat.)

von M. Sc. Sreetama Banerjee

geboren am 05. September 1986 in Indien

Tag der Einreichung: 12. Dezember 2017

Gutachter:

Prof. Dr. Dr. h.c. D. R. T. Zahn

Prof. Dr. L. Hueso

Tag der Verteidigung: 4. Februar 2019

Dedicated to

Maa, Baba, Didi and Sandeep

Table of Contents

Bibliografische Beschreibung	1
Chapter 1. Introduction	3
1.1 Organic-inorganic hybrid electronics	4
1.2 Inorganic semiconductors versus organic semiconductors	5
1.3 Electronic properties of a molecular layer	5
1.4 Vertical HEDs and planar HEDs	6
Chapter 2. Wafer-scale fabrication approach for planar HED-TIEs	8
2.1 Overview of nano-patterning techniques	8
(a) Electron beam lithography (EBL)	8
(b) Nanostencil lithography (NSL)	8
(c) Nanoimprint lithography (NIL)	9
2.2 Fabrication of planar organic-inorganic HED-TIEs	12
2.2.1 Trench refill approach for fabricating HED-TIEs	12
2.2.1.1 Deposition of the trench refill layer	15
2.2.1.2 Deposition of the organic channel material	16
(a) HED-TIE with thermally evaporated organic channel	16
(b) HED-TIE with solution processed organic channel	18
2.2.2 Spacer approach for fabricating HED-TIEs	21
2.2.2.1 Deposition of the isolation layer	23
2.3 Characterization techniques	26
(a) Electrical characterization	26
(b) Raman spectroscopy	26
(c) Photoluminescence spectroscopy	27

2.4	Summary and outlook	27
Chapter 3.	Electrical characterization of HED-TIEs	29
3.1	Theoretical background	29
3.1.1	Space charge limited current (SCLC) conduction mechanism.....	29
3.2	Experimental details	32
3.3	Results and discussions	34
3.4	Summary and outlook	40
Chapter 4.	Application of HED-TIEs as optical sensors	41
4.1	Photosensing properties of TIPS-pentacene based HED-TIEs	41
4.1.1	Theoretical background	41
4.1.2	Experimental details	43
4.1.3	Results and discussions	44
4.1.4	Summary and outlook	49
4.2	Photosensing properties of TIPS-pentacene based HED-TIEs with Au nanoparticles in the channel matrix	50
4.2.1	Theoretical background	50
4.2.2	Experimental details	51
4.2.3	Results and discussions	52
4.2.4	Summary and outlook	59
Chapter 5.	Application of HED-TIE devices as magnetoresistive sensors.....	61
5.1	Theoretical background	61
5.1.1.	Organic spintronics	61
5.1.2	Mechanisms of organic magnetoresistance (OMAR)	65
	(a) Bipolaron model	68

(b) Electron-hole (e-h) pair model	69
(c) Exciton–charge interaction model	70
5.2. OMAR measurements on TIPS-pentacene OFETs and HED-TIEs	71
5.2.1 Experimental details	71
5.3 Results and discussions	73
5.4 Summary and outlook	79
Chapter 6. Summary and outlook	81
References	86
List of Figures	97
List of Tables	103
List of Abbreviations	104
Acknowledgements	106
List of Publications	108
List of Conference Presentations and Posters	109
Selbstständigkeitserklärung	111
Curriculum Vitae	112

Bibliografische Beschreibung

M. Sc. Sreetama Banerjee

HED-TIE: a wafer-scale approach for fabricating hybrid electronic devices with trench isolated electrodes and its application in sensing devices

Technische Universität Chemnitz

Dissertation (in englischer Sprache), 2017

Die organisch-anorganische Hybridelektronik bietet verschiedene Möglichkeiten zur Entwicklung neuartiger Bauelemente, welche die Vorteile von organischen und anorganischen Halbleitern vereinen. Planare Bauelemente werden typischerweise mittels Schattenmasken-basierter Strukturierung hergestellt. Ein Grund hierfür ist die Empfindlichkeit organischer Halbleiter gegenüber Ultraviolettem Licht und Lösungsmitteln, welche in den Standard-Photolithographieprozessen eingesetzt werden. Die Schattenmasken-Strukturierung führt allerdings zu Bauelementen mit kleinsten Abmessungen im Mikrometerbereich. Für die Reduzierung der Kanalabmessungen von planaren organisch-anorganischen Hybridbauelementen unterhalb eines Mikrometers ist die Elektronenstrahlolithographie die am häufigsten verwendete Technik. Aufgrund des hohen Kosten- und Zeitaufwandes ist es nicht möglich, diese Technik für Wafermaßstab-Herstellung in der industriellen Anwendung einzusetzen.

In dieser Arbeit wird eine alternative Technologie zur Herstellung von planaren Bauelementen mit isolierten Grabenelektroden und Kanalabmessungen von wenigen Hundert Nanometer bis unter 100 nm vorgestellt. Gräben kleiner als ein Mikrometer werden zunächst auf Silizium-Substraten strukturiert und anschließend mit einer isolierenden SiO_2 Schicht aufgefüllt. Diese hilft dabei die gewünschten Elektrodenabstände, also die gewünschte Kanallänge, zu erreichen.

Die Flexibilität des neuen Herstellungsverfahrens ermöglicht es nicht nur verschiedenen Kanallängen und Bauelement-Geometrie, sondern auch die Verwendung verschiedener Materialien für Elektroden und organischen Kanäle. Dies wiederum ermöglicht eine Vielfalt von potentiellen Anwendungen der hybriden Bauelemente. In dieser Arbeit wurde 6,13-bis (triisopropylsilylethynyl)-Pentacen (TIPS-Pentacen) Lösung und metallfreie Phthalocyanin als organisches Material verwendet und als Elektrodenmaterial diente Gold. Die entstandenen auf TIPS-Pentacen-Lösung

basierenden planaren hybriden Bauelemente wurden für potentielle Anwendungen als optische sowie magnetoresistive Sensoren getestet.

Schlagwörter:

hybride Bauelemente, planare Bauelemente, Kanalabmessungen unter 100 nm, UV-lithographie, Grabenelektroden, TIPS-Pentacen Lösung, metallfreie Phthalocyanin, optische Sensoren, magnetische Sensoren.

Chapter 1

Introduction

This dissertation focuses on the development of a new technique for fabrication of planar hybrid electronic devices with electrode gap dimensions of ~ 100 nm using conventional UV-lithography (365 nm). In standard microtechnology wafer processing, depending on the UV wavelength used for photolithography, the minimum achievable electrode gap dimension fabricated by conventional UV-lithography are limited to 800 nm to 1 μm approximately. Usually for fabrication of patterns below 1 μm dimensions, various alternative patterning techniques are used^{1,2,3}. The most commonly used technique is electron beam lithography which is an expensive and time consuming method, making it unsuitable for industrial applications^{1,4}.

In this dissertation, an alternative technique for fabrication of electrode gaps down to ~ 100 nm is demonstrated by using devices with trench isolated electrodes. Chapter 1 introduces the topic of hybrid electronics in general and discusses the various possible applications of it. Some basic properties of organic semiconductors are also discussed in this chapter. It also presents the two different types of device architectures which are commonly used for hybrid electronic devices. Chapter 2 of this dissertation focuses on the fabrication technologies used for the planar *hybrid electronic devices with trench isolated electrodes* or in short, the planar HED-TIEs. Chapter 3 discusses the electronic transport properties of the HED-TIEs. To demonstrate the compatibility of the technology with both thermally evaporated and solution processed organic channel materials, the electrical transport properties of both types of devices are discussed. For this purpose, thermally evaporated metal free phthalocyanine (H_2Pc) based HED-TIEs and solution processed 6,13-bis(triisopropylsilylethynyl) pentacene or commonly known as TIPS-pentacene based HED-TIEs are fabricated and characterized. Following this, in chapter 4 and chapter 5, two possible applications of the HED-TIEs are demonstrated. As TIPS-pentacene is an air-stable photosensitive material^{5,6,7}, the first possible application of HED-TIEs is demonstrated as light sensing devices. Chapter 4 discusses various results obtained from the light sensing experiments of the TIPS-pentacene based HED-TIEs. The light sensing properties of these devices are tuned further by incorporating metal nanoparticles in the TIPS-pentacene matrix. Chapter 5 discusses the possibility of using HED-TIEs as magnetoresistive sensors.

For the first time, organic magnetoresistance or OMAR is demonstrated in solution processed small molecule based devices, measured at room temperature and under ambient conditions. Solution processed TIPS-pentacene based HED-TIEs, same as those used for the light sensing applications, are used for this purpose. The HED-TIEs are also compared with commercial bottom contact organic field effect transistors (OFETs) to demonstrate the advantages of reducing the electrode gap dimensions in HED-TIEs compared to conventional planar devices. Chapter 6 summarizes the work done in this dissertation and gives an outlook towards the possibilities of further research work.

1.1 Organic-inorganic hybrid electronics

Rapid development of various electronic devices has drastically changed our daily lives over the last sixty years. These electronic devices were based on conventional inorganic semiconductors like Si, GaAs, *etc.*^{8,9,10,11}. Though organic semiconductors have been investigated since the 1940s, it failed to play an important role in industrial applications until very recently. In 1948, thermally activated conductivity in metal free and copper phthalocyanines were demonstrated¹². Following this discovery, electroluminescence in organic molecular crystals were discovered^{13,14}. However, these devices had drawbacks of high operating voltage, low output and poor stability, making it unsuitable for practical applications. Since then various research areas ranging from new material synthesis, device design, fabrication/deposition methods, device modelling, up to possibility of numerous application areas of these devices, have widely been investigated. The field of organic-inorganic hybrid electronics, based on either small molecules or conjugated polymers^{15,16}, has come a long way in the past few decades. The tailorability of the chemical structure of organic molecules according to device requirements along with their light weight already yielded to the breakthrough of organic light emitting diodes (OLEDs), and still leave open possibilities of realizing novel device concepts. Remarkable improvements in device performance and stability have also been demonstrated in organic field effect transistors (OFETs)^{17,18}, organic photovoltaic devices (OPVs)^{19,20}, memory devices^{21,22} or even various sensing devices^{23,24}. Properties of organic materials were also explored for various spintronic device applications¹. Presently, other application areas like wearable electronics, smart textiles, various health monitoring devices are also gaining more and more research interests^{25,26,27,28}, and perhaps awaits a great future in the commercial world.

1.2 Inorganic semiconductors versus organic semiconductors

One reason for the scientific charm of the hybrid electronic devices (HEDs) lies in the complementarity of the electronic and structural properties of the organic or inorganic materials, which offers opportunities for novel functions that are not easily obtainable with either organic or inorganic materials individually. Compared to inorganic semiconductors, organic semiconductors offer various advantages such as lower production costs, flexibility and low weight^{29,30}. These advantages make it ideal for various commercial applications. Another reason for the wide interest in HEDs relates to the processability of the organic/inorganic materials: inorganic materials (semiconductors, metals) possess robustness and are mostly compatible with standard microtechnology processing techniques, while organic semiconductors (OSCs) can easily be deposited as thin films by low temperature thermal sublimation or even solution processing¹⁵.

If the electronic state configurations of organic and inorganic semiconductors are considered, there is a significant difference between these two types of materials. Inorganic semiconductors are formed by a continuum of states and electrons are delocalized within the bands, whereas organic semiconductors are composed by discrete energy levels. This energy level is associated to a molecular orbital that can be strongly localized on a group or bond of the molecule, or delocalized over an entire molecule. These two orbitals that are involved in the charge transport are known as the "Highest Occupied Molecular Orbital" (HOMO) and the "Lowest Unoccupied Molecular Orbital" (LUMO) that are separated by an energy gap³¹. These orbitals can be compared to the conventional valence band and conduction band of inorganic semiconductors. In the case of inorganic materials, the electrons are delocalized and give rise to bands, which is not the case in a molecule.

1.3 Electronic properties of a molecular layer

Molecules can be arranged in amorphous, polycrystalline or single crystalline phase depending on the deposition conditions of the molecular film. In a thin layer, the molecules interact with each other through Van der Waals interactions and this is responsible for the layer cohesion. Van der Waals forces that exist between molecules are weaker compared to the covalent or ionic bonds in inorganic materials. This is the main reason behind the less rigidity of organic molecules in comparison with inorganic materials. Additionally, the overlap between orbitals in adjacent molecules is often

weak and it resists the delocalization of electrons on other molecules. Depending on the orbital overlapping there can be two types of electronic transport in molecules: (i) band transport when the overlap between π -orbitals is strong enough to allow the delocalization of charges in an energy band formed by a quasi-continuum of states, (ii) hopping transport where the charges jump from one localized state of a molecule to another to form carrier conduction³¹. Figure 1.1 represents the mechanism of band transport and the hopping transport of charge carriers.

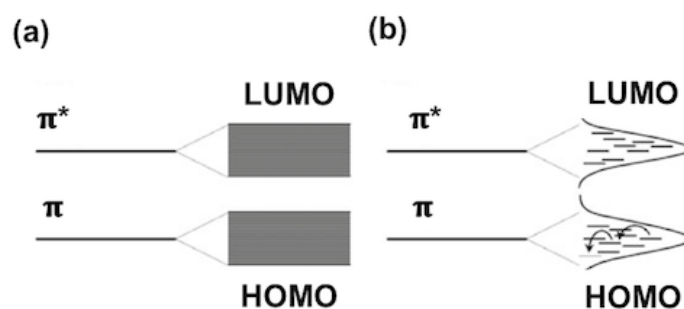


Figure 1.1 (a) Representation of the structure for band transport. If the overlap between molecules is strong enough, the overlap of bonding and anti-bonding π orbitals leads to the formation of energy bands formed by a quasi-continuum of states. (b) Representation of the structure for hopping transport. In an amorphous material, disorder leads to a dispersion of localized states. Transport occurs by hopping and it is assisted by phonons. Figure adapted from ref.³¹.

The weak Van der Waals interactions result in a charge transport in the bulk material mainly based on charge hopping, leading to a lower mobility of the organic molecules compared to inorganic materials.

1.4 Vertical HEDs and planar HEDs

There are two types of organic–inorganic HED architectures which have been described in the literature so far: (i) the vertical device architecture and (ii) the planar or lateral device architecture³². The vertical and planar terminology originates from the direction of the carrier transport with respect to the electrodes. OLEDs or OPV devices mostly use the vertical type of device^{19,33} architecture, while OFETs or organic thin film transistors (OTFTs)^{5,34} are the most common example for planar type hybrid devices. Vertical type HEDs offer the advantage of defining the device channel length by controlling the thickness of the active organic layer with an accuracy specific to the deposition method used. These devices are expected to perform at high speed for low

applied voltages due to the channel length dimensions in the range of a few nm to a few hundreds of nm. Another advantage of vertical HEDs is the possibility of depositing two different metals for the different electrodes which is common practice in various applications³⁵. However, common deposition techniques for the metal electrode layers, such as sputtering, often damage the molecular layers^{36,37}.

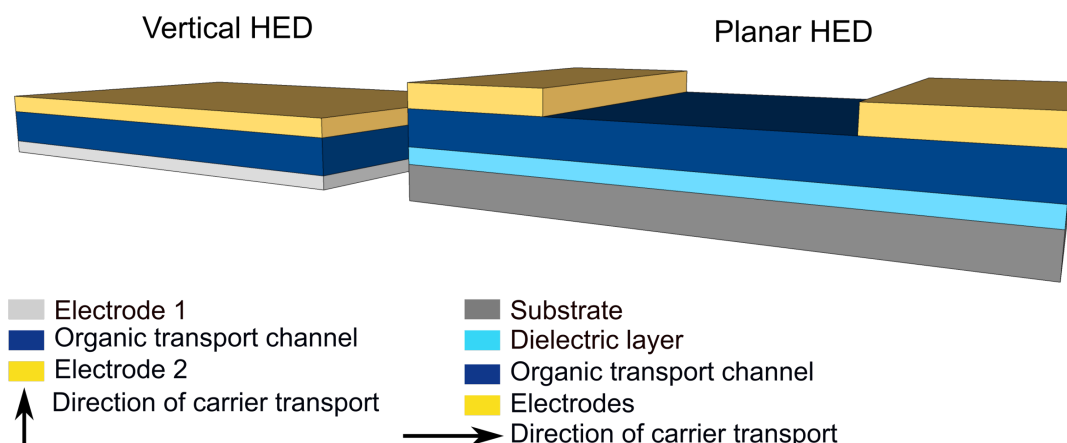


Figure 1.2 Schematic diagram of vertical and planar type hybrid electronic device structures.

Additionally, the metal tends to penetrate through pinholes and goes into the organic layers, shorting the device electrodes. Planar HEDs are mostly fabricated using shadow mask based patterning owing to the fragility of OSCs to standard photolithography processes. This procedure results in devices with larger active areas³⁸. Figure 1.2 shows schematic diagram of basic device structures of planar and vertical HEDs. One main advantage of planar HEDs is the possibility of fabricating three terminal transistor devices or fabricating sensors where the active channel of the device is fully accessible from the top^{23,39}. The various possibilities of fabricating planar hybrid devices and their associated advantages or disadvantages will be discussed in detail in the next chapter.

Chapter 2

Wafer-scale fabrication approach for planar HED-TIEs

2.1 Overview of nano-patterning techniques

In the previous chapter, we discussed about the two types of hybrid electronic device architectures reported so far in the literature. As already mentioned, in the vertical HEDs, it is possible to control the channel length dimensions by various deposition techniques and hence this can go down to few nanometres. On the other hand, planar HEDs are mostly fabricated using shadow mask based patterning due to fragility of OSCs to standard photolithography processes using UV-light. The usage of shadow masks results in devices with at least μm -large active areas³⁸. In this chapter, at first a few alternatives to shadow mask technique which have already been tested for down-scaling the channel dimension of planar HEDs will be presented. In the following section, the development of the technology for fabricating HED-TIEs achieved in this work, and its associated advantages over the other technologies reported in literature will be discussed. A part of the results discussed in this chapter was published in ref.⁴⁰.

(a) Electron beam lithography (EBL)

The most commonly used technique for patterning planar HEDs with sub-micron channel dimensions is the electron beam lithography (EBL)^{1,4}. In EBL, an electron beam scans across the whole desired pattern pixel-by-pixel. This considerably increases the exposure time compared to photolithography, where the entire pattern is exposed at once using a mask. The high maintenance costs along with the long exposure times make EBL difficult to implement in wafer-scale fabrication for industrial applications.

(b) Nanostencil lithography (NSL)

Nanostencil lithography or NSL was introduced as an alternative technique to EBL and it uses a silicon nitride shadow mask patterned by EBL within a complex process flow^{2,3}. For the nanostructuring using NSL, full wafer stencils can be used. A double sided polished Si wafer is first cleaned, and then a low pressure chemical vapour deposition (LPCVD) of a slightly strained silicon nitride (SiN) layer is carried out with a thickness of 100 nm to 500 nm. The thickness of the layer depends on the particular

application and the design that is being targeted. The optimum value of the SiN layer thickness is a trade-off between the mechanical stability of the membrane and the smallest aperture size. On one hand, the thicker the SiN layer, the larger deformations it can sustain. On the other hand, the aspect ratio of the SiN membrane thickness/aperture width needs to be ≤ 2 due to fabrication restrictions², which means that in order to have small patterns, thin membranes are required. This SiN layer is deposited on both sides of the wafer. Following this, a lithography step is performed on the front-side of the wafer via EBL, using an electron-sensitive resist. Then, the SiN layer is patterned using dry etching. Subsequently, another lithography step is performed on the backside of the wafer using UV-lithography to define the windows for KOH bulk micromachining on the backside to release the patterned membranes from the wafer. The fabricated stencil is then used for patterning structures. The figure 2.1 shows the simplified process flow for nanostencil fabrication and the use of the nanostencils for fabrication of nanostructured patterns.

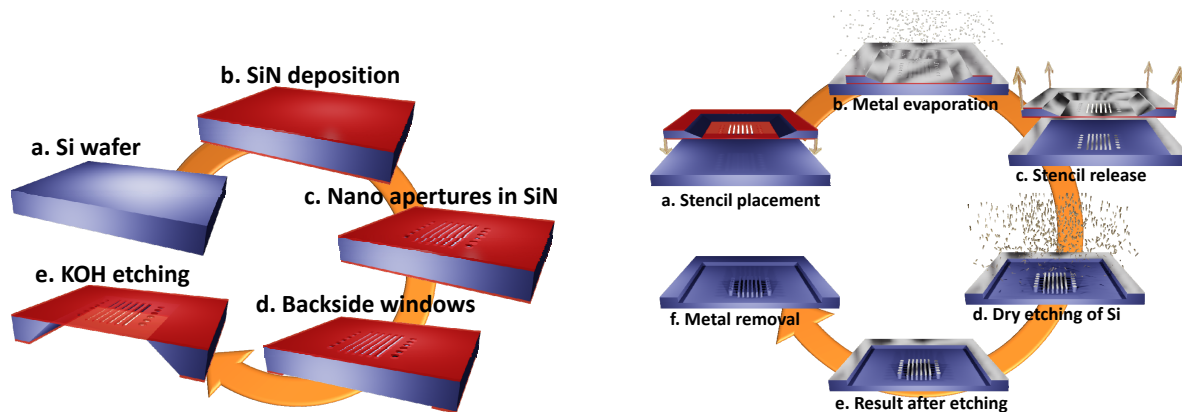


Figure 2.1 Schematic of the fabrication process flow for fabricating nanostencils and how the nanostencil is used for fabricating nanostructured patterns on substrates. Figure taken from ref.².

(c) Nanoimprint lithography (NIL)

Nanoimprint lithography or NIL is another commonly used technique that can produce high-resolution structures with dimensions in the sub- μm range by using polymer stamps^{2,41}. This technique can also be applied on a wafer level. The fabrication of the NIL polymer stamp itself, however, uses complex and expensive processes like EBL, NSL, or ion beam lithography^{2,42,43}, which still makes the overall process expensive. The NIL process is a mechanical replication process where surface released from the template are embossed into a thin layer on the substrate. In principle, there are two types of NIL. One is based on thermoplastic polymers and the second one is based on

UV-curable polymers. The NIL process and imprint instrument are conceptually very simple, but allow extremely good resolution and a relatively fast replication of the patterns. Thermal-NIL, as illustrated in figure 2.2, was the original version of NIL. It is based on the use of a layer of thermoplastic polymer, spin coated on a substrate. The thermoplastic polymer is heated above the glass transition point of the polymer, and then the heated template is brought into contact with the thermoplastic polymer. Once the polymer fills up all the cavities of the template, the substrate and the template are cooled down and the template is separated from the substrate. A negative replica of the template is created on the polymer. In order to use the imprinted polymer for pattern transfer to other layers on the substrate, polymer left on the indented areas is removed.

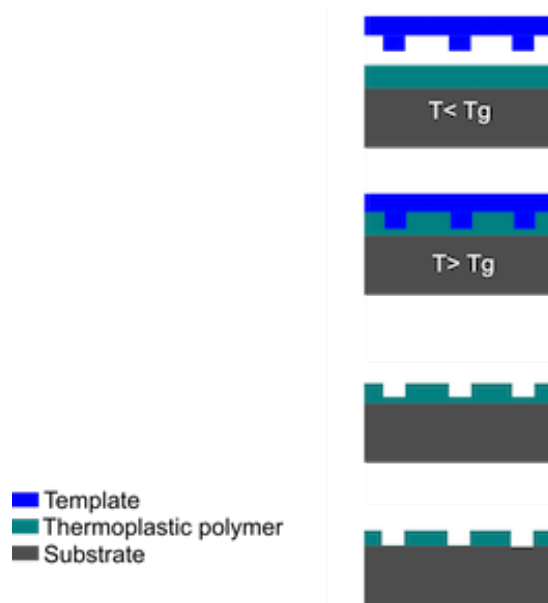


Figure 2.2 Schematic of thermal nanoimprint lithography process. T_g denotes the glass transition temperature of the thermoplastic polymer.

A few other interesting approaches have been shown to reach sub-micron electrode patterning, but their implementation has not yet been extended to the wafer-scale fabrication. For example, Min *et al.*⁴⁴ made use of organic nanowire printing for producing the organic channel, while Grünewald *et al.*⁴⁵ proposed a shadow evaporation technique to fabricate organic–inorganic planar HEDs for spintronic applications. Nevertheless, all these technologies do have their associated drawbacks. There is, therefore, still demand for the development of new, wafer-level technologies for the fabrication of planar HEDs.

In the frames of this work, the trench isolated electrode (TIE) technology as a wafer-scale approach for the fabrication of planar hybrid devices with an electrode distance down to ~ 100 nm was developed. This TIE technology is inspired from the process

flow that has been successfully implemented in the fabrication of MEMS or microelectromechanical systems^{46,47}. In the first part of the fabrication process flow, the “trench refill approach” will be discussed. In the next step, an additional spacer layer was introduced in the fabrication process flow for producing trenches with more controlled and sharper geometry. This modified technology was named as the “spacer approach”. Figure 2.3 shows the device architecture of a conventional planar HED and a HED-TIE. Both types of devices are patterned by photolithography. In conventional planar device, the channel length is defined by the photolithography technique whereas in HED-TIE the final channel length is defined by the thickness of the deposited isolation layer. Development of this technology was started as a task for a master’s thesis and various optimization steps for development of the technology can be found in ref.⁴⁸. In the duration of this dissertation work, some necessary changes in the fabrication flow were implemented for improving the device geometry and the electrical properties of the devices.

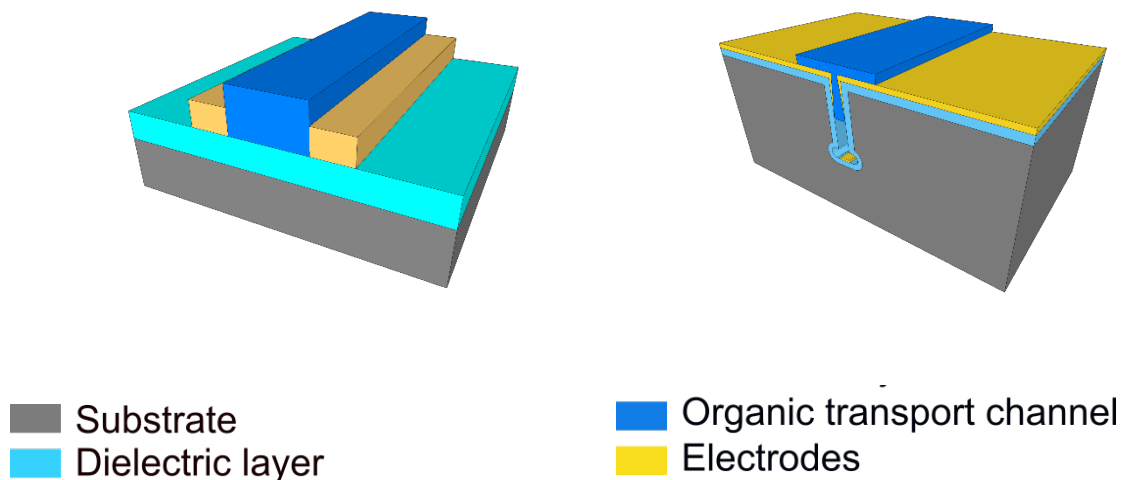


Figure 2.3 Schematic representation of the device architectures of conventional planar device (left) and HED-TIE (right).

The key aspects of the proposed technology are as follows: (i) the TIE process flow is compatible with standard silicon technology and can be scaled up for high-volume manufacturing on 200 mm or 300 mm wafers; (ii) the device geometry is not limited to two-terminal architecture, but can easily be varied to multiple electrodes design with fully tuneable channel dimensions in the range of 100 nm or even below, and various materials, including ferromagnetic metals or oxides can be used for the electrode layer; (iii) the HEDs fabrication is compatible with various deposition techniques of the active

transport channel, such as solution processing techniques (inkjet printing, spin-coating, drop-coating, or the ‘doctor blade’ method), stamping or vacuum deposition by thermal evaporation; (iv) the HEDs fabrication is not restricted to organic channels: other materials such as polymers, oxides, or even 2D materials (graphene, MoS₂, *etc.*) can be implemented in the highly flexible fabrication process flow. In addition to providing a platform for fundamental investigations of nanoscale transport mechanisms with systematic variation of the transport channel length on a single chip, the HED-TIE technology offers full accessibility of the active transport channel to external stimuli such as light or gases. This type of device structures can find a wide range of applications in spintronic devices, waveguides, photodetectors, or gas sensors, depending on the channel material and/or in combination with the electrode material used in the devices. As this work focuses on developing a new fabrication technology for planar hybrid devices, it is important to check the compatibility of the technology with the standard deposition techniques available for organic molecules. It is demonstrated that the HED-TIEs are suitable for both solution processing of organic molecules as well as thermal evaporation of organic molecules in vacuum. For this purpose, thermally evaporated metal free phthalocyanine (H₂Pc) based HED-TIEs and solution processed 6,13-bis(triisopropylsilylethynyl)pentacene or commonly known as TIPS-pentacene based HED-TIEs are fabricated and characterized. The device characterizations and the possible applications of the fabricated devices will be discussed in the following chapters.

2.2 Fabrication of planar organic-inorganic HED-TIEs

2.2.1 Trench refill approach for fabricating HED-TIEs

Figure 2.4 shows the fabrication process flow of the HED-TIEs using the “trench refill approach”. (a) The process starts with cleaning the 100 mm n-type (100) silicon wafer with a specific resistance of 6–7 Ω cm. (b) Thermal oxidation of the wafer is performed to form a 500 nm SiO₂ layer which acts as the hard mask layer. (c–d) Sub-micron trenches with dimensions ranging from 850 nm to 1050 nm are patterned on the hard mask layer using standard photolithography, and the SiO₂ layer is etched away using reactive ion etching. (e) Deep reactive ion etching of silicon with an etch depth of 4 μm is carried out in a Surface Technology Systems (STS) multiplex inductively coupled plasma system to create the trenches. For this step, a time multiplexed reactive ion etching was used by supplying SF₆ and C₄F₈ in an alternating way. The SF₆ chemically

etches away the silicon whereas the C_4F_8 forms a chemically inactive polymer deposited on the surface. Due to the highly directional nature of the ions, the SF_6 can only attack the bottom surface, whereas the sidewalls are protected by the polymer⁴⁹. This alternate etching and passivation process introduces small scallops on the sidewalls. (f) Deposition of a 200 nm thick SiO_x layer is then carried out by plasma enhanced chemical vapour deposition (PECVD). This layer protects the vertical sidewalls of the trenches in the following step. (g) The deposited SiO_x layer is then removed from the bottom of the trenches by a highly anisotropic etch step using a reactive ion etching process based on CF_4 . This step allows for isotropic etching of the silicon substrate in the following step while the vertical sidewalls are still protected by the SiO_x layer. (h) Isotropic etching of Si is carried out using a SF_6/O_2 plasma for 20s. This forms a cavity at the bottom of the trench, which is needed for electrical isolation of the electrodes. (i) The SiO_x layer which was used to protect the sidewalls of the trench is then completely removed by hydrofluoric acid (HF). (j) Deposition of an 800 nm SiO_x layer by LPCVD is then carried out. This SiO_x layer reduces the device channel dimensions by refilling the trenches partially, and also serves as the electrode isolation layer.

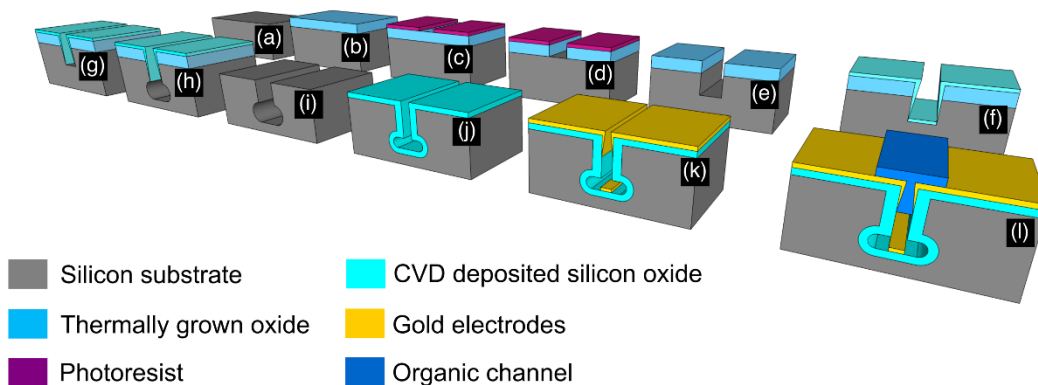


Figure 2.4 Schematic representation of the fabrication process flow of the HED-TIEs using “trench refill approach”. Figure taken from ref.⁴⁰.

As can be seen in figure 2.5, the thickness of the LPCVD SiO_x layer on the electrode area is much larger than that in the trench opening. This produces a ‘cone’-shaped trench opening at the top part of the trench. The thickness of 800 nm was chosen to obtain the desired electrode gap dimensions without closing the trench. (k) Sputtering of a 50 nm thick gold layer is then carried out to form the device electrodes along with a 10 nm thick Cr adhesion layer. (l) Finally, the wafer is diced into 1 cm × 1 cm chips followed by the organic channel formation.

It should be emphasized that the developed technology offers the possibility of tuning the electrode gaps to reach any desired channel dimension, even below 100 nm, by tuning the thickness of the refilling SiO_x layer and/or the metal layer. It should be noted, however, that during sputtering the metal gets deposited partially on the sidewalls of the trench and also at the bottom of the trench. As long as the deposited metal layers on the sidewalls do not touch each other, or the metal layer on the sidewalls are properly isolated by the cavity at the bottom of the trench, the metal layer thickness can be tuned to the desired range.

The widths of the electrical transport channels are kept to either 30 μm or 40 μm. Depending on the initial trench dimensions obtained from photolithography, which is varied from 850 nm to 1050 nm. Device structures with electrical transport channel lengths of 120 nm, 170 nm, 210 nm, 250 nm, and 300 nm were fabricated. The channel dimensions can have variations of ±10 nm due to aspect ratio-dependent variation in the fabrication processes (such as etching or deposition), while the measurement error from scanning electron microscopy (SEM) imaging itself is ±3%. For simplicity, the channel dimensions will be given without error bars throughout the dissertation.

Up to the point of deposition of the metal layer, the fabrication process described is based on standard wafer-level silicon processing technology and optimized for 100 mm wafer fabrication. The organic channel formation for the devices described in this dissertation was done on diced chips from the fabricated wafer for both drop-coated and evaporated channel materials. This was done for making it compatible with the measurement set-up used for further experiments. Availing options like inkjet printing of organic molecules on the channel area can take this technology a step further and make it a complete wafer-level fabrication process for planar hybrid devices. Spin-coating can also be an alternative for coating the whole wafer uniformly with organic molecules.

Before the deposition of the organic material, the electrical isolation of every single device was checked to ensure that the current obtained during the electrical characterization was indeed from the channel material but not from the metal sidewalls touching each other and creating shorted electrodes. Typically, more than 97% of the tested devices on a 100 mm wafer were properly isolated.

Figure 2.5 (a) shows the cross-sectional SEM (XSEM) image of a fabricated HED-TIE with solution processed TIPS-pentacene as channel material. Figure 2.5 (b) shows the cross-sectional SEM image of a fabricated HED-TIE with evaporated metal free

phthalocyanine (H_2Pc) as channel material. The details of the organic channel deposition process will be discussed in the following section.

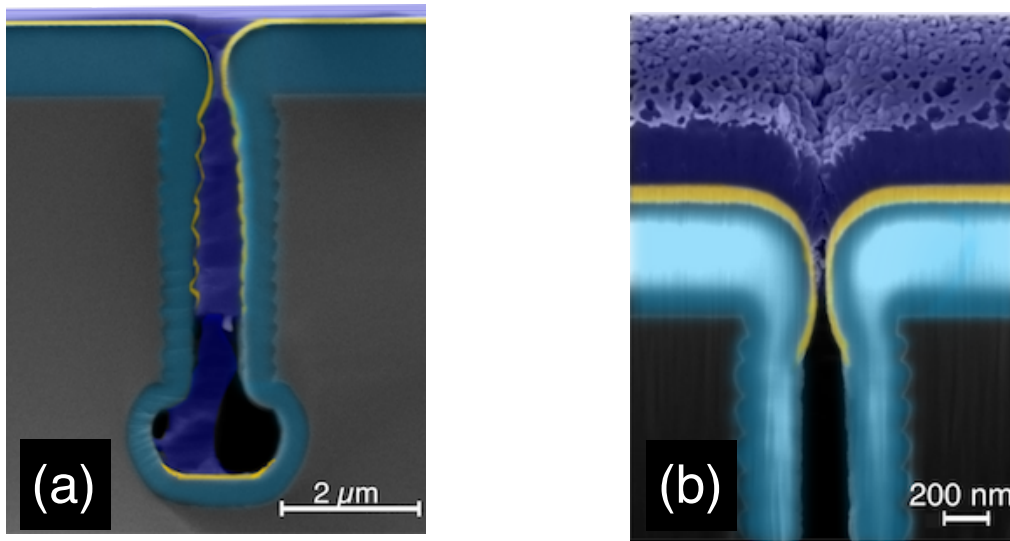


Figure 2.5 XSEM image of fabricated HED-TIEs with (a) solution processed TIPS-pentacene channel and (b) thermally evaporated H_2Pc channel. Figures taken from ref.⁴⁰.

2.2.1.1 Deposition of the trench refill layer

During the optimization process of the developed technology for HED-TIEs, both thermally grown oxide and LPCVD oxides were tried out for the deposition of the trench refill layer. Figure 2.6 shows the XSEM images of the fabricated structures with both types of trench refill layers. During the LPCVD oxide deposition, the thickness of the deposited layer on the electrode area is much more compared to the deposited thickness at the trench opening. It can clearly be seen from the XSEM image. The deposition rate declines due to shrinking gap. It also depends on the aspect ratio of the structure at the beginning of the deposition step. The larger the aspect ratio, the higher would be the deposition rate. On the other hand, once the trench opening becomes narrower, the deposition rate declines. This creates a “cone” shaped opening at the top part of the trenches. Judging from the initial trench dimension and the final trench dimension, it can be concluded that narrowing effect is more significant for the larger trenches. With this kind of ‘cone’ shaped trench openings, it is necessary to decide the layer thicknesses in such a way that the smaller trenches do not get closed during the LPCVD process or during the metal deposition, *i.e.* before the deposition of the organic material. Thermally grown SiO_2 layer is able to solve the problem of poor step coverage of oxide layer but it produced rounded corners which was again not beneficial for the device geometry. Metal deposition was not carried out in the case of

structures with the thermally grown oxide layer as the narrowed region in the trenches would have produced shorted electrodes. Finally, LPCVD oxide was chosen as the suitable trench refill layer over the thermally grown oxide layer for further processing of device fabrication.

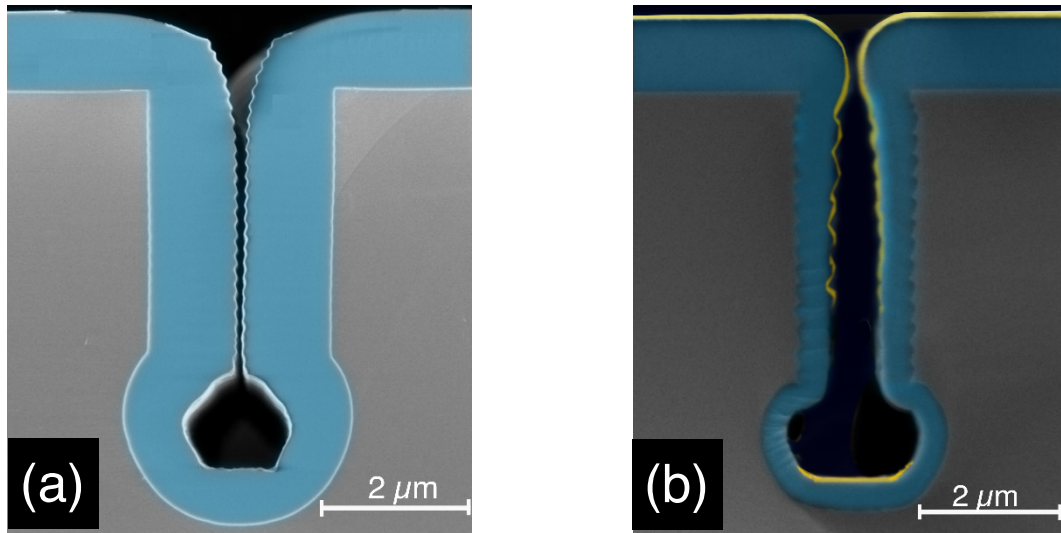


Figure 2.6 XSEM image of fabricated structures with two types of trench refill oxide layer: (a) thermally grown SiO₂ layer and (b) LPCVD SiO_x layer.

The deposition of such a thick oxide layer on various structures with different aspect ratios can lead to process parameter variations. This step can be subject of further optimization in the fabrication process in order to reduce the sensitivity of the electrode gaps to process variations. A further development of the fabrication technology using the “spacer approach” in the frames of this work yielded in better defined device geometry as described in the section 2.2.2.

2.2.1.2 Deposition of the organic channel material

(a) HED-TIE with thermally evaporated organic channel

In the initial phase of the work, different thermally evaporated channel materials were used to form the organic channels and their electrical characterizations were carried out⁴⁸. Exemplary, here we will focus on only thermally evaporated metal free phthalocyanine or H₂Pc based HED-TIEs. Phthalocyanines are a class of organic semiconductors, which have been a significant part of the research studies on molecular semiconductors due to their high chemical and thermal stability⁵⁰. Phthalocyanines are macrocyclic planar aromatic compounds, exhibiting semiconducting properties. Figure 2.7 shows the molecular structure of H₂Pc

molecules. The bandgap of H₂Pc is ~2.4 eV as reported in literature⁵¹.

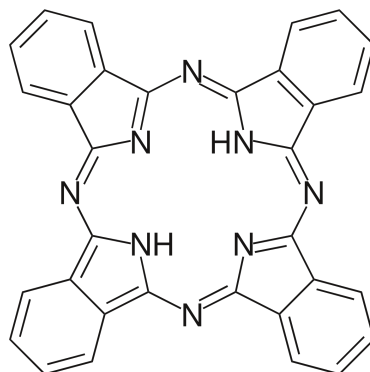


Figure 2.7 Molecular structure of metal free phthalocyanine molecule. Figure taken from ref.⁵².

In figure 2.8, the photograph of an array of TIE structures metallized with gold can be seen.

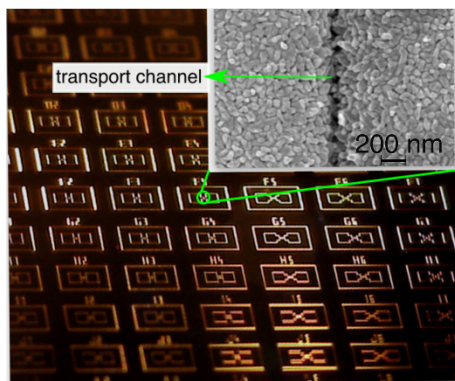


Figure 2.8 Photograph of an array of HED-TIE structures with gold electrodes. The inset shows scanning electron microscopic top-view of a HED-TIE with $W = 30 \mu\text{m}$ and channel length $L = 210 \text{ nm}$, after the evaporation of a nominal 300 nm phthalocyanine film thickness. Figure taken from ref.⁴⁰.

In case of the thermally evaporated channel devices, after the metallization step, a UV-curable adhesive polymer mask was aligned and positioned on top of the TIE gold structures. The shadow mask protects the electrode area from getting covered with the organic layer during thermal evaporation. The thermal evaporation of the molecules was performed in a vacuum chamber with a base pressure of $\sim 5 \cdot 10^{-8}$ mbar. The phthalocyanine powder was purchased from Sigma Aldrich and had a purity of 98%. The evaporation temperature was approximately 380 °C and the deposition rate was $\sim 1 \text{ nm/min}$. During the organic film deposition, the substrate was kept at room temperature. The typical nominal film thickness required to form all the channels was $\sim 300 \text{ nm}$. The inset of Figure 2.8 shows the SEM top view of the HED-TIEs with H₂Pc channels. The XSEM image of a similarly fabricated structure is shown in figure 2.5

(b), where it can be seen that the evaporated organic material forms a “free-standing” membrane between the electrodes. It is this membrane which forms the current conduction channel. The electrical properties of these devices will be discussed in chapter 3. The formation of such a “free-standing membrane” was observed in all devices fabricated by thermal evaporation of organic materials.

(b) HED-TIE with solution processed organic channel

To demonstrate the compatibility of the developed HED-TIE technology with standard solution processing techniques of the organic semiconductors, we fabricated 6,13-bis (triisopropylsilylethynyl)-pentacene or TIPS-pentacene solution-processed devices with trench isolated gold electrodes. TIPS-pentacene was chosen because it is a solution processable molecule and also is known to exhibit high carrier mobility values. TIPS-pentacene is a soluble derivative of pentacene and is frequently used in various organic devices such as OFETs or other electronic devices^{5,53,23}. As reported in previous studies, the highest unoccupied molecular orbital (HUMO) of TIPS-pentacene lies at ~5.20 eV while the lowest unoccupied molecular orbital lies at ~3.55 eV^{54, 55}. The bandgap of the material is ~1.65 eV^{54,55}. Figure 2.9 shows the molecular structure of TIPS-pentacene molecule.

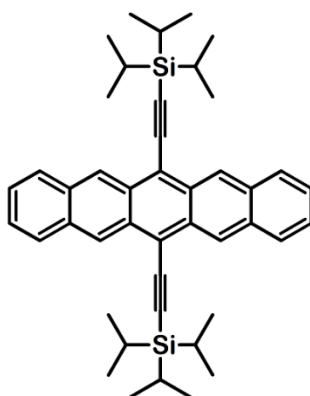


Figure 2.9 Molecular structure of TIPS-pentacene.

In the following chapters (chapter 4 & chapter 5), we will explore the possible applications of the TIPS-pentacene based HED-TIEs. To underline one key feature of the planar HED-TIEs, namely, the full accessibility of the active transport channel to external stimuli such as light, the devices were successfully tested for possible application as hybrid photodetectors. The devices were also found to exhibit light induced magnetoresistive properties.

TIPS-pentacene powder with a purity of 99.9 % was purchased from Ossila. The

solution was prepared in a mixture of toluene:tetralin (2:1) with a concentration of 8 mg/ml. Prior to drop-coating, the fabricated structures with gold electrodes were cleaned using acetone, ethanol and deionized water respectively. 3 μl solution was used to drop-coat the HED-TIE devices for a chip of 1 cm x 1 cm area. The drop-coating of the substrates was performed at 65 °C on a hot plate and the samples were kept at 65 °C for 30 min after drop-coating. This was to initiate crystallization of the TIPS-pentacene film and to ensure evaporation of the solvents from the film. The thickness of the drop-coated film was measured by atomic force microscopy (AFM). The largest thickness of the drop-coated TIPS-pentacene layer on the gold electrode area was found to be ~300 nm. The Raman spectrum of the drop-coated thin film compared with that of the as purchased TIPS-pentacene powder (both recorded at 514.7 nm excitation wavelength) and the spectra are shown in the figure 2.10.

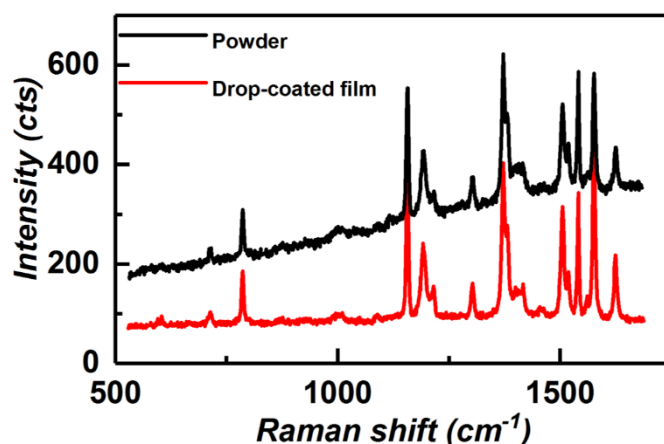


Figure 2.10 Comparison of the Raman spectra of the TIPS-pentacene powder and the drop-coated film (excitation wavelength used: 514.7 nm). Figure taken from ref.⁴⁰.

The typical features of TIPS-pentacene can be seen in both Raman spectra, indicating that the molecular structure is preserved upon drop-coating from solution. Figure 2.11 shows a photograph of a 1 cm x 1 cm chip with an array of gold TIE structures. The inset of figure 2.11 shows the optical microscopic image of an exemplary device with TIPS-pentacene channel. While the crystallized film of TIPS-pentacene does not cover the TIE structure homogeneously, the channel trench is covered almost homogeneously. The isolation trenches are, nevertheless, not completely filled and hence isolating. For the TIPS-pentacene devices, the adhesive shadow mask (as described for devices with evaporated channel materials) was not used, since UV-curing of the mask is needed to remove the mask from the devices, and TIPS-pentacene is a photosensitive material which can be photo-oxidized under UV

exposure in air⁴⁰. The contact pads were, therefore, covered with TIPS-pentacene films; however, it was still possible to contact the electrodes through the thin organic layer.

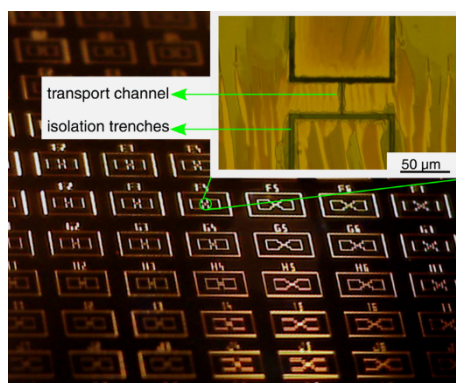


Figure 2.11 Photograph of a silicon chip with an array of gold TIE structures prior to deposition of the organic film. The inset shows an optical microscopic image of a fabricated device with channel width $W = 40 \mu\text{m}$ and channel length $L = 210 \text{ nm}$ after drop-coating with TIPS-pentacene solution. Figure taken from ref.⁴⁰.

XSEM image of a representative TIPS-pentacene based HED-TIE is shown in figure 2.5 (a). Unlike the devices with thermally evaporated channels, where the organic channel was found to form a “free-standing” membrane, the TIPS-pentacene was found to go inside the trench and partially fill it to form the transport channels. It should be noted that the non-polar solvent in the TIPS-pentacene solution exhibits a very good wetting of the gold electrodes which allows the solution to wet with the inner part of the trench and thus ensures the transport channel formation. The post-deposition thermal treatment leads to the growth of elongated, presumably crystalline, grains (darker areas in the inset of Figure 2.11).

The thermally evaporated phthalocyanines formed smaller crystals (grain size $< 100 \text{ nm}$) as shown in the inset of figure 2.8. When the electrical measurements were carried out for longer duration or repetitively, the phthalocyanine channel was found to get damaged, perhaps due to very high current density at the points where two or more grains touch each other. This issue was not present in the case of TIPS-pentacene based devices presumably due to the larger size of the crystalline domains ($> 50 \mu\text{m}$, as shown in inset of figure 2.11) which was found to cover the device channel area uniformly and thus avoiding the issue created by localized high current densities.

2.2.2 Spacer approach for fabricating HED-TIEs

The motivation behind modification of the process flow for fabricating HED-TIEs was to achieve a better control and reproducibility over the trench geometry. In trench refill approach, since the initial trench dimensions are 850 nm to 1050 nm, most of the channel opening reduction occurred during the LPCVD oxide deposition. Deposition of ~800 nm thick layer (or thicker depending on requirements) on various structures with different aspect ratio can lead to process parameter variations. Moreover, as discussed earlier, this LPCVD oxide layer was found to produce a “cone” shaped trench opening. Hence it was desirable to introduce some other step in the fabrication technology which can reduce the thickness of the deposited oxide layer. One possible option was to introduce an atmospheric pressure CVD (APCVD) deposited SiO_x layer, to tune the hard mask geometry in such a way that the gap is further reduced even before the deep etching of silicon is carried out. Figure 2.12 illustrates the difference in the fabrication approach using both the techniques.

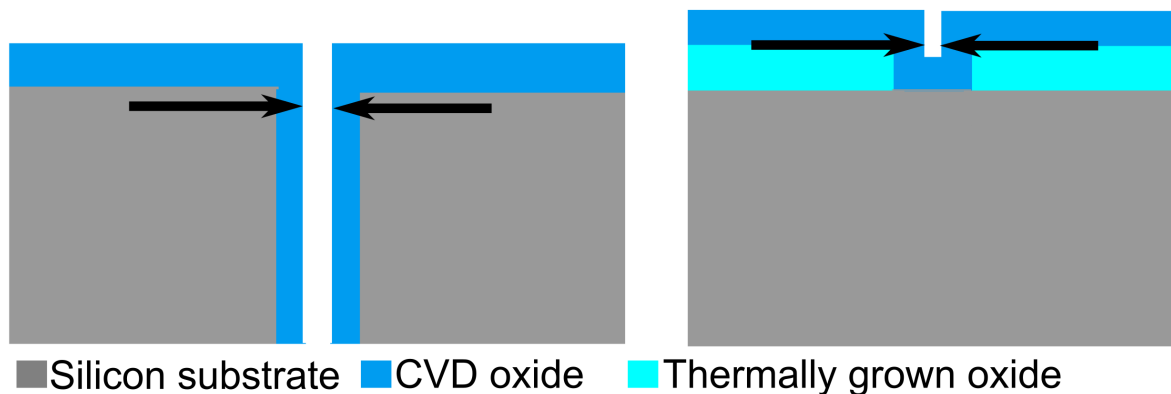


Figure 2.12 Schematic illustration of “trench-refill approach” (left) and “spacer approach” (right) for fabricating HED-TIEs. In “trench refill approach”, the electrode gap is determined by the thickness of the trench refill layer. In “spacer approach”, an APCVD oxide layer is used to alter the hard mask geometry for reducing the electrode gaps even before the trenches are etched.

Figure 2.13 shows the fabrication process flow of the hybrid devices with trench isolated electrodes using the “spacer approach”. (a) The process starts with cleaning the 100 mm n-type (100) silicon wafer with a specific resistance of 6–7 Ω cm. (b) Thermal oxidation of the wafer is performed to form a 1000 nm SiO_2 layer which acts as the hard mask layer. (c–d) Sub-micron trenches with dimensions ranging from 850 nm to 1050 nm are patterned on the hard mask layer using standard photolithography, and the SiO_2 layer is etched away using reactive ion etching. Following this, a 450 nm APCVD SiO_x layer is deposited as the spacer layer to alter the hard mask geometry.

APCVD oxide was found to have very good step coverage over the trenches, as desired. The thickness of this APCVD oxide depends on the thickness of the hard mask silicon dioxide layer. (e) Anisotropic etching of SiO_x is carried out to remove the APCVD oxide layer from the floor of the trench and only the vertical part of this layer is left near the trench opening. This remaining APCVD oxide forms the spacer, thus reducing the trench dimension by adjusting the hard mask geometry. (f) Deep reactive ion etching of silicon with an etch depth of $\sim 2 \mu\text{m}$ is carried out in a Surface Technology Systems (STS) multiplex inductively coupled plasma system to create the trenches. For this step, silicon etching was carried out first by using SF_6 and then the sidewalls were protected by polymers by using CF_4 . This polymer is then removed from the bottom of the trench to open the bottom of the trench for the isotropic etching step. (g) Isotropic etching of Si is carried out using a SF_6/O_2 plasma for 45 s. This forms a cavity at the bottom of the trench, which is needed for electrical isolation of the electrodes.

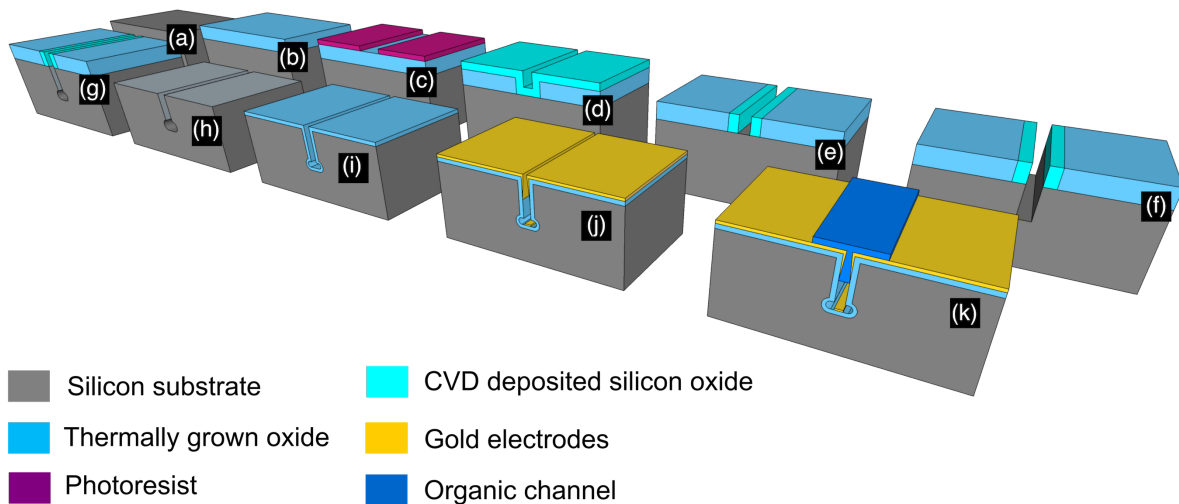


Figure 2.13 Schematic representation of the fabrication process flow of the HED-TIEs using “spacer approach”.

(h) The SiO_x layer which was used to protect the sidewalls of the trench is then completely removed by hydrofluoric acid (HF). (i) Thermally grown SiO_2 with a thickness of 130 nm is grown to form the isolation layer for isolating the electrodes. This also reduces the trench dimensions further. It should be noted; the thickness of the isolation layer could be brought down to 130 nm from the 800 nm LPCVD SiO_x layer which was used in trench refill approach. (j) Sputtering of a 30 nm thick gold layer is then carried out to form the device electrodes along with a 10 nm thick Cr adhesion layer. (k) Finally, the wafer is diced into $1 \text{ cm} \times 1 \text{ cm}$ chips followed by the organic

channel formation. The organic channel formation was carried out in the same way as described for “trench-refill approach”. For the chips fabricated using “spacer approach”, only solution processed TIPS-pentacene based HED-TIEs were fabricated and characterized.

Figure 2.14 shows the XSEM image of a fabricated structure using spacer approach. The minimum achieved electrode gap dimension was ~ 100 nm using an isolation layer of ~ 130 nm thermally grown oxide and a 30 nm gold, with 10 nm Cr adhesion layer as electrodes. Unlike the trench refill approach, where scallops were observed on the sidewalls, smooth vertical sidewalls were obtained using the above mentioned etching process.



Figure 2.14 XSEM image of fabricated HED-TIE structure using spacer approach, prior to deposition of the organic channel.

2.2.2.1 Deposition of the isolation layer

For deposition of the isolating SiO_2 layer between two electrodes, it was necessary to find an oxide deposition process which would provide good step coverage, uniform layer thickness and sharp cornered, non-rounded trench openings. Along with thermally grown oxide and LPCVD oxide (similarly to the tests performed in the trench refill approach), APCVD oxide was also tested in the spacer approach.

Figure 2.15 shows the XSEM of HED-TIE structures with thermally grown oxide as the isolation layer. Unlike the trench refill technology, where the thermally grown oxide was found to produce rounded corners (shown in figure 2.6), in spacer approach, the thermally grown oxide produced perfectly suitable and sharp trench geometry.

It should be noted that the fabricated structures shown in figure 2.15 were fabricated for test purpose to optimize the profile of the thermally grown oxide layer. The thickness of the used APCVD spacer layer was different in this case as compared to the structure

shown in figure 2.14, which produced wider trenches (shown in figure 2.15). Similar fabricated structures were also used to test the profile of the SiO_x layer deposited by LPCVD and APCVD and are shown in figure 2.17 and figure 2.18.

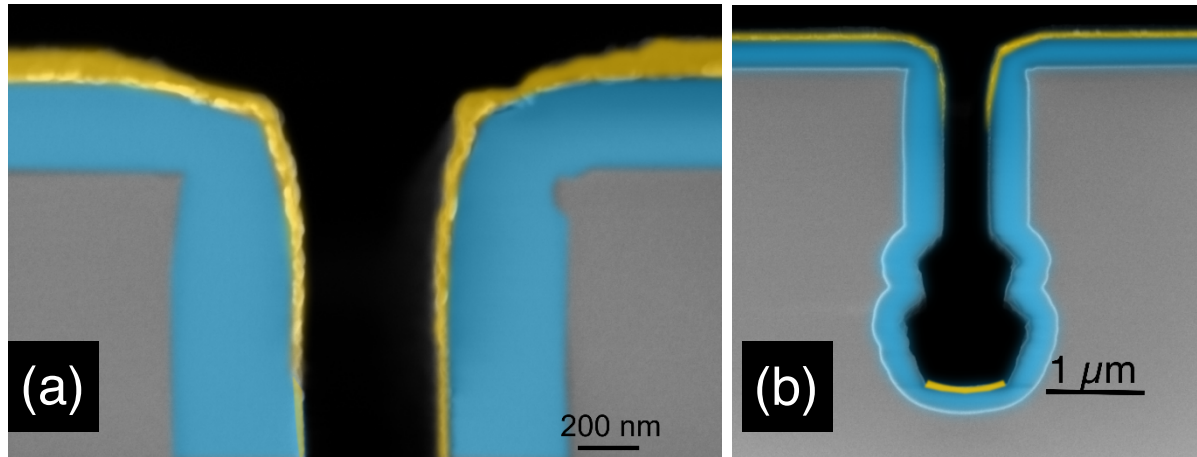


Figure 2.15 XSEM image of HED-TIE structure with thermally grown SiO_2 isolation layer: (a) zoomed in view of the trench opening and (b) complete view of fabricated HED-TIE structure.

After the deep reactive etching of Si, the fabricated structures were found to produce “notches” at the trench opening as shown in the figure 2.16.

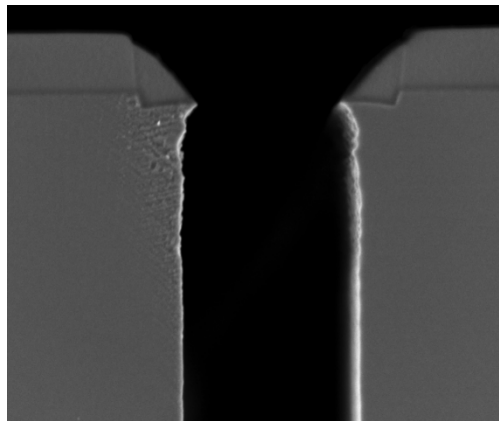


Figure 2.16 XSEM image of the trench opening after deep etching of silicon is carried out, showing the notches at the trench opening.

When SiO_2 is grown thermally, the silicon substrate is partially consumed. The growth rate is different where there is a corner. As these areas with notches have different growth rate, compared to the surroundings, the notches were consumed and thus trenches with non-rounded corners were obtained. Though the trench geometry was found to be suitable using thermally grown oxide as isolation layer, techniques like APCVD and LPCVD were also tested as these techniques are low-cost techniques

compared to thermal growth of SiO_2 .

Figure 2.17 shows the XSEM of HED-TIE structures with SiO_x isolation layer deposited by LPCVD. As previously observed for trench refill approach (shown in figure 2.6), the LPCVD oxide showed non-uniform thickness and poor step-coverage. For lower dimension trenches, it would again produce cone shaped trench openings leading to almost closure of the trench openings. This method was not chosen for further processing of HED-TIE structures.

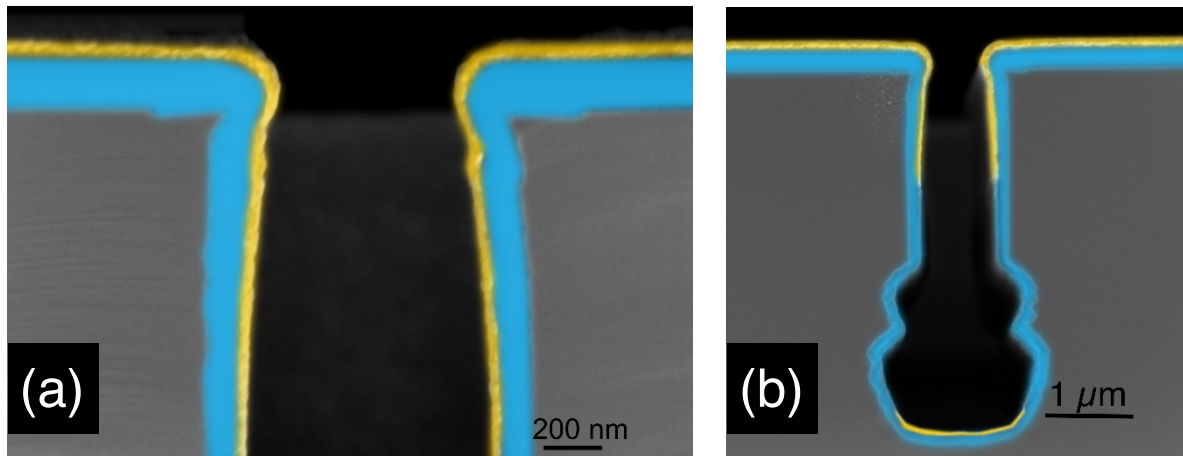


Figure 2.17 XSEM image of HED-TIE structure with LPCVD SiO_x isolation layer: (a) zoomed in view of the trench opening and (b) complete view of fabricated HED-TIE structure.

Figure 2.18 shows the XSEM images of the fabricated structures with APCVD SiO_x as isolation layer. APCVD SiO_x has a very good step-coverage and produces layers with uniform thickness.

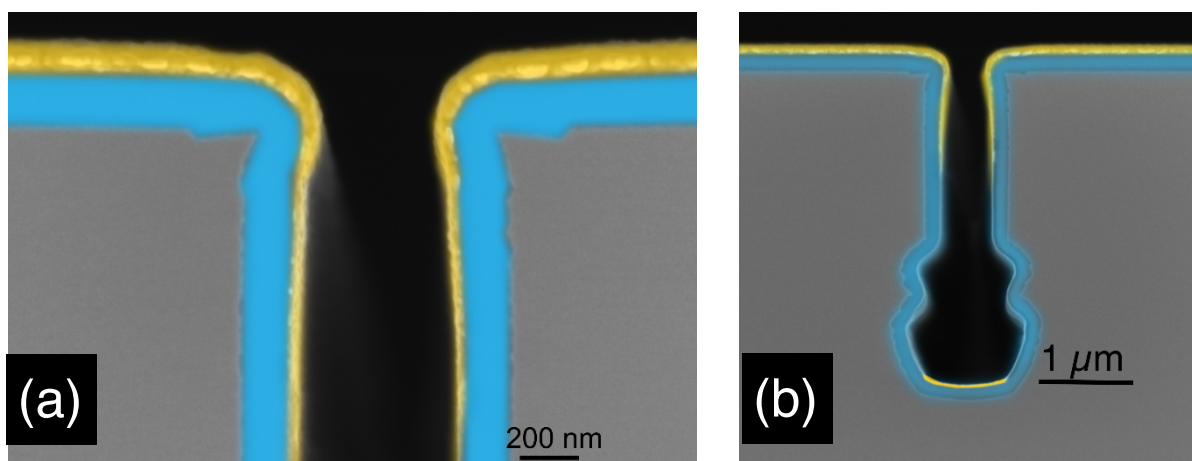


Figure 2.18 XSEM image of HED-TIE structure with APCVD SiO_x isolation layer: (a) zoomed in view of the trench opening and (b) complete view of fabricated HED-TIE structure.

This technique was also used to produce the spacers for tuning hard mask geometry.

When this APCVD oxide was used as isolation layer, sharp trenches with well-defined geometry were obtained. Initially this APCVD oxide was chosen as the suitable isolation layer as it is a low-cost technique as compared to thermally grown oxide. When devices were fabricated with APCVD oxide as isolation layer, however, the device current was found to increase over time. The device current over time measurements showed an increase in device current even after 2 h and the current was not found to stabilize. It was suspected that the APCVD oxide leads to leakage current which causes the increase in current over time. To verify this, devices with thermally grown oxide layers were fabricated and electrically characterized. These devices did not show any increase in current over time and hence finally, thermally grown oxide layer was used for the samples discussed in this work, as suitable isolation layer between the electrodes. The electrical characterization of the fabricated devices will be discussed in the next chapter.

2.3 Characterization techniques

(a) Electrical characterization

All electrical measurements described in this dissertation were conducted using a Keithley 2636A SYSTEM source meter unit in the auto-range mode. For the measurements carried out to investigate the electrical transport properties of the devices, measurements were conducted on a manual wafer-prober under a microscope for making electrical contacts precisely on all the devices in a chip.

For the optical sensing and magnetic sensing experiments, the measurements were carried out on wire-bonded devices to make it suitable for the experimental set up.

(b) Raman spectroscopy

Raman spectroscopy is a vibrational spectroscopic technique that can be used for studying the chemical structure of a material⁵⁶. The Raman effect was discovered by Sir C.V. Raman, who received the Nobel prize in Physics for this in 1930. The technique is very widely used as it is non-destructive, non-invasive method and can be performed in ambient conditions and even at room temperature. The Raman effect relies on how a light (typically laser beam) interacts with the matter. Upon irradiating the sample, two types of light scatterings occur. The Rayleigh scattering or the elastic scattering is the most intense one, which has the same energy as the excitation source. The weaker inelastic scattering is the Raman scattering. This scattering is a result of

the light interaction with the material in form of phonons or molecular vibrations. After a molecule or crystal is excited to a higher energy state, it relaxes either to a higher or lower vibrational state compared to the initial state resulting in gain or loss of energy and thus creating or annihilating phonons. These phenomena are known as Stokes or anti-Stokes scattering respectively.

(c) Photoluminescence spectroscopy

Photoluminescence (PL) spectroscopy is a non-contact, non-destructive method for probing the electronic structure of a material ⁵⁶. In principle, light with higher energy than the bandgap of the material is directed onto a sample, to be absorbed by the material. As a result, photo-excitation of the carriers takes place. This causes the carriers to jump to a higher electronic state, and once it relaxes and returns back to a lower energy level, the energy is released by emitting photons. The emission of light, or luminescence through this process is known as photoluminescence. Typical applications of PL spectroscopy include determination of bandgap, investigation of material quality and understanding the carrier recombination mechanism.

2.4 Summary and outlook

Summarizing, HED-TIE technology was introduced as a wafer-level approach for the fabrication of planar organic–inorganic hybrid devices with trench isolated electrodes. Electrode gap dimensions were fabricated with dimensions in the range of ~100 nm, using conventional photolithography. Two different types of fabrication approaches were discussed: (a) trench-refill approach and (b) spacer approach. In trench refill approach, sub-micron trenches are patterned first and then partially refilled with a thick layer of LPCVD SiO_x layer, to achieve the desired electrode gap dimension. In case of the spacer approach, an additional APCVD grown oxide layer was introduced to tune the hard-mask geometry and thus reducing the electrode gap dimension even before the deep etching of silicon is carried out. The spacer approach was found to produce HED-TIE structures with more controlled and reproducible geometry. Both APCVD oxide and thermally grown oxide isolation layers were found to produce HED-TIE structures with the desired device geometry but APCVD oxide was found to be unsuitable as electrical isolation layer. Thermally grown oxide was finally chosen as the desired isolation layer.

To demonstrate the compatibility of the fabrication technology, HED-TIEs with both solution processing of organic molecules as well as thermal evaporation of organic molecules in vacuum were fabricated. For this, thermally evaporated metal free phthalocyanine (H_2Pc) based HED-TIEs and solution processed 6,13-bis(triisopropylsilylethynyl)pentacene or commonly known as TIPS-pentacene based HED-TIEs were fabricated. The thermally evaporated channels were found to form a “free-standing” membrane between the electrodes whereas the TIPS-pentacene solution was found to penetrate deep inside the trench and form the electrical transport channel. It should be mentioned that it is important to use a suitable solvent which has good wetting properties with the metal electrodes to make the channel formation successful.

The key aspects of the proposed technology are as follows: (i) the TIE process flow is compatible with standard silicon technology and can be scaled up for high-volume manufacturing on 200 mm or 300 mm wafers for industrial applications; (ii) the device geometry is not limited to two-terminal architecture; gate electrode can easily be incorporated to form three-terminal transistor structures. The technology offers the flexibility of selecting various materials, including ferromagnetic metals or oxides can be used for the electrode layer; (iii) the HEDs fabrication is compatible with various deposition techniques of the active transport channel, such as solution processing techniques, stamping, or vacuum deposition by thermal evaporation; (iv) the HED-TIEs are not restricted to organic channels: other materials such as polymers oxides, or even 2D materials such as graphene, MoS_2 , WSe_2 etc. can be implemented in the highly flexible fabrication flow. The HED-TIE technology offers full accessibility of the active transport channel to external stimuli such as light or gases and thus making it suitable for various sensing applications. Few of the possible applications will be demonstrated in the following chapters. In future, one possibility would be depositing two different electrode materials on the two different electrodes using the shadowing technique as proposed in ref.⁴⁵, which would open up the possibility of fabricating devices where different electrode materials are needed.

Chapter 3

Electrical characterization of HED-TIEs

The basic electrical conduction mechanisms in organic-inorganic hybrid devices will be influenced by a multitude of parameters, including device geometry, intrinsic carrier mobility, crystalline structure of the channel material, coverage of the channel material, the deposition techniques used, metal-organic contact properties *etc.* Depending on whether the device is a two-terminal device or a three terminal device, different static electrical measurements such as output characteristics, transfer characteristics *etc.* with or without the gate voltage can be measured and analysed to understand the conduction properties. This chapter focuses on the current-voltage characteristics of HED-TIEs and in particular on the influence of the device geometry, on the electrical properties of the devices. To this purpose, two-terminal HED-TIEs with organic channel produced by either solution processing or thermal evaporation were used. Some of the results discussed here were published in ref.⁴⁰.

3.1 Theoretical background

3.1.1 Space charge limited current (SCLC) conduction mechanism

In low mobility materials such as organic materials or dielectrics, when electric field is applied, charges are likely to accumulate and the induced electric field due to the accumulated charges influences the current transport through the device. SCLC occurs when the injected carrier density is higher than the intrinsic free carrier density of the material. This creates a space charge limited region near the metal/organic contact where the charges are injected. The electrostatic potential of the space charges prevents injection of additional charges in the material and limits the device current^{57,58}. The current through the device is then only dependent on the charge carrier mobility and not on the charge carrier density. The carrier mobility can thus be determined from current-voltage measurements. Provided the commonly low carrier mobility in organic semiconductors, the metal/organic-semiconductor/metal heterostructures usually exhibit SCLC conduction mechanism^{59,60}.

For the hole-conducting molecules used in this chapter as solution-processed channel material (TIPS-pentacene⁶¹) and thermally evaporated channel material (H₂Pc^{50, 48}), the SCLC was previously reported to be the main conduction mechanism for holes.

The basic considerations of this mechanism for a unipolar device are, therefore, addressed in the following section.

In absence of any traps in the organic semiconductor, and assuming that the injecting contact is ohmic (the current through the device is not limited by the injection), the space charge limited current density in a unipolar material (only one type of carriers contribute to the current) can be described by the Mott-Gurney law⁶²:

$$J = \frac{9}{8} \mu \epsilon_0 \epsilon_r \frac{V^2}{L^3} \quad (3.1)$$

where J is the current density, μ is the free carrier mobility, ϵ_0 and ϵ_r are electric permittivity of vacuum and the dielectric constant of the material respectively, V is the applied voltage and L is the distance between the two electrodes or the device channel length. Here, the current is assumed to be caused by only one type of carriers (either electrons or holes), the mobility is assumed to be independent of the electric field and, the effect of charge carrier diffusion is neglected.

Considering the presence of traps in the material, which is a more realistic situation, the SCLC equation will have to be modified by taking into account the energetic distribution of traps. Very often in literature, the energetic trap distribution in organic semiconductors is assumed to have an exponential shape (and are termed, therefore, also tail states):

$$\rho_{traps}(E) = \frac{N_t}{E_B} \exp\left(\frac{-E}{E_B}\right) \quad (3.2)$$

where E_B and N_t are the characteristic energy and total trap density, respectively.

In such systems the SCLC can be expressed as⁶²:

$$J = q \mu N_v \left(\frac{\epsilon_0 \epsilon_r}{q N_t} \frac{m}{m+1} \right) \left(\frac{2m+1}{m+1} \right)^{m+1} \frac{V^{m+1}}{L^{2m+1}} \quad (3.3)$$

where J is the current density at an applied voltage V , μ denotes the free carrier mobility, N_v is the effective density of states, q is the electronic charge, L denotes the channel length of the device and m is a constant which has a value > 1 . In absence of traps or at higher voltages, when the traps are completely filled, *i.e.* for $m = 1$ and $N_v/N_t = 1$, the equation (3.3) will reduce to the Mott-Gurney law expressed in the equation (3.1).

Figure 3.1 shows the trap-free space-charge-limited electron transport in amorphous tin(IV) phthalocyanine dichloride thin film for various film thicknesses as reported by Qiao *et al.* in ref.⁶³. It can be observed that the J - V characteristics exhibit two regions for all thicknesses. In the lower voltage region, the current is linearly dependent on voltage, indicating an ohmic conduction. In the higher voltage region, the behaviour changes from linear to a curve with a slope of ~ 2 , indicating a SCLC conduction.

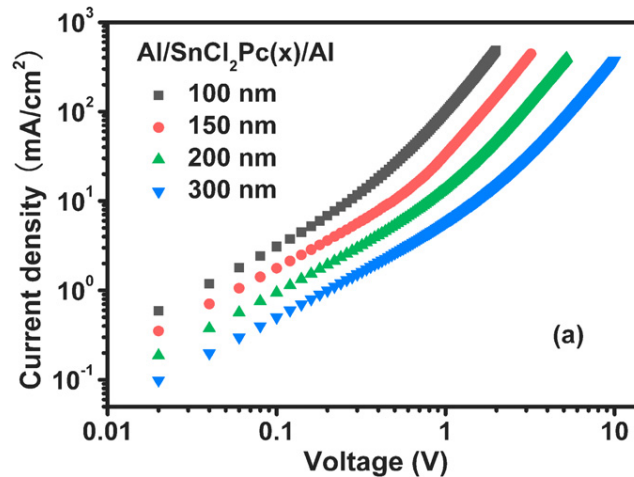


Figure 3.1 Dependence of the current density (J), on the applied voltage (V), for Al/SnCl₂Pc/Al devices at various thicknesses of SnCl₂Pc. Figure taken from ref.⁶³.

Figure 3.2 illustrates the SCLC behaviour observed by El-Nahass *et al.*⁵⁰ for thermally evaporated phthalocyanine films. Similar to what was observed for SnCl₂Pc, as shown in figure 3.1, H₂Pc was also found to exhibit two distinct regimes of current conduction.

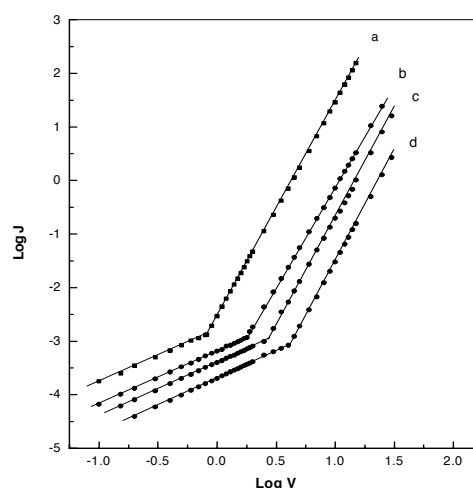


Figure 3.2 Dependence of the current density (J), on the applied voltage (V), for H₂Pc samples of different thickness (a) 138, (b) 201, (c) 253 and (d) 312 nm. Figure taken from ref.⁵⁰.

The lower voltage region exhibits an ohmic conduction whereas at higher voltages the SCLC is observed, with an approximate slope of 3.9 (slope > 2), indicating an

exponential trap distribution in the films. The critical voltage at which the transition from ohmic conduction to SCLC occurs, is expected to depend on the volume generated conductivity of the film and hence is directly proportional to the film thickness⁵⁷. This can clearly be observed in both figure 3.1 and figure 3.2. In SCLC, the carriers get accumulated at the metal/organic interface from where the charges are injected and the carrier density decreases as the distance from the interface increases, due to the space charge formation. At a distance away from the interface, less number of charge carriers is available for conduction, leading to a decrease in current with increasing thicknesses of the films. At lower applied voltages, the injected charge density is lower than the intrinsic free carrier density of the material and hence at lower voltages, in absence of the space charges, the ohmic conduction dominates.

Figure 3.3 shows the typical characteristic shape of SCLC conduction behaviour as reported by Agarwal *et al.*⁶⁴ for ITO/CuPc/Al devices. The inset of the figure shows the variation of the current density for various channel lengths for a fixed bias of 0.2 V.

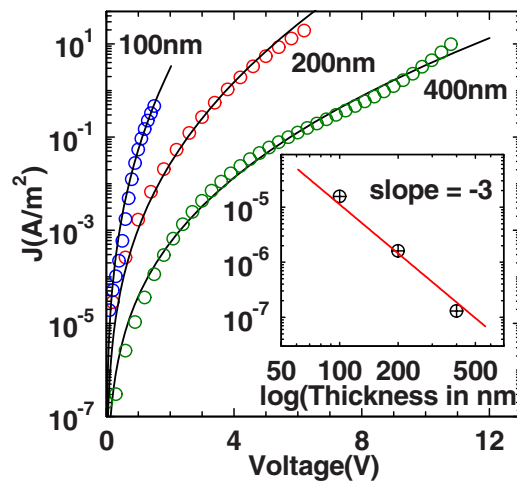


Figure 3.3 Characteristic shape of J - V plot of ITO/CuPc/Al devices exhibiting SCLC conduction. Figure taken from ref.⁶⁴.

3.2 Experimental details

Firstly, devices fabricated using “trench-refill” approach as described in chapter 2 were used with both evaporated and solution processed channel materials. In the later stage of the work, a new mask design was developed introducing interdigitated electrode structures to increase the effective volume of the channel material and thus increasing the overall device current. Only TIPS-pentacene based devices were fabricated for the structures with interdigitated electrodes and the dependence of the current amplitude on the device geometry were studied. As these devices were fabricated at a later

stage, the “spacer” approach for fabrication was used for producing devices with more controlled and reproducible geometry. The schematic of the device layout is shown in figure 3.4. The “L” denotes the transport channel length and “w” denotes the width of the transport channel. The width of the isolation trench was kept as 5 μm .

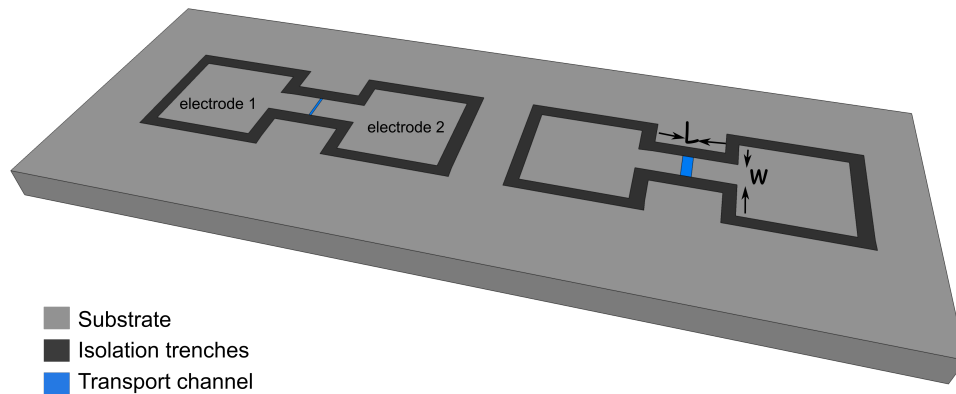


Figure 3.4 The schematic of the device layout of the HED-TIE devices.

In the devices without interdigitated electrodes, the channel widths were kept either to 30 μm or 40 μm . The channel lengths were varied as 120 nm, 170 nm, 210 nm, 250 nm and 300 nm after the deposition of the metal layer as discussed in chapter 2. The electrode dimension was 200 μm x 200 μm . Figure 3.5 shows the schematic of the device layout with interdigitated electrodes. In the devices with interdigitated electrodes, the channel widths were varied by using structures from 1 finger to 100 fingers of 50 μm each, resulting in channel widths of 50 μm (1 finger), 100 μm (2 fingers), 500 μm (10 fingers), 1000 μm (20 fingers) and 5000 μm (100 fingers).

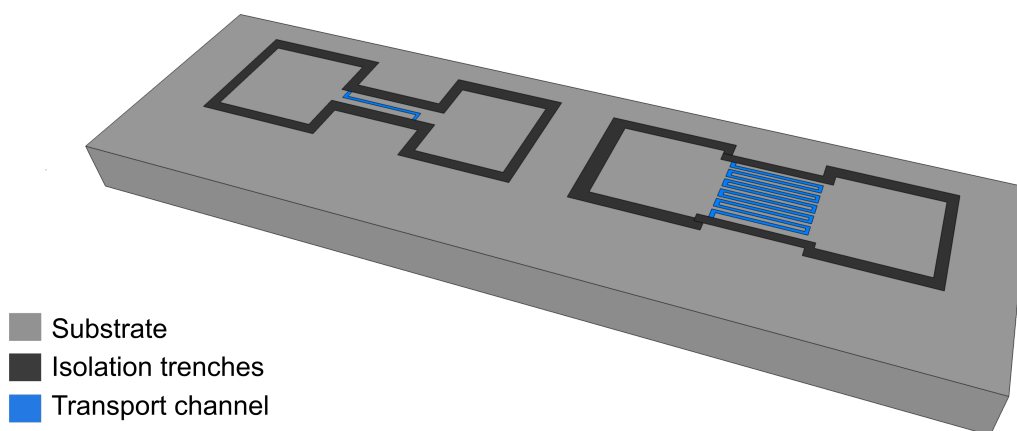


Figure 3.5 The schematic of transport channels of the HED-TIE devices with interdigitated electrodes showing a device with single finger (left) and a device with multiple fingers (right).

The channel lengths achieved after the deposition of the metal layer were 100 nm, 150 nm and 200 nm. The electrode dimensions were of 800 μm x 800 μm size. The sample preparations were done in the same way as described in chapter 2, section 2.2.1.2. The electrical measurements were conducted as described in chapter 2, section 2.3 (a).

3.3 Results and discussions

The current-voltage (I - V) characteristics of the TIPS-pentacene based HED-TIEs are shown in figure 3.6 for the shortest (120 nm) and the longest channel (300 nm) devices. The I - V characteristics are symmetric around 0 V. In agreement to the equation 3.1 and equation 3.3, the shorter channel HED-TIE indeed shows higher current compared to the longer channel HED-TIE.

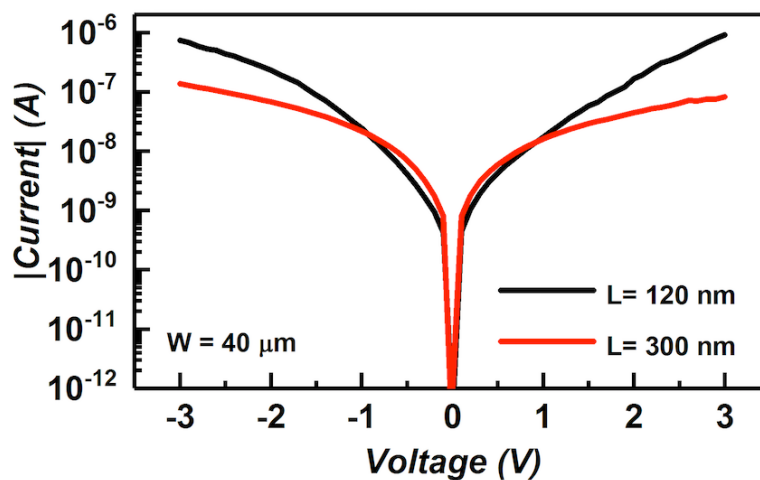


Figure 3.6 The current-voltage characteristics of solution processed TIPS-pentacene based HED-TIEs for devices with 120 nm and 300 nm transport channels. The channel width for both devices is kept at 40 μm .

In figure 3.6. it can also be observed that, at low voltages the current increases linearly with the voltage (*i.e.* ohmic behaviour) before it starts following the typical higher-power law of the SCLC mechanism. This becomes more evident in the $\log(J)$ vs. $\log(V)$ plot shown in figure 3.7. For any finite conductivity, there would be a range of voltages around zero for which the ohmic conduction would dominate. For voltages higher than a particular critical voltage, space-charge-limited current conduction would start to be dominant. For applied voltage higher than 0.5 V, the $\log(J)$ vs. $\log(V)$ plot for 120 nm channel device exhibits a slope of ~ 3.6 (slope > 2) (see figure 3.7), indicating a trap dominated SCLC conduction mechanism. For the 300 nm channel TIPS-pentacene

HED-TIE the $\log(J)$ vs. $\log(V)$ plot a clear transition voltage from ohmic to SCLC dominated transport is difficult to be identified in the measured voltage range, since also at higher voltages the slope is ~ 1.7 (slightly lower than 2). Perhaps the device is expected to reach a slope of ≥ 2 for an even higher measured voltage range.

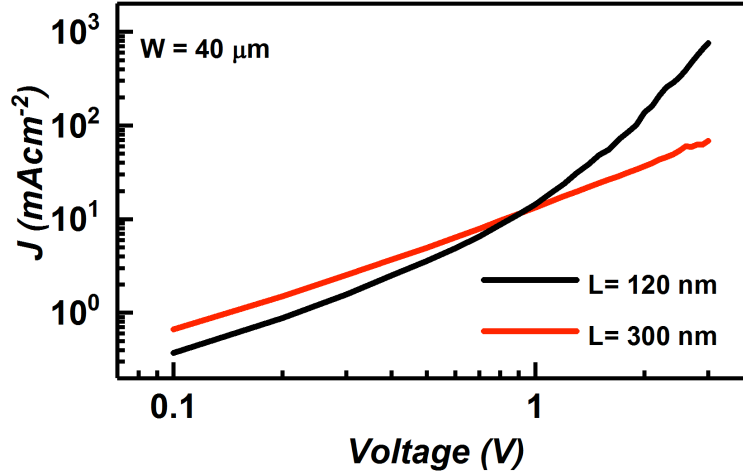


Figure 3.7 The $\log(J)$ vs $\log(V)$ plot of solution processed TIPS-pentacene based HED-TIEs indicating trap dominated SCLC conduction.

Figure 3.8 shows the J vs $1/L^3$ plot for devices with different channel lengths. The dotted line shows the expected linear behaviour according to equation (3.1) for devices with trap-free SCLC conduction.

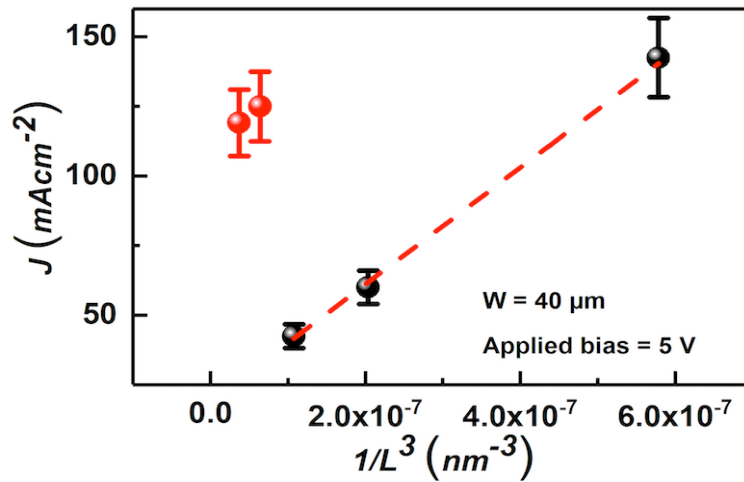


Figure 3.8 The current density (J) vs. $1/L^3$ (where L = device channel length) plot for TIPS-pentacene based devices with channel width of $40 \mu\text{m}$. The dotted line indicates the expected behaviour assuming space charge limited current conduction.

For smaller (120 nm – 210 nm) channel devices, the current density (black dots) follows the expected trend, while for the larger channel (250 nm and 300 nm) devices, the current density values (red dots) are much higher than that of expected from SCLC equation. The error bars in figure 3.8 indicate the deviation in measurement values

when the same device is measured repeatedly. It was found to be $\sim 10\%$ of the current amplitude. This apparent discrepancy between the shorter channel solution processed HED-TIEs and larger channel solution processed HED-TIEs can be explained by considering the degree of filling of the channels. When the trench opening is larger, more amount of channel material can go inside the trench. The higher volume of channel material yields in higher current values. The drift carrier mobility calculated for the HED-TIEs were in the range of $7 \cdot 10^{-4} - 2 \cdot 10^{-3} \text{ cm}^2 \text{ V}^{-1} \text{ s}^{-1}$. Similar drift carrier mobility values were reported for TIPS-pentacene devices by Ostroverkhova *et al.*⁶⁵ It should be noted that the mobility values determined for TIPS-pentacene in field effect transistors are higher (in the range of $\sim 10^{-2} - 1 \text{ cm}^2 \text{ V}^{-1} \text{ s}^{-1}$) due to filling of tail states at high carrier concentrations in the channel⁶⁵.

Figure 3.9 shows the I - V characteristics of the HED-TIEs with evaporated channel material (H_2Pc) for different channel lengths and the same channel width of $30 \mu\text{m}$. It can be seen that the current increases with decreasing the electrode gap dimensions.

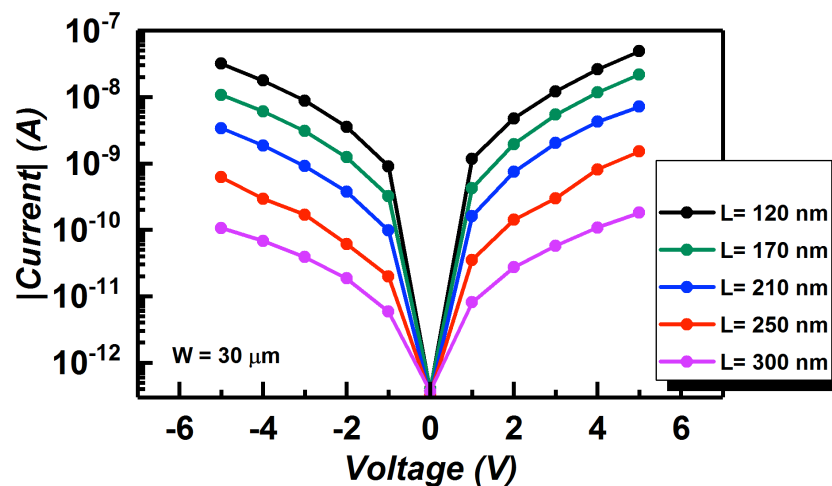


Figure 3.9 The current-voltage characteristics of HED-TIEs with thermally evaporated H_2Pc transport channels. The channel length is varied as 120 nm, 170 nm, 210 nm, 250 nm and 300 nm whereas the channel width for all devices is kept at $30 \mu\text{m}$.

The curves exhibit an ohmic behaviour for the lower voltage regime (applied voltage $< 0.5 \text{ V}$), as discussed earlier for TIPS-pentacene HED-TIEs, and have the characteristic shape⁶⁴ for the space charge limited current conduction mechanism in the higher voltage regime.

The devices with evaporated channel material exhibit slopes in the range of 2.7- 3 (slope > 2) for the $\log (J)$ vs. $\log (V)$ plot for different channel lengths (as shown in figure 3.10) indicating the same kind of trap dominated SCLC transport mechanism as the solution processed devices.

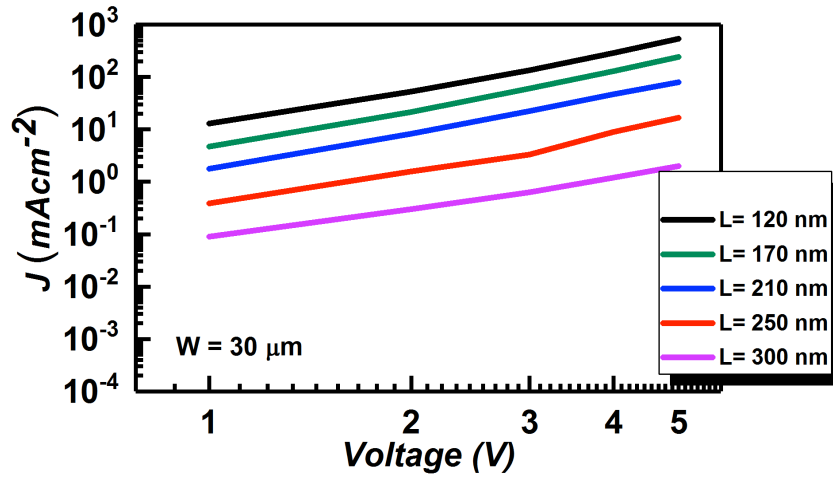


Figure 3.10 The $\log(J)$ vs $\log(V)$ plot of HED-TIEs with thermally evaporated H_2Pc as channel materials. The curves were found to exhibit a slope >2 , indicating trap dominated SCLC conduction.

As shown in figure 3.11, all devices with evaporated channel materials follow the predicted (according to eq. 3.1) linear behavior when the J vs $1/L^3$ plots is considered.

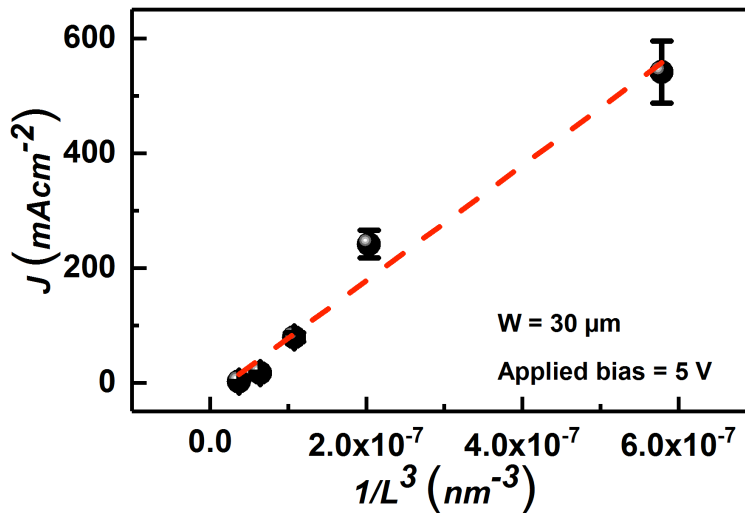


Figure 3.11 The current density (J) vs. $1/L^3$ (where L = device channel length) plot for H_2Pc based devices with channel width of $30 \mu\text{m}$. The dotted line indicates the expected behaviour assuming space charge limited current conduction.

In these devices, as discussed in chapter 2 and also in ref.⁴⁸, we observed that the channel forms as a “free standing” membrane on top of the electrodes and hence the influence of the degree of trench filling (with H_2Pc) on the current magnitude should be negligible. The carrier mobility for H_2Pc based HED-TIEs calculated using SCLC equation was found to be in the range of $\sim 10^{-4} \text{ cm}^2 \text{ V}^{-1} \text{ s}^{-1}$, which is higher than what is reported for H_2Pc two-terminal devices in ref.⁵⁰. The hole mobility for the reported films

was found to be in the range of $\sim 10^{-6} \text{ cm}^2 \text{ V}^{-1} \text{ s}^{-1}$. The results discussed till now were based on the layout without interdigitated electrodes.

In future, temperature dependent I - V measurements can be performed for both solution-processed and thermally evaporated channel HED-TIEs, to understand the SCLC conduction in sub-micrometer two-terminal planar devices in further detail and to investigate the transition of the trap dominated SCLC to the trap-free SCLC or SCLC with completely filled trap states for various device geometries.

In the next section, the improvements in device current which was obtained by using the devices with interdigitated electrodes, due to the increase in the channel volume of the fabricated devices, will be discussed. For this purpose, only devices with solution processed TIPS-pentacene channels were fabricated and characterized.

Figure 3.12 shows the I - V characteristics of the HED-TIEs with interdigitated electrodes with an effective channel width of $5000 \mu\text{m}$. The device channel length was varied as 100 nm , 150 nm , and 200 nm . As expected, similarly to the case of “simple” devices discussed before (see figure 3.6 and corresponding discussion), the current magnitude in the interdigitated devices decreases with increasing channel length indicating SCLC conduction.

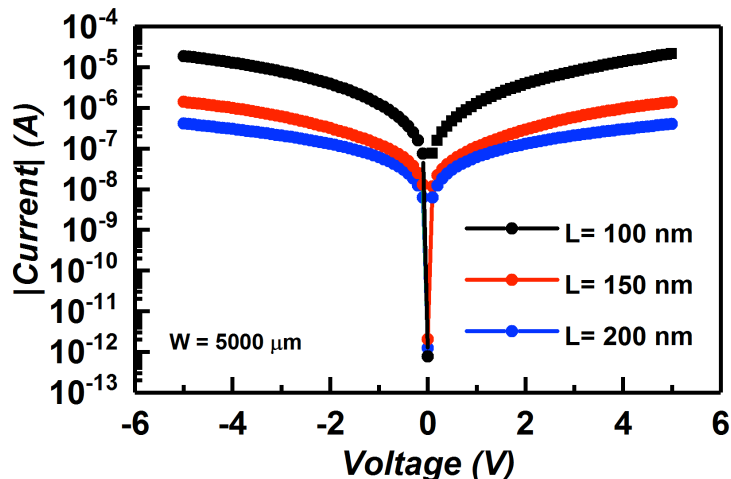


Figure 3.12 Current-voltage characteristics of solution processed TIPS-pentacene based interdigitated HED-TIEs for devices with 100 nm , 150 nm and 200 nm transport channels. The large channel width of all devices ($5000 \mu\text{m}$) was realised by using interdigitated electrodes with 100 finger structures of $50 \mu\text{m}$ each.

The influence of the device channel width, which was varied from $50 \mu\text{m}$ to $5000 \mu\text{m}$, on the current-voltage characteristics was investigated by keeping the channel length constant at 100 nm (see figure 3.13). Since the increase in channel width would lead to a linear increase of the channel volume without modifying the channel length and

thereby without yielding any change in the transport mechanism, it is expected that the current will scale linearly with the device channel width. At an applied voltage of 5 V, the device with 50 μm channel length gives a current of $\sim 0.1 \mu\text{A}$. When the channel width is increased to 500 μm and 5000 μm , the device currents are also increased to 1 μA and 10 μA respectively. The linear increase of device current with the increasing channel width is shown in the inset of figure 3.13. This remarkable improvement in the device current magnitude, achieved by introducing the interdigitated electrodes, can in later studies be exploited to increase the device sensitivity when used for sensing applications.

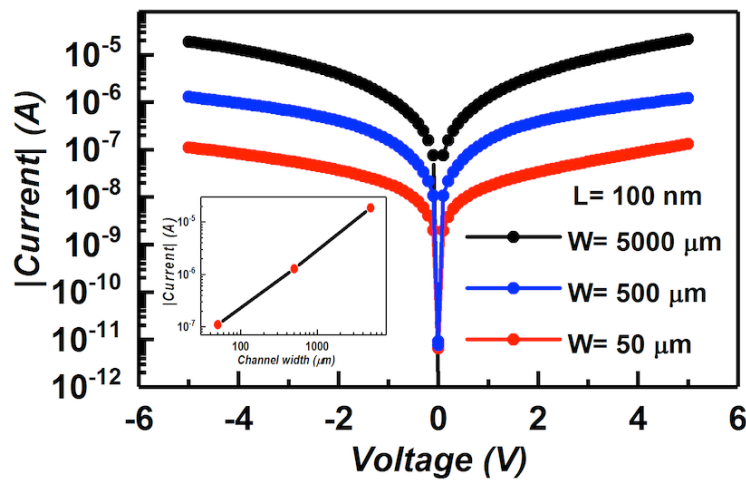


Figure 3.13 Current-voltage characteristics of solution processed TIPS-pentacene based HED-TIEs for devices with 50 μm , 500 μm and 5000 μm channel widths. The channel length for all the devices is 100 nm. The current is found to scale linearly with the device channel widths as shown in the inset.

It is worth mentioning here that the chips (1 cm x 1 cm) with “simple” two-terminal devices contained 88 devices per chip and the chips (1 cm x 1 cm) with interdigitated electrodes two-terminal devices contained 45 devices in each chips. The yield of working devices was found to be more than 97 % in both cases. 3 % or less of the devices in one chip were found to have shorted electrodes or isolation issues. This very good yield of working devices can open up the possibility for fabricating HED-TIEs at a wafer scale for industrial applications in future.

For demonstrating the possible applications of HED-TIEs, only the solution processed TIPS-pentacene based HED-TIEs will be considered and the results will be discussed in the following chapters.

3.4 Summary and outlook

To summarize, the current-voltage characteristics of two-terminal HED-TIEs were investigated for devices with both solution-processed and evaporated channel materials. The $\log(J)$ vs. $\log(V)$ plots exhibited slope >2 indicating trap dominated SCLC behaviour. The device currents were found to increase with decreasing the channel lengths of the devices. The J vs. $1/L^3$ plot followed the expected linear behaviour for the thermally evaporated channel devices, while a discrepancy was observed for the two largest channel length solution processed devices. This difference between the solution processed and thermally evaporated channels can be explained considering the filling of the trench channels with the organic material. In the case of solution processing, the amount of solution going inside the trench can vary with the channel length, thereby influencing the active channel (contact) area and hence the current density. In contrast, the thermally evaporated molecules form “free standing” channels and the active contact area is less affected by the channel length variation. It was also shown that the HED-TIE technology is flexible with respect to the device geometry and that by introducing interdigitated electrodes which allowed an increase of the channel width from 50 μm up to 5000 μm the device currents were found to increase proportionally with the effective channel width, *i.e.* in this case by 2 orders of magnitude. All chips had a yield of $> 97\%$ working devices. In future, further studies on the basic electrical properties of HED-TIEs can be performed by performing, *e.g.* temperature dependent I - V measurements, which were not possible in the frame of this work due to time limitations. This will help in understanding the SCLC conduction in sub-micrometre scale two-terminal lateral devices in further detail and clarify still open questions, *e.g.* related to the transition of the trap dominated SCLC to the trap-free SCLC or SCLC with completely filled trap states.

Chapter 4

Application of HED-TIEs as optical sensors

One key feature of the HED-TIEs developed in this work, is the full accessibility of the active transport channel from top to external stimuli such as light. This feature can be exploited for the fabrication of HED-TIEs as hybrid photodetectors by choosing a suitable channel material which is photosensitive. In the previous chapters, the successful transport channel formation in HED-TIEs using solution processed TIPS-pentacene as the channel material was demonstrated and the electrical transport properties of the TIPS-pentacene based HED-TIEs were discussed. In the first part of this chapter the photosensing properties of the fabricated HED-TIEs under different single wavelength illumination will be investigated for HED-TIEs with different channel lengths below 1 μm . The results based on the photosensing properties of TIPS-pentacene HED-TIEs were published in ref.⁴⁰ The photosensing properties of the TIPS-pentacene HED-TIEs were further tuned by incorporating gold nanoparticles of two different sizes in the TIPS-pentacene matrix, and will be discussed in the second part of this chapter.

4.1 Photosensing properties of TIPS-pentacene based HED-TIEs

4.1.1 Theoretical background

Over the recent years, significant progress has been made in the development of flexible electronic devices. This has mostly been driven by the demand for consumer electronic goods which are low-cost and flexible. To cater to this market, flexible optoelectronic devices are being extensively researched, covering a wide range of materials from 2D materials to organic semiconductors^{66,67,68}. Organic semiconductors have been studied for various applications like photovoltaics¹⁹, light-emitting diodes⁶⁹ and photodetectors⁷. Significant improvement has been achieved in terms of materials and the processing techniques for fabrication of high performance, low-cost organic optoelectronic devices.

TIPS-pentacene is known to be not only air stable⁶ as discussed before, but it is also a photosensitive^{7,70} material. In a previous report, TIPS-pentacene transistors with channel lengths in the range of 10 μm to 1000 μm were shown to have good

photosensing properties under ultraviolet (UV) and white light illuminations^{7,71}. The authors investigated the photosensing properties of the TIPS-pentacene thin film transistors under dark, UV (wavelength, 365 nm) and white light illuminations and compared. The output characteristics of the TIPS-pentacene-transistors under UV and 100 mW/cm² white light illuminations are shown in Figure 4.1 and 4.2 respectively. It was shown that the photoresponse of the TIPS-pentacene in the off state is higher than that of on state of the transistors. The obtained results suggested that UV and white light could optically control device operation as an additional terminal rather than the conventional source, drain and gate electrodes of a transistor.

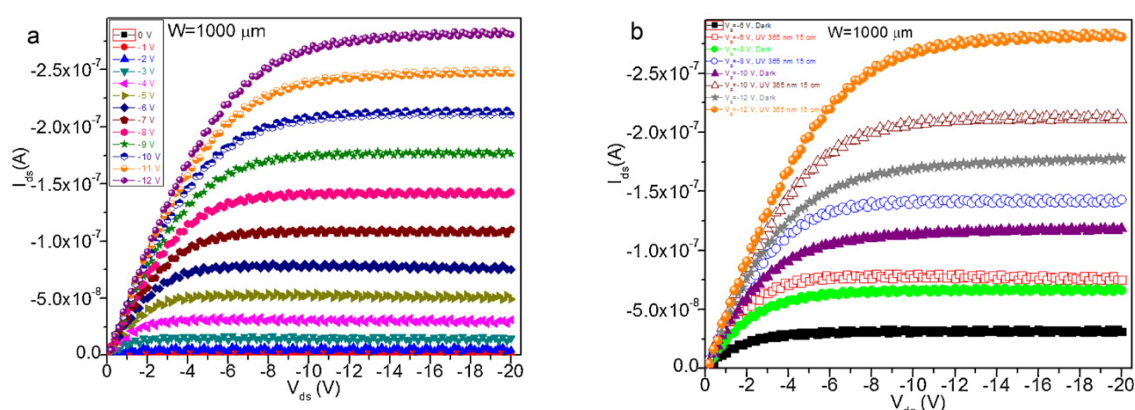


Figure 4.1 The output characteristics of the TIPS-pentacene-OTFT transistor (a) under UV and (b) comparison of the dark and UV conditions at various gate voltages. Figure taken from ref.⁷.

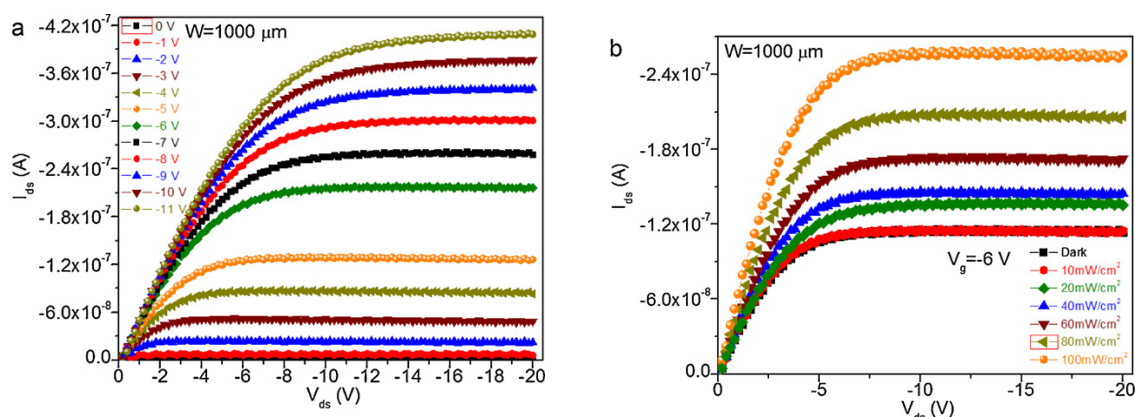


Figure 4.2 The output characteristics of the TIPS-pentacene-OTFT transistor (a) under 100 mW/cm² white light illumination and (b) comparison of the dark and white light illumination conditions at $V_g = -6$ V. Figure taken from ref.⁷.

Moreover, increased conductivity of pentacene single crystals under illuminations were reported by Jurchescu *et al.*⁷². In this report the effect of dry air and ambient air on

pentacene single crystals were studied in dark and under illumination. All these results also open up the possibility of using TIPS-pentacene as the active channel material in two-terminal photodetectors.

4.1.2 Experimental details

The HED-TIEs were prepared using the “trench-refill approach” as described in chapter 2. 800 nm of LPCVD silicon oxide layer was used as the trench-refill layer and 50 nm Au was deposited as the electrode layer with a 10 nm Cr layer as the adhesion layer. Devices with a channel width of 40 μm with two different channel lengths were chosen for the photosensing experiments: (i) 120 nm and (ii) 300 nm.

To investigate the photosensing properties, three different laser lines: 632.8 nm (1.96 eV, red), 514.7 nm (2.41 eV, green), and 325 nm (3.81 eV, ultraviolet) were used for illumination of the active area of the devices from the top. The electrical data were recorded as described in chapter 2, section 2.3 (a).

According to Davis *et al.*⁵⁴, TIPS-pentacene has higher absorbance in the ultraviolet spectral region compared to the visible region, as verified also for our TIPS-pentacene films drop-coated on quartz substrates. Figure 4.3 shows the UV-Vis spectra of a TIPS-pentacene film drop-coated on a quartz substrate. The three laser lines used in the photosensing experiments are indicated in the absorption spectra by dotted lines.

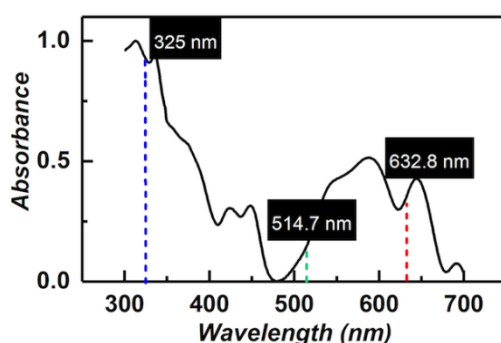


Figure 4.3 UV-Vis spectra of a TIPS-pentacene film drop-coated on quartz substrate.

The schematic diagram of the photosensing experiments is shown in Figure 4.4. The diameter of the circular illuminated area is ca. 40 μm for the red and green laser lines and ca. 200 μm for UV laser line respectively, due to the usage of objectives with different magnification. During the photosensing experiments, great care was taken that the Raman spectrum of the illuminated area did not change in time, as a proof that the TIPS-pentacene in the channel does not degrade under bias stress and light stimulus.

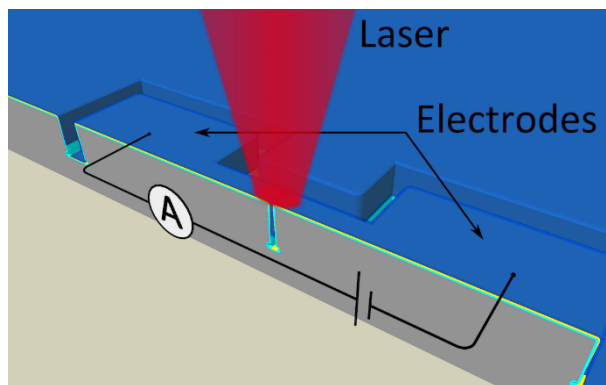


Figure 4.4 Schematic diagram of the photosensing experiments. The active channel of the fabricated HED-TIE is illuminated from top. Figure taken from ref.⁴⁰.

4.1.3 Results and discussions

The TIPS-pentacene HED-TIEs are found to generate photocurrents for all three illumination wavelengths. The observed photocurrent in a device can be a photovoltaic effect, a photoconductive effect or a combination of both. In case of the HED-TIEs, it was concluded that the observed photocurrent is purely due to the photoconductive nature of the devices. The possibility of the devices to exhibit photovoltaic effect was eliminated as: (i) the photocurrent vs voltage characteristics were found to be symmetric around 0 V and (ii) the devices did not show any current while illuminated at 0 V. Moreover, it was previously reported in literature that for TIPS-pentacene OFETs, the photoconductive effect dominates when no gate voltage is applied and the photovoltaic effect starts to dominate under an application of gate voltage⁷. An OFET can be considered as a two-terminal device when the gate terminal is at zero potential and hence similarly, the fabricated HED-TIEs are expected to exhibit photoconductive effect, not photovoltaic effect. The photocurrent density (J_{ph}), defined as the difference between the current density under illumination and in the dark, as described in equation (4.1), is plotted over the applied voltage range in figure 4.5 (a).

$$J_{ph} = J_{illumination} - J_{dark} \quad (4.1)$$

Similar to the current-voltage characteristics recorded in the dark (as discussed in chapter 3), the photocurrent density is higher in the case of the shorter channels for voltages above 1 V. For lower voltages, the longer channels generate more carriers and hence higher currents for the case without illumination or when illuminating in the absorption bands of the TIPS-pentacene (*i.e.* with red and UV light). The light on / light

off photo-switching of the TIPS-pentacene HED-TIEs was investigated by measuring the device currents over time, while the laser illumination is switched on and off at regular intervals of 30 s and the results are shown in Figures 4.5 (b) – 4.5 (d). The measurements were performed at a constant applied voltage of 0.5 V, in order to keep the applied bias stress on the organic channel as low as possible. The laser power densities used for the wavelengths 632.8 nm, 514.7 nm, and 325 nm are $7 \cdot 10^3 \text{ mWcm}^{-2}$, $8.3 \cdot 10^3 \text{ mWcm}^{-2}$, and $5.7 \cdot 10^2 \text{ mWcm}^{-2}$, respectively.

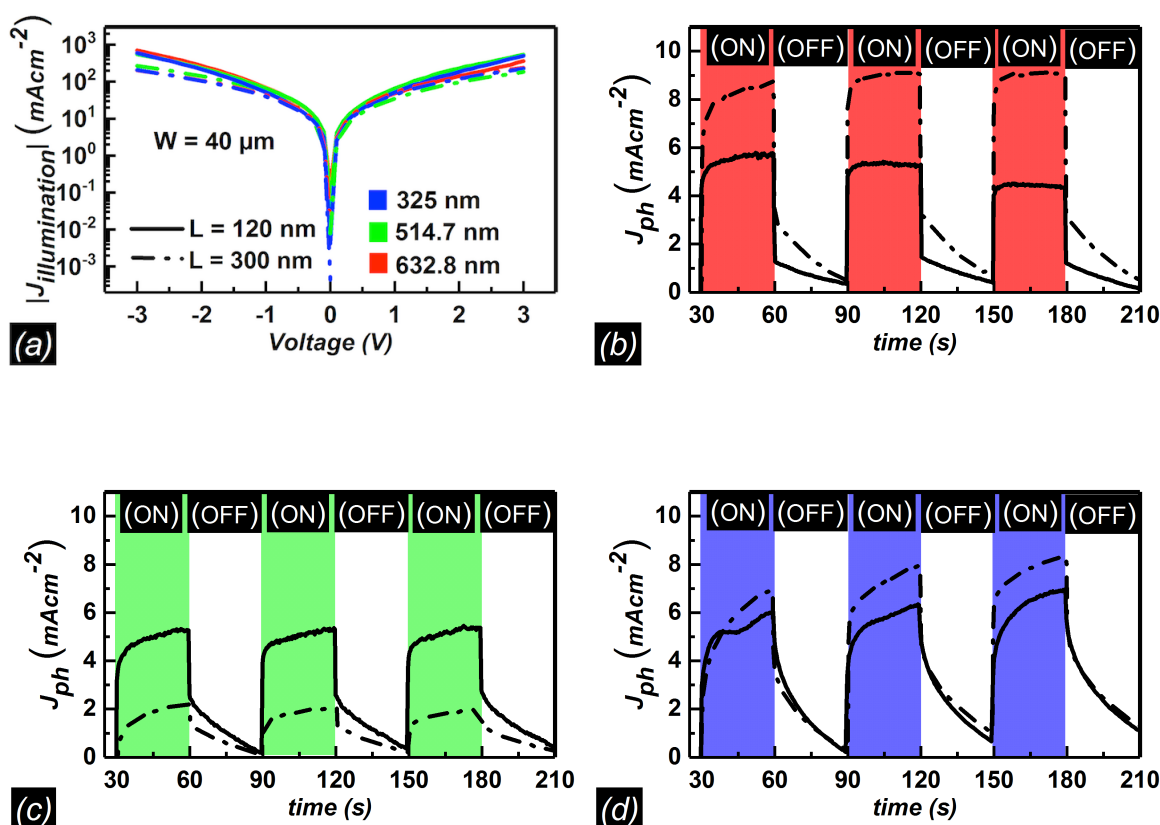


Figure 4.5 (a) Photocurrent density (J_{ph}) plotted over the applied voltage for three different laser lines. (b)-(d) J_{ph} over time at a constant bias voltage of 0.5 V, while the illumination was switched on and off every 30 s. Illumination wavelengths used are (b) 632.8 nm, (c) 514.7 nm, and (d) 325 nm. Figure taken from ref.⁴⁰.

After an initial fast rise, a slower increase in photocurrent is observed for the whole time interval when the illumination is kept on. This additional increase in photocurrent is almost negligible for red excitation but the effect becomes more pronounced with increasing the excitation energy. When the light is switched off, the photocurrent decreases within 30 s to nearly the value before switching the light on, whereby a first fast decrease occurs nearly instantaneously and is followed by a slower decay. The

photocurrent decay was fitted with a bi-exponential function, similar to the report by Li *et al.*⁷³ for the dynamic response of CdSe nano-dots in poly(3-hexylthiophene) (P3HT) matrix. Li *et al.*⁷³ suggested that the initial decay can be attributed to the imbalance in electron-hole mobilities resulting in a faster dynamic response related to the faster carriers followed by a slower response of the slower carriers in the channel material. The short time constants (τ_1) in the device with 120 nm/ 300 nm channel were found to be roughly ~ 0.15 s/ ~ 0.2 s, ~ 0.45 s/ ~ 0.7 s, and ~ 1.5 s/ ~ 0.45 s for 632.8 nm, 514.7 nm, and 325 nm respectively. Similar time constants are reported in literature for “instantaneous” switching response of photoactive materials under illumination^{74,75}. From the mobility of the carriers calculated for our devices, we expect, however, the carrier transit time in the channel to be in the range of nanoseconds. The time resolution in our experiment is, however, limited to ~ 0.1 s.

The slower photocurrent decay for the device with channel length of 120 nm/ 300 nm are characterized by the following time constants (τ_2): ~ 40 s / ~ 35 s, ~ 50 s/ ~ 45 s, and ~ 50 s/ ~ 50 s for 632.8 nm, 514.7 nm, and 325 nm respectively. This can be related to a process dominated by trapping and de-trapping of the charge carriers created during illumination. Figure 4.6 shows how the time constant of the photo-switching varies with the excitation wavelength. The error bars are calculated based on the error values generated by the fitting parameters.

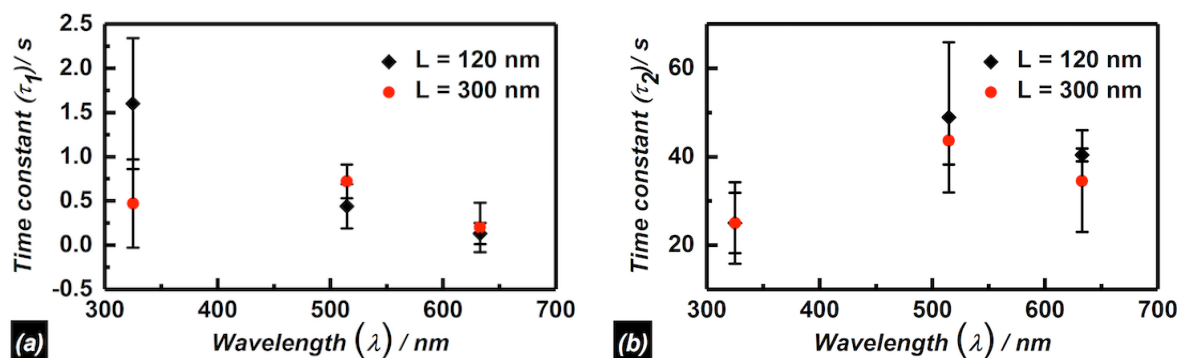


Figure 4.6 The variation of the time constant with the excitation wavelength. (a) τ_1 (the time constant responsible for the instantaneous device response) vs wavelength and (b) τ_2 (the time constant representing the slower photocurrent decay due to trapping and de-trapping of the carriers vs wavelength).

One possible reason for the rather long time-scale of this process might be photo-assisted oxygen diffusion into the film, as all our electrical and photosensing measurements were carried out in ambient atmosphere. Similar time constants were

reported by Grollman *et al.*⁷⁶ for the fluorescence decay in air for fluorinated and non-fluorinated TIPS-pentacene embedded in a polymer matrix under a 633 nm excitation. In ref.⁷⁶ the fluorescence quenching was nearly completely suppressed when the experiments were performed in vacuum. Jurchescu *et al.*⁷² showed, by measuring the transient current in pentacene crystals, that the oxygen diffusion in pentacene is associated with the creation of holes, and thus with the doping of the material. When pentacene is exposed to ambient air, water molecules can also diffuse into the pentacene layer creating traps. Ref.⁷² suggests that the balance between the holes and the traps created by ambient air can be influenced by illumination, as the efficiency of the oxygen exposure induced doping is increased by exposure to ambient fluorescent light. In ref.⁷⁷ it was shown that the diffusion of molecular oxygen and water from the ambient into pentacene is reversible when the air exposure takes place in the dark or under visible light. On the other hand, it was suggested, that the exposure to ambient under UV illumination (from a low pressure Hg lamp) leads to a reaction, most probably with singlet oxygen and/or ozone with the deterioration of the material within a time interval of 15 minutes.

Therefore, it was concluded that the different line-shape of the photocurrent time transient observed in the described photosensing experiments in case of UV as compared to green and red illuminations is most probably due to a more pronounced diffusion of the oxygen into the TIPS-pentacene channel. In order to cross-check the photo-oxidation of TIPS-pentacene by illumination with the 325 laser line, we employed an optical method: photoluminescence (PL) spectroscopy, since the PL intensity is highly sensitive to the molecular structure and environment. The PL spectra of the channel material is shown in figure 4.7.

The spectra were recorded at first in nitrogen ambient, then the sample space was purged with air and finally again by nitrogen. The area under the PL emission band of TIPS-pentacene is shown in figure 4.8 as a function of time. The time scale of PL and of the photo-switching measurements is different due to experimental constraints of the time required to purge the measurement stage with nitrogen or air. A waiting time of 10 min was maintained in each case to ensure that the experimental set up was properly purged with nitrogen or air.

The PL area remained almost constant as long as the measurement was performed in nitrogen ambient, while a rapid PL decrease occurred when the measurement was carried out in air. Once the stage was purged again with nitrogen, the PL intensity

slowly recovered to nearly the initial value. This kind of behaviour is consistent with a photo-oxidation the TIPS-pentacene UV exposure, which is, contrary to the report from ref.⁷⁷, reversible once the sample is purged again with nitrogen. We expect that the irreversibility of the photo-oxidation reported in ref.⁷⁷ is due to the broader UV spectrum and higher power of the Hg lamp.

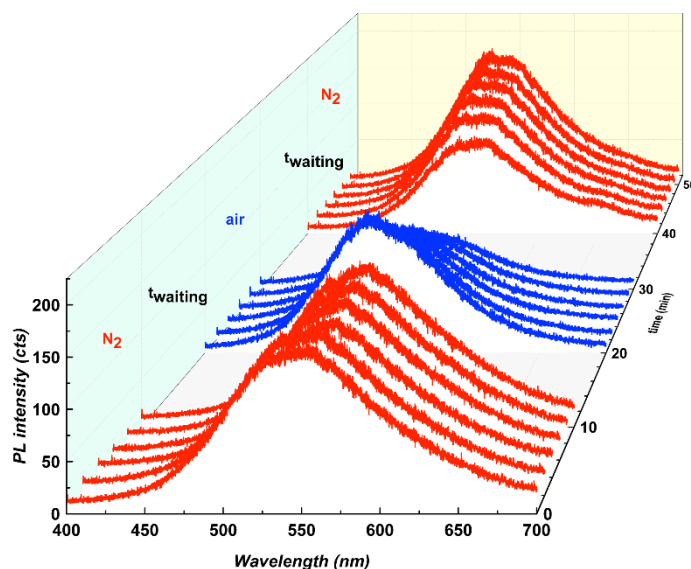


Figure 4.7 The photoluminescence spectra of the TIPS-pentacene channel. Excitation wavelength is 325 nm. A laser beam with the power of 180 μ W was focused on the HED-TIE channel using a 10x objective. Initial PL measurements were carried out in N₂ ambient followed by air and N₂ ambient again. Figure taken from ref.⁴⁰.

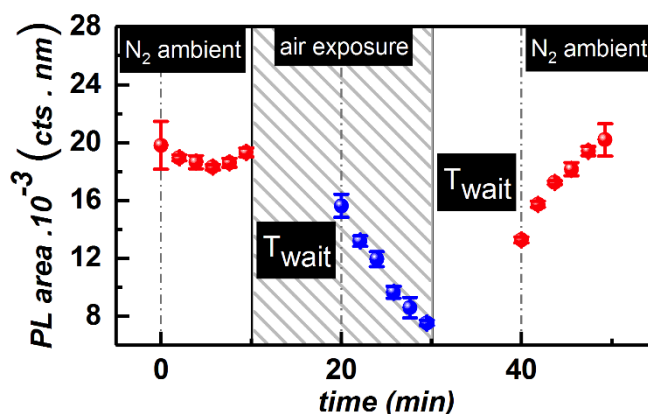


Figure 4.8 The area under PL spectra plotted over time to show the decay in PL intensity while the channel material is exposed to air. Figure taken from ref.⁴⁰.

The photo-oxidation of the TIPS-pentacene under UV exposure underlines another aspect where the full accessibility of the active transport channel in HED-TIEs to

external stimuli can play an important role: namely for gas sensing applications. TIPS-pentacene based devices were already demonstrated as ammonia gas sensors by Yu *et al.*²³

4.1.4 Summary and outlook

One key feature of the proposed HED-TIE technology is the full accessibility of the active area of the devices to external stimuli (*e.g.* light) which can be useful for various sensing applications. In this part of the chapter, photosensing properties of TIPS-pentacene HED-TIEs have been demonstrated. In principle, HED-TIEs with any photosensitive material as the active channel material can have applications as hybrid photodetectors. Three different illuminations were used to investigate the photosensing properties. The laser lines used for illumination were 632.8 nm (1.96 eV, red), 514.7 nm (2.41 eV, green), and 325 nm (3.81 eV, ultraviolet). HED-TIEs were found to generate photocurrent for all three illuminations.

The red illumination was found to generate highest intensity of photocurrent and also the switching was the fastest for red illumination. After an initial fast rise, a slower increase in photocurrent was observed for the whole time interval when the illumination is kept on. This additional increase in photocurrent was almost negligible for red excitation but the effect became more prominent with increasing the excitation energy. This was attributed to the photo-oxidation of TIPS-pentacene as all the measurements were carried out in air. Photoluminescence spectroscopy showed this photo-oxidation to be a reversible phenomenon when purged with nitrogen.

The results discussed above suggests that fabricated TIPS-pentacene HED-TIEs can be used as hybrid photodetectors to be used in the red wavelength regime. Higher excitation energies can lead to a prominent photo-oxidation effect, affecting the switching properties of the devices and thus reducing the suitability of the fabricated HED-TIEs to be used as hybrid photodetectors.

The results discussed above are summarized in the table below. The table represents the photocurrent density at a constant applied bias and the switching time constant of devices (when the illumination is switched off) with two different channel lengths and under three different single wavelength illuminations.

Device channel length	Illumination wavelength		
	325 nm	514.7 nm	632.8 nm
120 nm	$J_{ph} = 6 \text{ mAcm}^{-2}$ $\tau_1 = 1.5 \text{ s}$	$J_{ph} = 5 \text{ mAcm}^{-2}$ $\tau_1 = 0.45 \text{ s}$	$J_{ph} = 6 \text{ mAcm}^{-2}$ $\tau_1 = 0.15 \text{ s}$
300 nm	$J_{ph} = 7 \text{ mAcm}^{-2}$ $\tau_1 = 0.45 \text{ s}$	$J_{ph} = 2 \text{ mAcm}^{-2}$ $\tau_1 = 0.7 \text{ s}$	$J_{ph} = 9 \text{ mAcm}^{-2}$ $\tau_1 = 0.2 \text{ s}$

Table 4.1 Summary of the photosensing properties of the TIPS-pentacene HED-TIEs of two different channel lengths and under three different single wavelength illumination. All the J_{ph} mentioned are measured at a fixed bias of 0.5 V.

4.2 Photosensing properties of TIPS-pentacene based HED-TIEs with Au nanoparticles in the channel matrix

4.2.1 Theoretical background

With the advancement of organic electronics in last few decades, hybrid inorganic/organic nanocomposites have emerged as promising candidates for various applications in next-generation electronic, optoelectronic or memory devices^{78,79}. The organic matrix can be based on small molecules or polymers whereas nanoparticles can be metal nanoparticles or some other materials based on the proposed application. Metal nanoparticles are attractive for optical detection applications and they can easily be processed from colloidal dispersions. Colloidal particles offer a route to the simple assembly of complex structures and can be used to create a variety of electronic and sensor components. Many colloidal nanoparticle syntheses have been known for a considerable amount of time^{80,81} but, more recently, dedicated works have been carried out for nanoparticle syntheses specifically for device applications. These particles may consist of a particular material, be of a particular size, or have specialized surface functionality⁷⁹. It has even become possible to have some degree of control over the shape of the nanoparticles⁸². Nanoparticles tend to be fairly unstable in solution and tend to agglomerate. Special precautions have to be taken to avoid the aggregation or precipitation of these synthesized nanoparticles. Nanoparticle syntheses also involves the use of a stabilizing agent, which associates with the surface of the particle, provides charge or solubility properties to keep the nanoparticles suspended, and thereby prevents the agglomeration of the

nanoparticles. Once the nanoparticles are synthesized, it is extremely important to investigate the stability and degradation of the synthesized nanoparticles over time for successful device operations.

The devices with hybrid metal nanocomposite films exhibit phenomena such as absorption of ultraviolet light, plasmonic enhancement of absorption, size-based spectral tuning *etc.* and the charge storage properties of these nanoparticles at the surface or the interface, can also play an important role in fabrication nanocomposite based memory devices. After demonstrating the possible application of the solution processed TIPS-pentacene based HED-TIEs as hybrid photodetectors, it was worth investigating whether the photosensing properties of these devices can be further tuned by incorporating metal nanoparticles in the TIPS-pentacene matrix.

4.2.2 Experimental details

The fabricated HED-TIEs used in this experiments were prepared using the “spacer approach” as described in chapter 2. Thermally grown SiO₂ with a thickness of 130 nm was used as the isolation layer and 30 nm Au was deposited as the electrode layer with a 10 nm Cr as the adhesion layer. The TIPS-pentacene solution was prepared as described section 2.2.1.1 in chapter 2.

Colloidal gold nanoparticles in ethanol dispersion, provided by Alexandra Raevskaya from University of Kiev, Ukraine, was then mixed with the prepared TIPS-pentacene solution in 1:1 ratio. The gold nanoparticles with a concentration of 200 mg/l were stabilized with polyethyleneamine and ascorbic acid and dispersed in ethanol. The concentration of ascorbic acid was kept constant at 200 mg/l. The concentration of polyethyleneamine was varied for two different nanoparticle sizes as 200 mg/l (Au NP_1) and 170 mg/l (Au NP_2) respectively. For simplicity, these two types of gold nanoparticles will be referenced as Au NP_1 and Au NP_2 in the rest of the chapter. The dynamic light scattering measurement performed by the cooperation partners indicated the average diameter of the nanoparticles to be ~30 nm and ~60 nm for Au NP_1 and Au NP_2, respectively.

Prior to drop-coating, the fabricated structures with gold electrodes were cleaned using acetone, ethanol, and deionized water respectively. 3 µl of solution mixture with 1.5 µl of TIPS-pentacene solution and 1.5 µl of gold nanoparticle dispersion was used to drop-coat the HED-TIEs for a 1 cm x 1 cm area for both samples. The drop-coating of the substrates was performed at 65 °C on a hot plate and the samples were kept at

65 °C for 30 min after drop-coating, similarly to the procedure used for pure TIPS-pentacene channels, in order to initiate crystallization of the TIPS-pentacene matrix and to ensure evaporation of the solvents from the film. Additionally, a reference sample was prepared with TIPS-pentacene solution diluted in ethanol (1:1 ratio) to compare the observed photosensing properties of the TIPS-pentacene HED-TIEs with and without gold nanoparticles in the channel.

For all the devices, the channel length was maintained constant at ~140 nm and the channel width was 100 μm . To investigate the photosensing properties, two different laser lines: 632.8 nm (1.96 eV, red), and 514.7 nm (2.41 eV, green) were used for illumination of the active area of the devices from the top. These two wavelengths were chosen to meet the absorption of the metal nanoparticles along with that of TIPS-pentacene (see next section). The electrical measurements were conducted in the same way as described in chapter 2, section 2.3 (a).

4.2.3 Results and discussions

Figure 4.9 shows the size distribution of the synthesized gold nanoparticles based on the dynamic light scattering technique. The average size of the gold nanoparticles were ~30 nm diameter size for Au NP_1 and ~60 nm diameter size for Au NP_2.

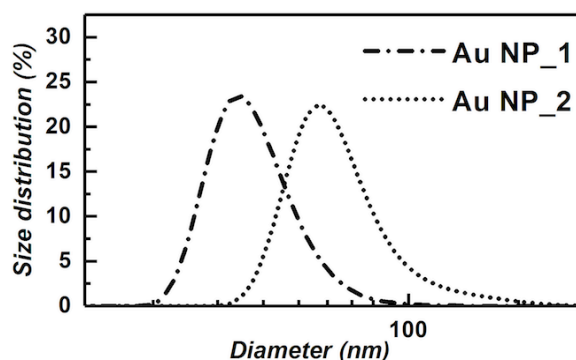


Figure 4.9 Size distribution of the synthesized gold nanoparticles.

The absorption spectra of the gold nanoparticles and the TIPS-pentacene solution are shown in figure 4.10. The two laser lines used in the photosensing experiments are indicated by the dotted vertical lines in the spectra.

Firstly, the current-voltage characteristics of all the fabricated devices were measured in dark and figure 4.11 shows the current-voltage characteristics of the HED-TIEs with and without gold nanoparticles in the TIPS-pentacene matrix.

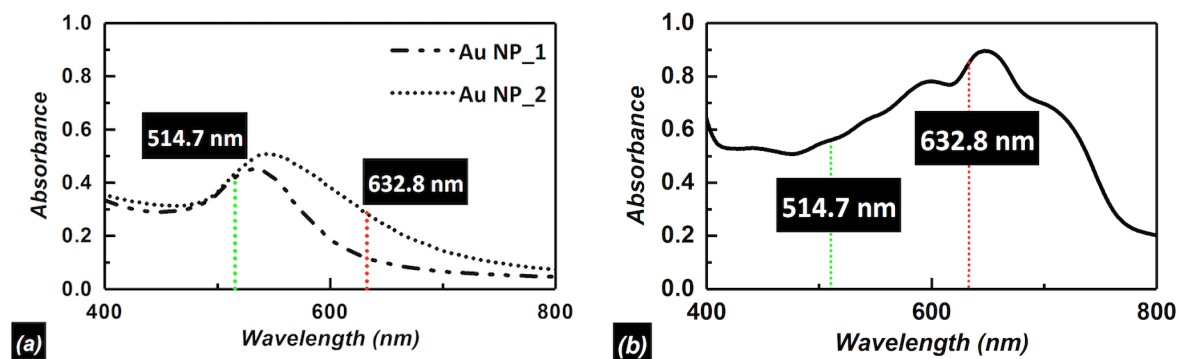


Figure 4.10 Absorption spectra of: (a) gold nanoparticles and (b) TIPS-pentacene. The green and red lines indicate the laser lines used for the photosensing experiments.

It also shows how the device characteristics change when TIPS-pentacene solution is diluted in ethanol. It can clearly be seen that the line-shape of the measured characteristics is different in the presence of the nanoparticles, indicating a different conduction mechanism. These line-shapes were not always reproducible when the same device was measured repeatedly. One possible reason for the change of I - V characteristics with time might be the movement of the gold nanoparticles in the channel matrix under applied bias, influencing the overall device current and hence the line-shape. The asymmetric behaviour of current-voltage characteristics of the sample with TIPS-pentacene solution diluted in ethanol (i.e. without gold nanoparticles) was reproducible, as it will be discussed in the following section. However, the electrical conductivity was found to increase when the TIPS-pentacene was diluted in ethanol.

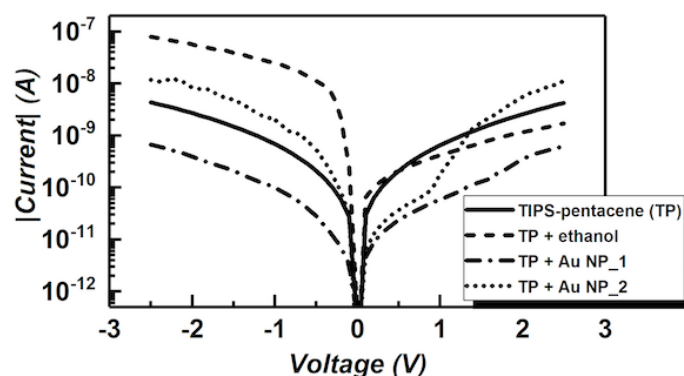


Figure 4.11 Exemplary current-voltage characteristics of TIPS-pentacene based HED-TIEs with and without gold nanoparticles in the channel.

To verify whether the observed asymmetry in the HED-TIE with TIPS-pentacene diluted in ethanol is a device property or a measurement artefact, the positive and

negative terminal of the device were swapped with each other and re-measured. The results are shown in Figure 4.12.

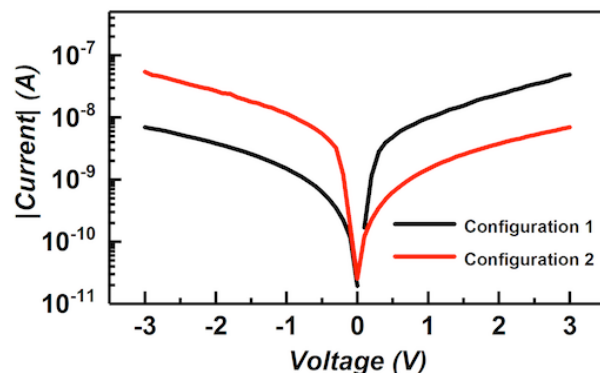


Figure 4.12 Current-voltage characteristics of TIPS-pentacene based HED-TIEs diluted in ethanol for two different configurations of the voltage terminals.

The observed asymmetry was found to change the direction indicating it to be indeed a device property, not a measurement artefact. This effect was reproducible for multiple samples prepared with different TIPS-pentacene solutions diluted in ethanol. That clearly indicates the observed asymmetry is due to a change in the transport properties of TIPS-pentacene when mixed with ethanol. It should also be mentioned here that the observed asymmetry in the sample with TIPS-pentacene diluted in ethanol was not due to a “diode like” behaviour of the devices as there was no shift observed around 0 V when the device active area was illuminated. It needs further investigation for a conclusive explanation behind the observed asymmetry in current-voltage characteristics when TIPS-pentacene is diluted in ethanol. One possible explanation would be that eventually remaining ethanol molecules in the channel act as traps for the carriers and this might lead to a change in the transport mechanism from unipolar to bipolar for a particular voltage regime, resulting in increase in device current due to contribution from both type of carriers. The fact that the overall conductivity of the devices increase when diluted in ethanol also supports the fact of formation of traps in the channel matrix.

Figure 4.13 shows how the electrical characteristics vary in dark and under illumination for all the samples. The TIPS-pentacene based HED-TIEs and the HED-TIEs with gold nanoparticles in the channel matrix were found to generate photocurrent under both green and red illuminations. When TIPS-pentacene was diluted in ethanol, the amount of generated photocurrent was negligible.

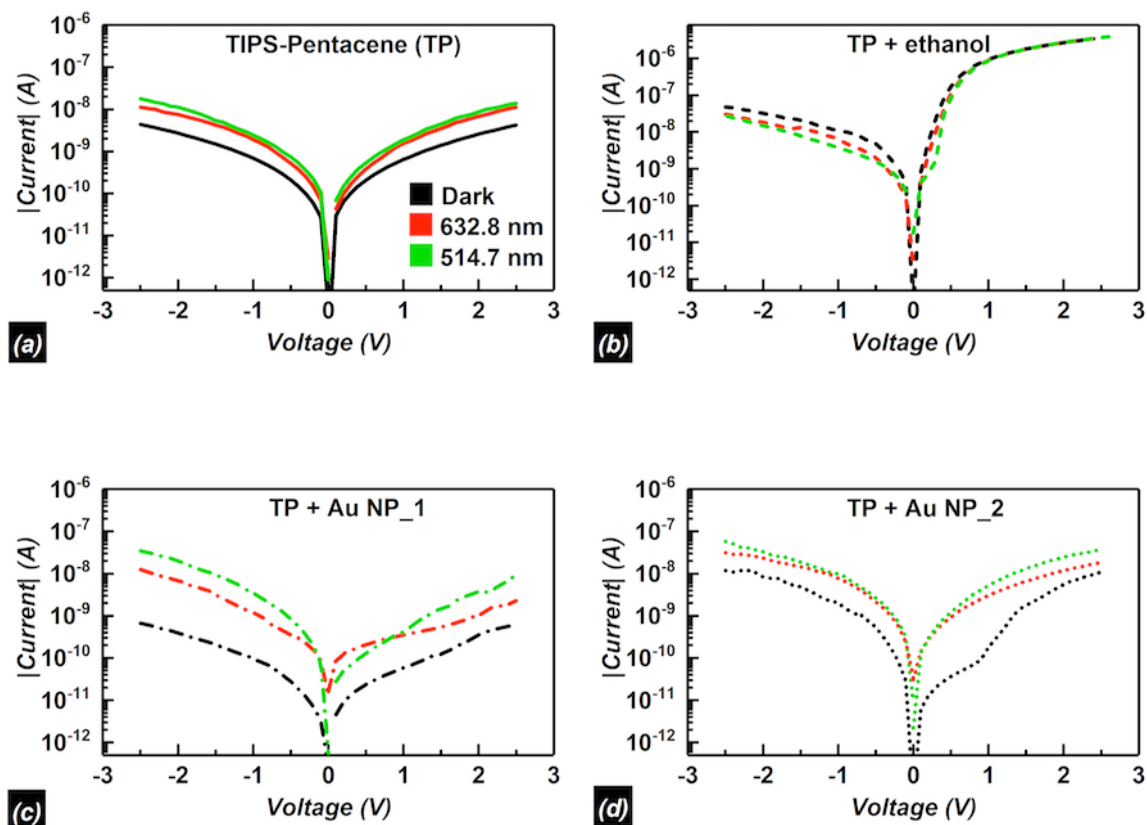


Figure 4.13 Current-voltage characteristics in dark and under red and green illumination: (a) TIPS-pentacene based HED-TIE, (b) TIPS-pentacene based HED-TIE with Au NP_1, (c) TIPS-pentacene based HED-TIE with Au NP_2 and (d) HED-TIE with TIPS-pentacene solution diluted in ethanol.

The light on / light off photo-switching of the all the fabricated HED-TIEs was investigated by measuring the device currents over time, while the laser illumination is switched on and off at regular intervals of 30 s and the results are shown in figures 4.14 – 4.17. The measurements were performed at a constant applied voltage of 1 V, in order to keep the applied bias stress on the organic channel as low as possible. The laser power densities used for 632.8 nm and 514.7 nm are $7 \cdot 10^3 \text{ mWcm}^{-2}$ and $8.3 \cdot 10^3 \text{ mWcm}^{-2}$, respectively.

The TIPS-pentacene based HED-TIE without gold nanoparticles in the channel matrix showed better photo-switching properties under green illumination, unlike the HED-TIEs as discussed in section 4.1.3. As shown in figure 4.14, the photocurrent density was higher for green illumination and the change with the switching on and off of the voltage was found to be much stronger compared to the photo-switching under red illumination. This difference can be due to the difference in the device geometry, leading to different type of trench-filling with the solution resulting in difference in the

absorption of the light or the photosensing properties.

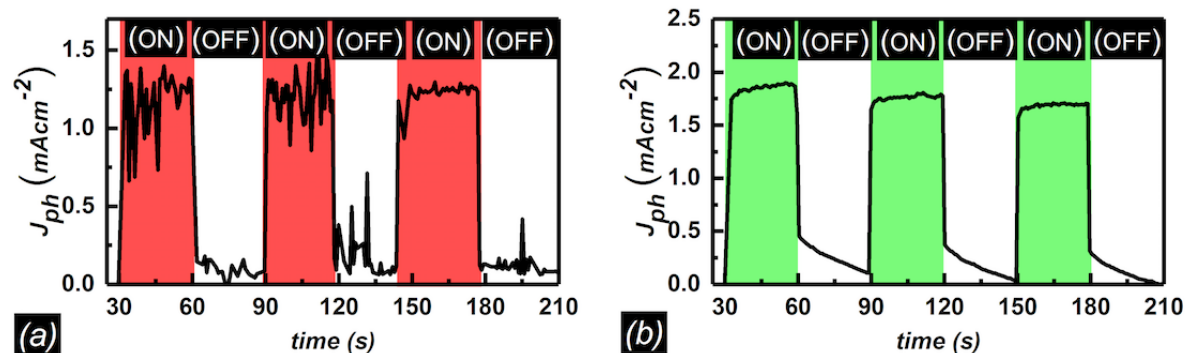


Figure 4.14 J_{ph} over time for TIPS-pentacene based HED-TIE at a constant bias voltage of 1 V, while the illumination was switched on and off every 30 s. Illumination wavelengths used are (a) 632.8 nm and (b) 514.7 nm.

When the HED-TIEs are fabricated with TIPS-pentacene solution diluted in ethanol, the photosensing properties deteriorate drastically. In this case, as shown in figure 4.15 (a), the device does not show any photo-switching under red illumination. When the device is illuminated with a green laser, there is a photo-switching observed but the intensity of the photocurrent density reduces by a factor of 4, compared to the HED-TIEs prepared with TIPS-pentacene without ethanol in the solution. This fact supports the hypothesis of the traps contributing to the electrical transport and thereby changing the transport mechanism. The photosensing properties of the samples prepared with ethanol in the solution is perhaps deteriorated because of the presence of more number of traps in the film. It is important to investigate the photo-switching properties of the devices prepared with ethanol in the solution mixture, as it will help us to compare the device properties with the gold nanoparticles in the channel matrix. The gold nanoparticles are dispersed in ethanol and hence by comparing the device characteristics with the gold nanoparticles in the channel matrix and the device prepared with solution diluted in ethanol, it can be concluded whether the photo-sensing properties are indeed dominated by the absorption of the gold nanoparticles, rather than by the absorption of the TIPS-pentacene matrix. It is also believed that conductivity of a device with gold nanoparticles in the channel matrix is not influenced by the conductivity of the gold nanoparticles itself because of the presence of the surfactants around the nanoparticles.

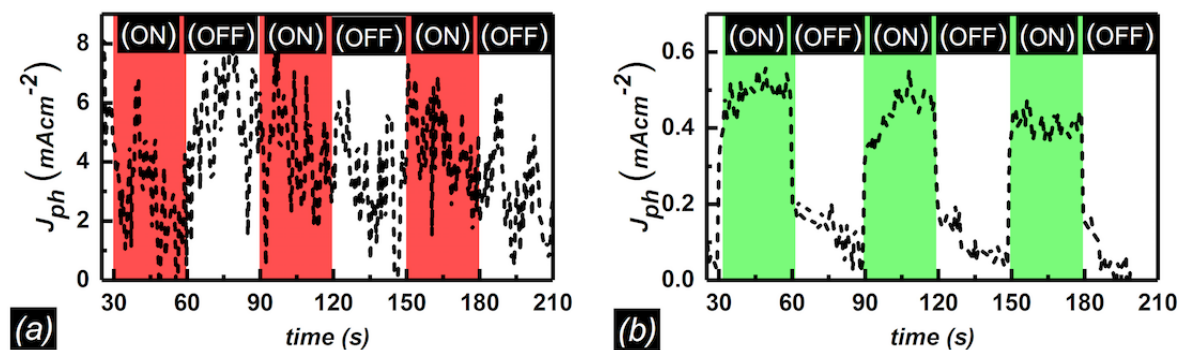


Figure 4.15 J_{ph} over time for TIPS-pentacene based HED-TIE, with TIPS-pentacene diluted in ethanol, at a constant bias voltage of 1 V, while the illumination was switched on and off every 30 s. Illumination wavelengths used are (a) 632.8 nm and (b) 514.7 nm.

When Au NP_1 (diameter of ~ 30 nm) is added in the channel matrix, the devices show better photo-switching properties for red illumination compared to green illumination and the measurement data is shown in figure 4.16. Though the intensity of photocurrent was higher for green illumination, the line-shape was found to be noisier and less steep compared to the switching line-shape obtained for red illumination. The drastic improvement in the photo-switching properties under red illumination compared to the HED-TIE prepared with TIPS-pentacene solution diluted in ethanol (as shown in figure 4.15 (a)) indicates that the photo-switching properties can be tuned by adding nanoparticles in the channel matrix.

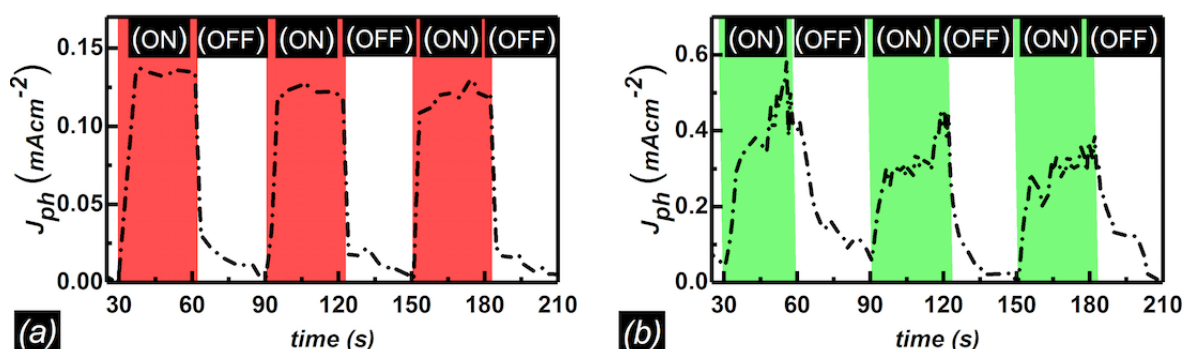


Figure 4.16 J_{ph} over time for TIPS-pentacene based HED-TIE with Au NP_1 in the channel matrix, at a constant bias voltage of 1 V, while the illumination was switched on and off every 30 s. Illumination wavelengths used are (a) 632.8 nm and (b) 514.7 nm.

When Au NP_2 (diameter of ~ 60 nm) is added in the channel matrix, the devices exhibit a higher photocurrent compared to devices with Au NP_1. The obtained data is shown in figure 4.17. The line-shape of the switching improves in this case for green

illumination, whereas the line-shape deteriorates under red illumination compared to Au NP_1 in the channel matrix.

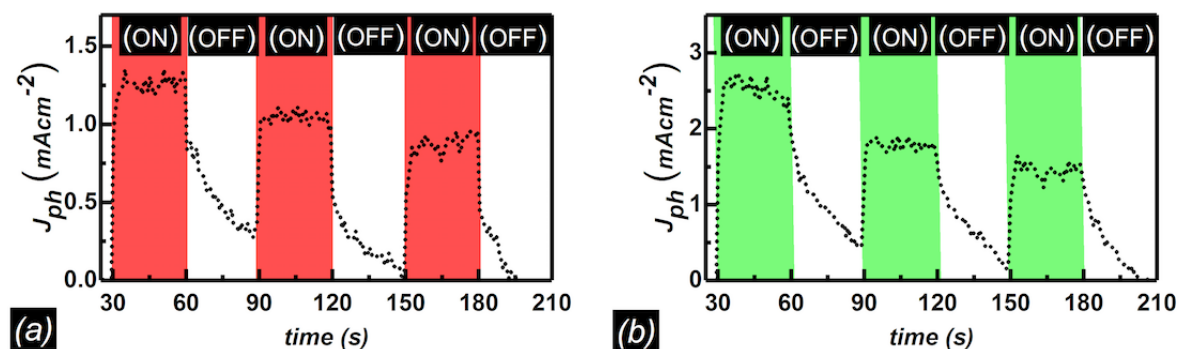


Figure 4.17 J_{ph} over time for TIPS-pentacene based HED-TIE with Au NP_2 in the channel matrix, at a constant bias voltage of 1 V, while the illumination was switched on and off every 30 s. Illumination wavelengths used are (a) 632.8 nm and (b) 514.7 nm.

The photocurrent density is higher for green illumination for both type of nanoparticles perhaps because of higher absorption in green wavelength regime for both nanoparticles (please see figure 4.10 (a)). It should also be noted that the number of nanoparticles can vary from sample to sample as the samples are prepared from nanoparticle dispersions, leading to variations in the photosensing properties. However, the devices with gold nanoparticles were found to degrade after approximately two months of sample preparation. The devices did not exhibit any photo-switching properties in that case, whereas the devices without gold nanoparticles in the channel matrix were still functional. This implies, the nanoparticles with the surfactants are perhaps not stable, which affects the device performance. To make devices with tuneable photosensing properties by adding metal nanoparticles in the channel matrix, the stability of the nanoparticles has to be taken care of for successful device operation.

The above discussed results suggest that photosensing properties of fabricated HED-TIEs can be tuned further by incorporating metal nanoparticles in the channel matrix. The photosensing properties would of course depend on the size of the nanoparticles and hence the absorption properties of the nanoparticles and also on the dispersion and the surfactants used.

4.2.4 Summary and outlook

In this part of the chapter, gold nanoparticles were added in the TIPS-pentacene channels of the fabricated HED-TIEs and investigations were carried out to understand how the photosensing properties evolve when the gold nanoparticles are added in the channel matrix. Two different sizes (30 nm and 60 nm diameter sizes) of nanoparticles were used for this experiment and the photosensing properties were investigated by 632.8 nm (1.96 eV, red) and 514.7 nm (2.41 eV, green) laser lines. The nanoparticles were added in the TIPS-pentacene solution from an ethanol dispersion and drop-coated on the pre-structured HED-TIE substrates. It was found the photosensing properties can be further tuned by adding these metal nanoparticles in the channel matrix. The photo-switching line-shape and the photocurrent density depend on sizes of the nanoparticles used. The variations in the number of nanoparticles in device channels (due to solution processing) can also affect the photosensing properties of the devices. However, the nanoparticles were found to be degrading over time resulting in disappearance of the photosensing properties of the fabricated HED-TIEs. The stability of the nanoparticles in the dispersion has to be taken care of for successful fabrication of functional HED-TIEs with tuneable photosensing properties. As an alternative, the nanoparticles can be dispersed in different solvent other than ethanol and studied to check whether the stability of the devices improves.

As an outlook to further research work, HED-TIEs with different photosensitive channel materials can be studied under different illuminations to fabricate hybrid photodetectors working in different wavelength regimes.

Another possible application of the TIPS-pentacene based HED-TIEs with gold nanoparticles in the channel matrix would be fabrication of memory devices. In ref.⁸³, Park *et al.* demonstrated high-performance organic charge trap flash memory devices based on ink-jet printed TIPS-pentacene transistors by embedding gold nanoparticles in the devices. Similar devices can be fabricated using the HED-TIE structures and possibly by using the substrate as a gate electrode. The photocurrent density for all the samples discussed above, in terms of photocurrent densities, is summarized in the table below.

<i>Device channel material</i>	<i>Illumination wavelength</i>	
	632.8 nm	514.7 nm
TIPS-pentacene	$J_{ph} = 1.25 \text{ mAcm}^{-2}$	$J_{ph} = 2 \text{ mAcm}^{-2}$
TIPS-pentacene diluted in ethanol	No photoswitching	$J_{ph} = 0.5 \text{ mAcm}^{-2}$
TIPS-pentacene + Au NP_1	$J_{ph} = 0.125 \text{ mAcm}^{-2}$	$J_{ph} = 0.5 \text{ mAcm}^{-2}$
TIPS-pentacene + Au NP_2	$J_{ph} = 1.25 \text{ mAcm}^{-2}$	$J_{ph} = 2.5 \text{ mAcm}^{-2}$

Table 4.2 Summary of the photosensing properties of the TIPS-pentacene HED-TIEs with and without gold nanoparticles in the channel matrix and under two different single wavelength illumination. All the J_{ph} mentioned are measured at a fixed bias of 1 V.

Chapter 5

Application of HED-TIEs as magnetoresistive sensors

In this chapter, the magnetoresistive properties of solution-processed TIPS-pentacene HED-TIEs are investigated. It is shown, that this material can exhibit light induced organic magnetoresistance at room temperature and under ambient conditions even if the film is not encapsulated. Organic magnetoresistance is also shown in solution-processed TIPS-pentacene based commercial bottom contact OFETs and the advantages of the shorter transport channel in HED-TIEs compared to OFETs are discussed. The results discussed in this chapter was published in ref.⁸⁴.

5.1 Theoretical background

5.1.1. Organic spintronics

The field of organic spintronics has received lot of research interest in the last years due to the possibility of designing nano-scalable molecule-based multi-functional devices^{1,85}. Spintronics deals with controlling and applying the electron spin degree of freedom through a variety of spin-dependent phenomena and has several applications in the area of magnetic sensors, magnetic data storage devices^{86,87} *etc.* In molecular spintronics, spin-polarized currents are carried through organic molecules. The most attractive feature of molecular spintronics is the weak spin scattering mechanism which implies the spin polarization of the carriers can be maintained for a longer time (~in the range of μs)¹ compared to the inorganic semiconductors (~in the range ns to ps)^{88,89}. The fact that carbon is a light element, and hence it has a weak spin-orbit interaction, leads to longer spin lifetimes. This is because, the strength of spin orbit interaction is proportional to Z^4 (Z: atomic number) and carbon is an element with a low atomic number¹. Spin relaxation time in organic devices was found to be improved by orders of magnitude compared to spin devices using inorganic materials. Most importantly, these molecules can be functionalized according to the requirements, which allows us to modify their electronic and magnetic properties.

The most common type of spintronic device is a spin-valve structure where a non-magnetic spacer layer is sandwiched between two ferromagnetic electrodes⁹⁰. The role of the spacer layer is to decouple the ferromagnetic electrodes, allowing spin transport from one contact to the other. The two ferromagnetic electrodes can be

chosen with two distinct switching fields, so that under an applied magnetic field, the device can be switched between a parallel and antiparallel magnetization configuration. These parallel and anti-parallel magnetization configurations lead to a significant difference in the device resistance which is known as the giant magnetoresistance (GMR)^{91,92}. Fert⁹³ and Grünberg⁹⁴ demonstrated the existence of GMR and were awarded the Nobel prize in 2007 for their pioneering work. In case of an organic spin-valve device, this spacer layer is an organic material which is sandwiched between two ferromagnetic electrodes. GMR in organic spintronic devices (OSPD) was successfully demonstrated for devices with different organic materials¹. The first report on experimental injection in OSPDs was published in 2002 on a planar device⁹⁵ that had ferromagnetic electrodes and an organic semiconductor (Sexithiophene or 6T) as the channel material with channel length ranges between 100 nm - 500 nm. $\text{La}_{0.7}\text{Sr}_{0.3}\text{MnO}_3$, or LSMO, a well-known material for its spin-injection properties was used as the ferromagnetic electrode in this report. A strong magnetoresistance was observed up to room temperature in the devices with channel length of 100 nm – 200 nm. It was demonstrated that, to have successful spin transport between electrodes, it is necessary to have devices with channel length of less than ~300 nm. Electron beam lithography (EBL) was used in this case for fabrication of electrode gaps of 100 nm - 500 nm. Figure 5.1 shows the LSMO/6T/LSMO planar device structure and the channel length dependence of the magnetoresistance of such devices.

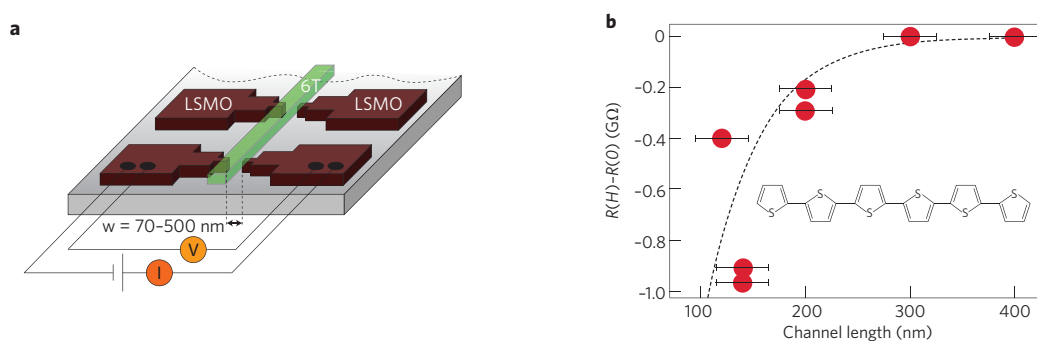


Figure 5.1 (a) LSMO/6T/LSMO planar spintronic device as published by Dediu *et al.* in ref.⁹⁵. Electron beam lithography was used for patterning electrode gap dimensions of 100 nm – 500 nm. (b) Magnetoresistance as a function of device channel length at applied magnetic field of 0.3 T. Figures taken from ref.⁹⁵.

Following this, fabrication of a vertical spin-valve structure was reported where aluminium-tris-(8-hydroxyquinoline) or Alq_3 layer (100 nm - 200 nm) was used as the

channel material, sandwiched between LSMO and cobalt electrodes⁹⁶. Tunnelling magnetoresistance (TMR) was also demonstrated in OSPDs for various systems consisting of different electrodes and/or organic channel materials^{97,98}. These discoveries opened up possibilities to explore the spin transport in the molecular level for coming up with novel hybrid device concepts. There are controversies regarding whether the observed magnetoresistance in organic spin-valves are due to successful spin transport through the layer or it is sort of a tunnelling through thin regions^{99,100}. The main disadvantages of molecular spintronic devices are, most of the magnetoresistance effects are observed below room temperature (down to ~4K) and have to be measured in controlled environments to avoid the influence of the ambient atmosphere on the organic channel material and hence these devices are not suitable for practical applications. Among the various reports on spin transport and/or magnetoresistive measurements in molecule based devices, the reports regarding the organic magnetoresistance (OMAR) are particularly interesting, because this effect can be observed at room temperature and in low magnetic fields of several mT^{101,33}. Most of the studies on OMAR have been carried out mainly on vertical devices^{102,103,104} where the active organic layer is sandwiched between two electrodes. Saragi *et al.* carried out studies on the magnetic field effect on three terminal bottom contact organic field effect transistors (OFET) and showed the existence of light induced magnetoresistance effect in pentacene¹⁰⁵ and one of its derivative 6,13 – bis(triisopropylsilylethynyl) or commonly known as TIPS-pentacene¹⁰⁶. In both cases, the molecules were deposited using thermal evaporation in vacuum with a base pressure of $\sim 10^{-7}$ Torr and a film thickness of $\sim 75 \pm 3$ nm. The devices were illuminated by a Tungsten - Halogen lamp with emission at 671 ± 7 nm wavelength. Systematic investigations were carried out to study the influence of applied gate voltage on the magnetoresistance of the device in these two reports. Figure 5.2 shows the results reported in ref.¹⁰⁶ as demonstration of light induced magnetoresistance in TIPS-pentacene OFETs. It also clearly shows the absence of the magnetoresistive effects in such devices when measured in dark. Possible mechanism behind this observed MR effect was also discussed in this report. It was concluded that the observed effect is due to presence of electron-hole pairs under illumination.

Even though OMAR has been a widely investigated topic in the last few years, most of the studies on OMAR in small molecules reported so far dealt with thermally evaporated molecules and were carried out under controlled atmosphere like nitrogen

purged glove box or a cryostat to prevent the degradation of the devices in ambient atmosphere (see, for example ref.^{102,105,106}). In this chapter, light induced magnetoresistance in solution processed planar hybrid devices is demonstrated which is measured at room temperature and most importantly, under ambient atmosphere. TIPS-pentacene is an ideal candidate for this proof of concept, as it is a solution processable molecule, which exhibits high carrier mobility and air-stability^{5,6}. Moreover, the existence of light induced magnetoresistance in TIPS-pentacene was already shown for thermally evaporated films by Saragi *et al.*¹⁰⁶ as discussed above.

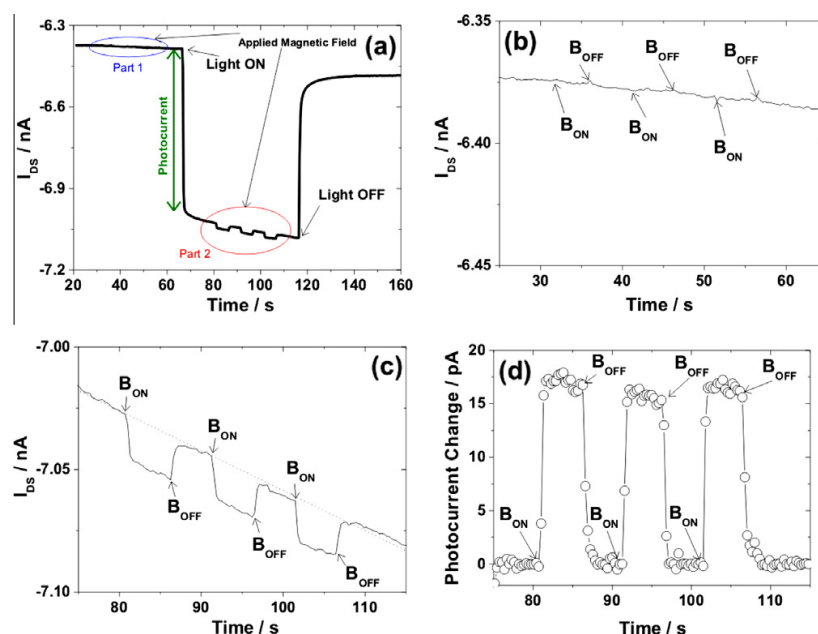


Figure 5.2 (a) Magnetoconductance in TIPS-Pentacene OFET recorded at $V_{DS} = -2$ V and $V_G = 0$ V, measured under illumination and external magnetic field (60 mT). (b) Zoomed in view of part 1 showing the dark current measured under influence of magnetic field. (c) Zoomed in view of part 2 showing the photocurrent measured under influence of magnetic field. (d) The corresponding photocurrent change when the light is kept on. Figures taken from ref.¹⁰⁶.

In order to investigate the influence of the distance between two electrodes on the OMAR magnitude and on the timeline of the OMAR response to the switching of magnetic field, we used two planar lateral device geometries: i) commercially available micro-structured bottom contact OFET substrates as used in ref.¹⁰⁶ to compare the results obtained from solution processed devices with the previously reported results for evaporated TIPS-pentacene and ii) HED-TIE devices as developed in this work and discussed in the previous chapters.

Negative magnetoresistance (positive magnetoconductance) was observed for both types of devices similar to the observations in ref.¹⁰⁶. The magnetoresistance effect, however, was found to degrade with the time, significantly faster than the photocurrent.

We suggest that this degradation is due to incorporation of water molecules from the ambient atmosphere into the TIPS-pentacene, details of which will be discussed in a section later in this chapter.

5.1.2 Mechanisms of organic magnetoresistance (OMAR)

Organic magnetoresistance (OMAR) is defined as the change in resistance of an organic semiconductor device under an applied magnetic field without any spin injection from ferromagnetic electrodes. This effect can be observed at room temperature and with applied magnetic fields of several mT^{33,103}. The observed relative change in device current under applied magnetic field is termed as magnetoconductance (MC). The MC can be quantified as,

$$MC = \frac{I_B - I_0}{I_0}, \quad (5.1)$$

where I_0 is the current without an applied magnetic field and I_B is the current at an applied magnetic field of B . MC values can be both positive or negative¹⁰⁷. Sign changes of MC has also been observed as a function of temperature or applied bias. Several organic semiconductors consisting of small molecules such as Alq_3 ³³, pentacene¹⁰⁵, α -sexithiophene¹⁰⁸ or even conjugated polymers like poly(N-vinyl carbazole), poly (p-phenylene vinylene) (PPV)¹⁰⁸ derivatives have been found to exhibit OMAR effect as an intrinsic material property. It was confirmed that OMAR is originated from intrinsic material property, not from spin injection by measuring the same type of devices with different film thicknesses¹⁰² and thereby decreasing the possibility of spin injection. It was found that the MC increased approximately linearly with thickness, thus ruling out the possibility of originating from magnetic field dependent injection. It has also been shown that OMAR does not depend on the orientation of applied magnetic field with respect to the sample surface¹⁰². The magnitude of the MC can be increased by applying a relatively large current density for some time which is termed as conditioning. Niedermeier *et al.*¹⁰⁹ showed increase of MC from 1 to 15% for PPV based devices by applying 1.25×10^3 A.m⁻² for a duration of 1 h. This increase in MC is believed to result from the formation of traps¹¹⁰. However, the actual mechanism behind observed OMAR effect is still debated. Various models have been proposed to describe the observed effect⁹⁹. In the following section, some of these models will be discussed.

It is proposed that hyperfine fields, which is the interaction between a nucleus and its surrounding environment, is the main source of spin relaxation in organic materials¹¹¹. In organic compounds, hyperfine coupling is dominant due to presence of the hydrogen atoms. The spin of the π -electrons couples indirectly to these nuclear spins through the interaction with the s-electrons of hydrogen. A dipole–dipole coupling between the spin of the π -electron and the nucleus is also present. As the electron spin interacts with the neighbouring nuclei, the total effect can be described by a classical hyperfine field in the range of few mT. Once spin is injected into the organic layer, it precesses around the local hyperfine field. As this hyperfine field is random at every site, the precession will change in a random direction causing a loss of spin polarization. This loss can be compensated with an external magnetic field, resulting in a magnetic-field dependent spin diffusion length affecting the shape of observed MR curve¹¹².

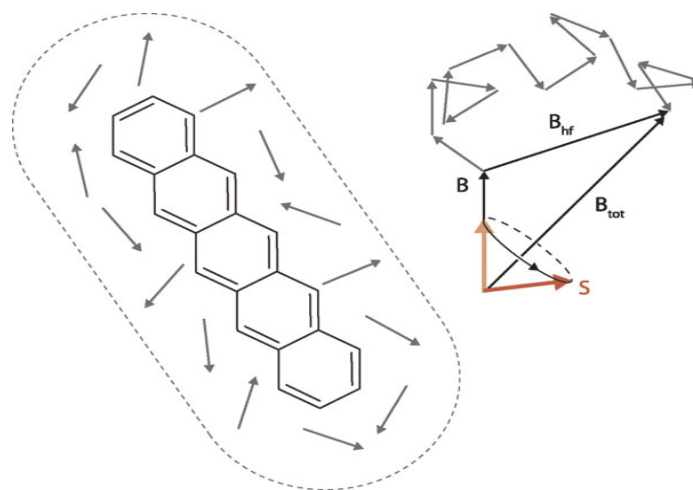


Figure 5.3 The spin of a polaron on a pentacene molecule interacting with the hyperfine fields from the hydrogen nuclei (illustrated by arrows). The polaron spin precesses around the sum of hyperfine fields from surrounding hydrogen nuclei and the external magnetic field. Figure taken from ref.⁹⁹.

Experiments by Nguyen *et al.* confirmed the role of hyperfine fields in obtaining OMAR. The authors used a PPV¹¹³ derivative and replaced all the relevant hydrogen with deuterium. Deuterium has less hyperfine constant by a factor of six and hence a larger spin-diffusion length was expected if hyperfine field is indeed the main cause of loss of spin polarization. When spin valves using the hydrogenated and deuterated polymer were compared, the deuterated ones showed a much larger MR and a spin-diffusion length. In another experiment, the most common isotope of carbon, carbon-60 (C₆₀) was used for determining the role of hyperfine coupling. As C₆₀ does not contain any

hydrogen atoms, the hyperfine coupling can be effectively eliminated in this semiconductor. Absence of any OMAR effect was reported for ITO/C₆₀/Ca/Al and Au/C₆₀/Ca/Al devices¹¹⁴. In the next step, hyperfine coupling was intentionally introduced by replacing C₆₀ with a substituted fullerene derivative (PCBM) exhibiting a hydrocarbon side-group. These devices showed clear OMAR signal.

Several models have been suggested for OMAR to explain the observed change in the current, electroluminescence, photocurrent or fluorescence under an applied magnetic field. In this section, some of the main models explaining the mechanism behind observed OMAR effect will be discussed. The models can be categorized based on the pairs of particles that is considered in the model for the spin-dependent interactions. These different particle pairs can be e–e pairs or h–h (where e and h denote electron and hole, respectively) pairs as considered in the bipolaron model, e–h pairs as considered in the e–h pair models, and excitons and free or trapped charges as considered in the triplet–charge interaction model. Figure 5.4 illustrates the particles considered in various models explaining OMAR mechanism. However, it should be noted that these spin-dependent interactions do not depend on the net spin polarization but on the relative orientation of the spins.

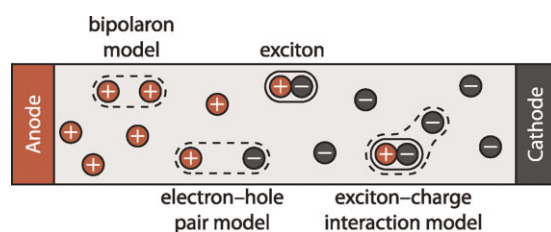


Figure 5.4 Illustration of the particle interactions that are considered in the different OMAR models. Figure taken from ref.⁹⁹.

It can be difficult to compare between various reports on OMAR as even with (almost) the same device structure and materials, different magnitudes of OMAR have been reported. In such devices, changing only one parameter (e.g. applied voltage, temperature or film thickness) might not give a very conclusive results on factors which determines the magnitude of OMAR effect. This can be explained as effects like conditioning and trapping play an important role on OMAR. Factors like fabrication process, material purity, ambient or even sequence of recording the experimental data can affect the results on OMAR.

(a) Bipolaron model

One of the main models explaining the mechanism behind observed OMAR effect is the bipolaron model^{99,115,116}. Due to energetic and positional disorder, charge transport occurs only via a limited number of percolation paths. On such a path, one carrier might be blocking the passage of another carrier. Depending on the spins of the two identical particles, a bipolaron can be formed as an intermediate state, which allows the carrier to pass afterwards. This is possible only when the spins of the two carriers are in a singlet configuration, as shown in figure 5.5(a). If the carriers are in triplet configuration, that leads to spin blocking as shown in figure 5.5(b). Even in absence of an external magnetic field, the carriers experience the hyperfine field.

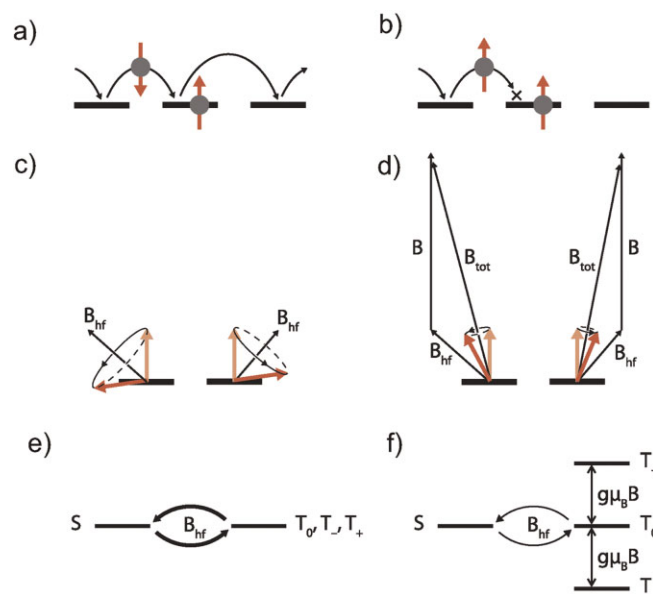


Figure 5.5 (a, b) Illustration of spin-blocking in bipolaron. Two particles with parallel spins cannot form an intermediate bipolaron. (c, d) Illustration of spin precession of two neighbouring spins in (c) only the local hyperfine fields B_{hf} and (d) in the total field B_{tot} , the sum of the local hyperfine field and the external field B . (e, f) Corresponding energy diagrams. (e) Without an external field, the hyperfine field mixes the singlet S and all three triplets, T_+, T_0 , and T_- . (f) An external field Zeeman splits the triplets. Mixing occurs only between S and T_0 . Figure taken from ref. ⁹⁹.

As showed in figure 5.3, the total hyperfine field one carrier experiences, is the sum of many random hyperfine fields. As a result, individual carriers experience individual total hyperfine field. The precession of spins in presence of a magnetic field changes the spin configuration of a pair of carriers because each of these carriers experience a different hyperfine field.

If we consider two spins initially in a triplet configuration as shown in figure 5.5(c), due to different precession of the spins, a singlet will mix in, creating a chance to form a

bipolaron, thus lifting the blocking. When a large external magnetic field is applied, the spins precess around the sum of this field and the local hyperfine field as shown in figure 5.5(d). As the hyperfine field is almost negligible, the spins eventually experience approximately the same amount of magnetic field resulting in two parallel spins remaining parallel with no intermixing. This can also be understood from the energy level diagrams of the total spin state of two carriers, as shown in figure 5.5(e,f). This involves one singlet (S) and three triplet (T) states. At zero external field [figure 5.5(e)], S and all three triplets are degenerate in energy and are mixed by the random hyperfine fields, allowing a large current to flow. However, when a large magnetic field is applied the triplets split in energy [figure 5.5(f)]. As a result, no mixing is possible between the singlet state S and the triplet states T⁺ and T⁻, as the Zeeman energy is larger than the hyperfine energy, resulting in a reduced current flow, and hence a positive magnetoresistance or a negative magnetoconductance. Thus a decrease in bipolaron formation by applying an external magnetic field can result in a decrease in device current. Though MC is usually negative, a positive sign can also be obtained when long range Coulomb repulsion is included. The long range Coulomb repulsion enhances the bipolaron formation. When more bipolarons are formed, there are less free carriers responsible for the current flow. The number of bipolarons can be reduced by applying an external magnetic field which gives rise to a positive magnetoconductance or a negative magnetoresistance.

(b) Electron-hole (e-h) pair model

The figure 5.6 shows different paths via which pairs of free polarons can recombine to the ground state⁹⁹. Free polarons are first bound as singlet and triplet e-h pairs, with a ratio 1:3, by coulombic force. These can convert into excitons (with rates k_S and k_T) or dissociate to free polarons (with rates q_S and q_T). Singlet and triplet e-h pairs can also be mixed by the hyperfine fields, resulting in an intersystem crossing with a rate m_{ISC} . The singlet and triplet excitons have different energies due to the exchange interaction. Recombination of free polarons reduces the current as this reduces the number of free carriers available for current flow. In the e-h pair model, the recombination and/or dissociation of e-h pairs are assumed to be different for singlet and triplets. Therefore, a change in the mixing of these pairs by an external magnetic field results in a change in the current. The way the magnetic field reduces the mixing by the hyperfine fields is similar to the reduction of mixing in the bipolaron model. The

total spin state of e–h pair is mixed in this model, instead of mixing the total spin state of two equally charged polarons (e–e or h–h). Prigodin *et al.* derived a magnetic field dependent recombination rate, linking it to the recombination mobility by balancing the recombination and dissociation rates^{117,118}. The authors assumed that singlets have a larger recombination rate than triplets ($k_S > k_T$) and the triplets mostly contribute to dissociation. Hence with less mixing in presence of an applied magnetic field, there is less recombination. This reduction gives rise to more current and thus a positive magnetoconductance or a negative magnetoresistance. The authors also tried to explain negative magnetoconductance by introducing a regime where the current responds oppositely to a change in recombination.

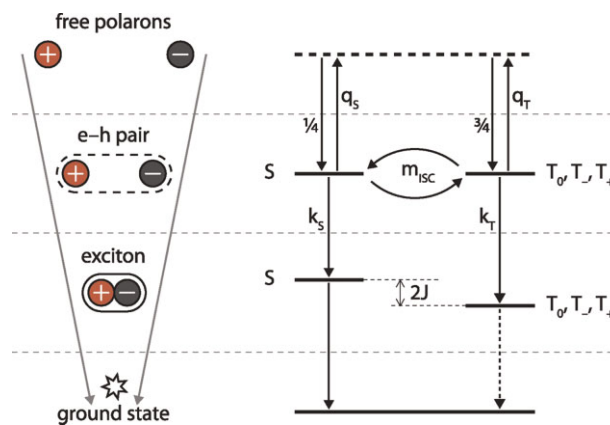


Figure 5. 6 Diagram of possible routes for recombination of free electrons and holes to the ground state, by first forming an e–h pair which turns into an exciton. The different transitions are explained in the text. Figure adapted from ref.⁹⁹.

(c) Exciton–charge interaction model

Desai *et al.* considered the excitons^{33,119} in the OMAR model instead of considering the e–h pairs. An exciton can transfer its energy to a charge carrier upon recombining to the ground state which is known as the exciton–charge interaction¹²⁰. Desai *et al.* also considered a reduction in the mobility of the free carriers by scattering on the exciton in an intermediate state of the exciton–charge interaction. It was suggested that a magnetic field plays a role on the intersystem crossing of singlet and triplet excitons, reducing the number of triplets in an applied magnetic field. This leads to reduced scattering of free charges on the triplets, thus a positive magnetoconductance or negative magnetoresistance. A negative magnetoconductance could also result from dissociation of the excitons into free carriers by the charge interaction. However,

it should be noted that the suggested magnetic-field dependence of the intersystem crossing between singlet and triplet excitons is highly improbable as the energy splitting is very large compared to the Zeeman splitting by a typical hyperfine field. Therefore, mixing of singlet and triplet excitons can be considered as not to be applicable. The exciton–charge interactions could play a role via another route. The reaction is spin dependent as the total spin is conserved in the reaction. Hence, application of a magnetic field reduces the average triplet–charge interaction rate by Zeeman-splitting the energies of the particles. The exciton–charge interaction can lead to de-trapping of the charges, thus increasing the current, resulting in a negative magnetoconductance. However, in the reaction the triplet exciton is lost, and hence it cannot contribute to the current via dissociation anymore, resulting in a positive magnetoconductance.

Other than exciton–charge interactions, exciton–exciton interactions can also be responsible for OMAR. Two triplets can interact to form a ground state singlet and an excited singlet, which quickly decays on emitting a photon, giving rise to delayed fluorescence. This triplet-triplet annihilation is a spin dependent phenomena and can be influenced by external magnetic field¹²¹.

5.2. OMAR measurements on TIPS-pentacene OFETs and HED-TIEs

5.2.1 Experimental details

The OFET substrates were purchased from Fraunhofer IPMS (Dresden, Germany) with channel lengths varying between 2.5 μm and 20 μm and a channel width of 10 mm. The gate oxide SiO_2 is 270 ± 10 nm thick and the source and drain electrodes are made of 30 nm Au with a 10 nm ITO adhesion layer. The gate electrode was kept at ground voltage for the magnetoresistance measurements and the devices were used as two terminal devices for making the results comparable with the HED-TIEs. For the HED-TIEs, the samples were prepared using the “spacer-approach” technology for fabricating HED-TIEs as discussed in chapter 2. A 130 nm of thermally grown SiO_2 layer was used as the isolation layer and 30 nm Au was deposited as the electrode layer with a 10 nm Cr as the adhesion layer. The TIPS-pentacene was drop-coated from solution following the procedure described in section 2.2.1.1. Because the TIPS-pentacene solution coats the gold surface (HED-TIEs) in much better way compared to the SiO_2 surface (OFETs) different amounts of solution, 5 μl and 3 μl , were used for OFET (chip area of 0.8 cm x 0.8 cm) and HED-TIEs (chip are of 1 cm x

1 cm), respectively, in order to ensure similar coverage. The electrical measurements were done as described in chapter 2, section 2.3 (a). The electrical characterisation including the photo-switching, current-voltage characteristics, and magnetoresistance measurements was performed immediately after the sample preparation. The total measurement time was about 1 h for each sample.

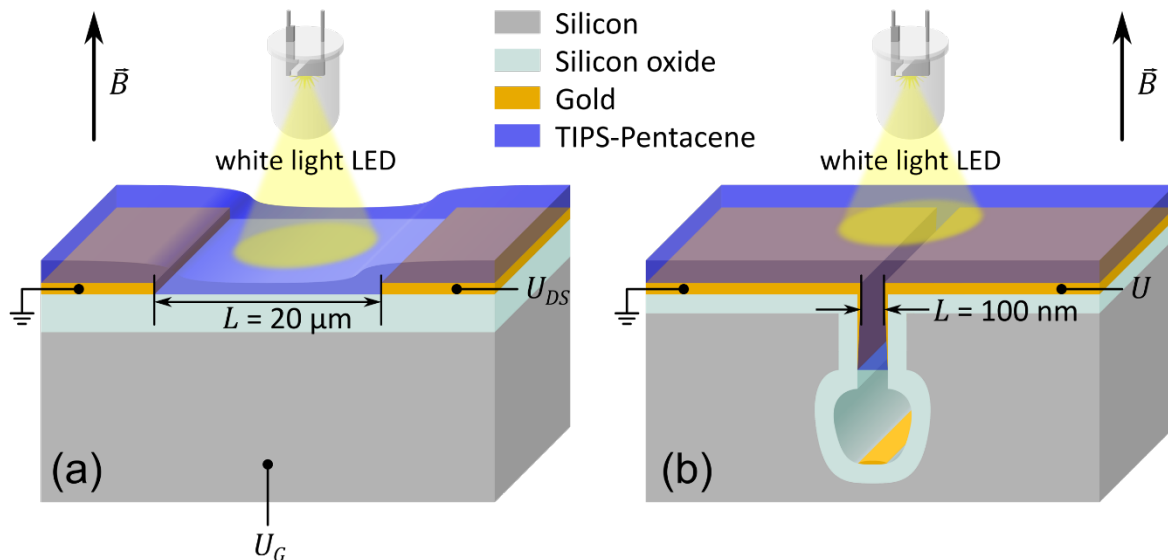


Figure 5.7 Schematic diagram of the experimental setup: (a) Commercial bottom contact OFET substrates (b) Planar device structure with trench isolated electrodes (HED-TIE). Figure taken from ref.⁸⁴.

The schematic diagram of the experimental set up is shown in figure 5.7. The entire sample surface was illuminated with a white light emitting diode (LED), with an emission ranging from 400 nm to 700 nm for the measurements of the photocurrent and of the magnetoresistance. The measurements were performed at room temperature ($\sim 25 \text{ }^\circ\text{C}$) and the ambient humidity was maintained at $\sim (20 \pm 5) \%$. The magnetic field was applied perpendicular to the electrical transport channel and to the substrate plane, using an electromagnet, though previous reports showed OMAR is independent of the sign and direction of the applied magnetic field¹⁰². It should be noted here that the experiments with OFETs have been carried out in a joint work and would partially be discussed in another dissertation¹²². The purpose of including the results with OFETs in this dissertation was just to demonstrate the improvement in the device performance in HED-TIEs compared to the standard planar hybrid devices, both fabricated using conventional photolithography.

5.3 Results and discussions

Figure 5.8(a) and figure 5.8(b) show the percentage of photocurrent with respect to the dark current, when the white light LED was switched on and off for OFET and HED-TIEs respectively. The percentage of the change in current was found to be more representative when comparing two device architectures with significantly different volume of the active organic channel. The photocurrent of the HED-TIEs is a factor of two higher and the photo-switching occurs to be faster in the HED-TIE devices, due to the smaller electrode gap.

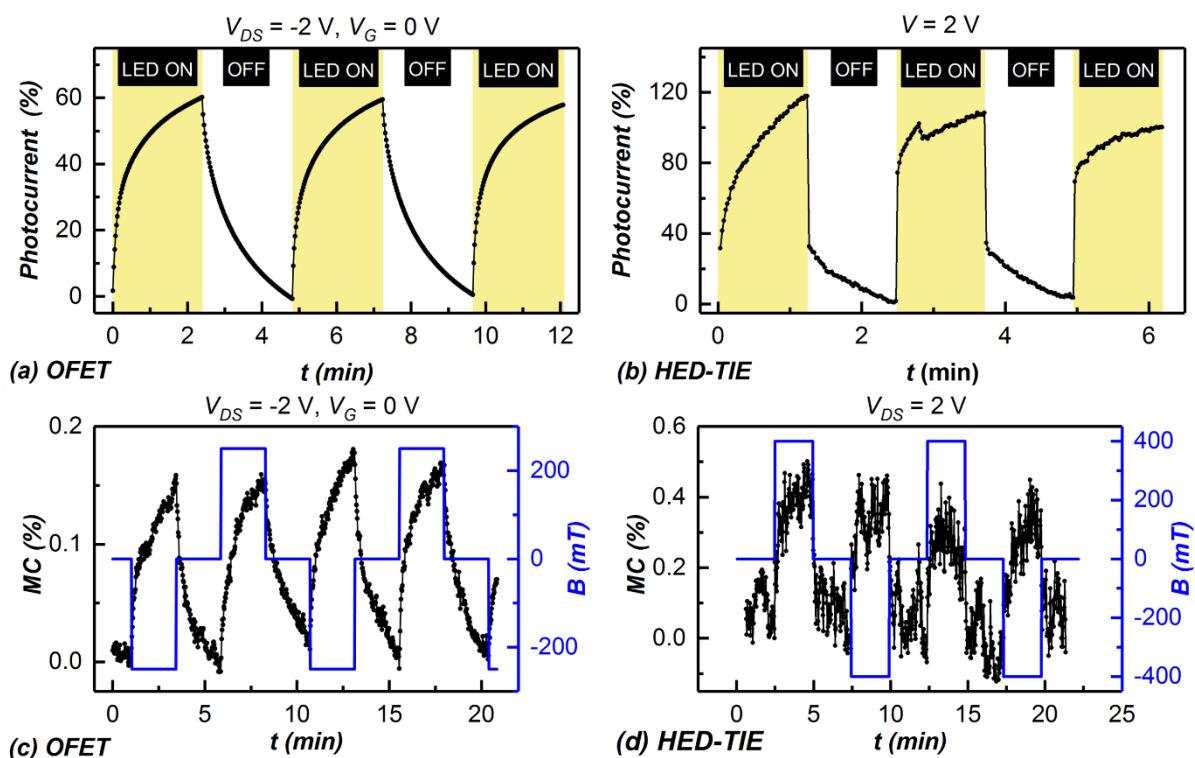


Figure 5.8 Light switching behaviour of TIPS-pentacene based (a) organic field effect transistor (OFET) and (b) hybrid electronic device with trench isolated electrodes (HED-TIE). Light induced magnetoresistance in TIPS-pentacene obtained from both types of planar devices: (c) OFET and (d) HED-TIE device. Figure taken from ref.⁸⁴.

Figure 5.8(c) and figure 5.8(d) show the magnetoconductance response of the same devices. Here, the device current over time was measured by switching on and off a constant applied magnetic field while the illumination was kept on throughout the measurements. Both OFETs and the HED-TIEs were found to exhibit positive magnetoconductance (negative magnetoresistance) as previously reported for evaporated TIPS-pentacene in ref.¹⁰⁶. The magnitude of OMAR is independent of the sign of the applied magnetic field which is expected for OMAR. For both light and

magnetic field switching, the HED-TIE devices were found to respond faster whereas the OFETs exhibit a slower carrier relaxation. This can be attributed to higher electric fields and shorter charge carrier transit times in the shorter channels of the HED-TIEs (~100 nm) compared to that of OFETs (20 μm). Also the magnitude of switching in HED-TIE for magnetic field was found to be twice as much as OFET, similar to the observed photocurrent.

It is worth mentioning that the TIPS-pentacene OFETs fabricated by thermal evaporation in ref.¹⁰⁶ showed a fast switching response, similar to the HED-TIEs, most probably due to the significantly less volume of the OFET channel (78 nm film thickness in ref.¹⁰⁶, compared to ca. 500 nm film thickness in the drop coated OFETs at the same channel length). The mobility values determined for our solution processed OFETs are in the range of 10^{-2} - $1 \text{ cm}^2 \text{ V}^{-1} \text{ s}^{-1}$, i.e. higher compared to the mobilities reported for the thermally evaporated TIPS-pentacene ($6 \cdot 10^{-3}$ - $1 \text{ cm}^2 \text{ V}^{-1} \text{ s}^{-1}$)¹⁰⁶.

No magnetoresistance was observed in the absence of illumination and hence of a photocurrent. It can be concluded that the observed effect in the solution-deposited TIPS-pentacene OFETs and HED-TIEs is supposed to be based on the presence of spin carrying polarons related to electrons and holes created by photoexcitation. As discussed in section 5.1.2 (b), these weakly interacting polarons are labelled as “electron-hole (e-h) pairs” and are considered to contribute to OMAR because of their flexible spin configuration (singlet or triplet). The same mechanism was proposed to be responsible for the OMAR observed in thermally evaporated TIPS-pentacene OFETs in ref.¹⁰⁶, which indicates that the processing methods of the TIPS-pentacene does not influence the intrinsic mechanism of the OMAR in this organic semiconducting material. In the e–h model, the recombination into electrically neutral excitons and the dissociation of the weakly bound e–h pairs into charge carriers available for the electrical transport is influenced by an applied magnetic field, in the favour of the latter effect (see ref.^{99,106} and references therein). An applied magnetic field will thus trigger an increase in the conductance of the device^{99,106}. It should be noted that although the applied constant magnetic field was different for the OFETs and HED-TIEs, this should not have an influence on the magnitude of the OMAR effect. It was shown in ref.¹⁰⁵ for pentacene that the magnitude of OMAR almost reaches a saturation at ~80 mT and a similar saturation field was also reported for other materials such as Alq_3 ¹⁰¹.

The observed magnetoresistive effect was found to diminish approximately after two days of sample preparation in case of the HED-TIEs kept under ambient conditions,

while the photocurrent decreased from 120 % to only 65 %. The photo-switching time, however, increased compared to the freshly prepared sample. The magnetoresistive effect and the photocurrent in the OFETs were also found to decrease in magnitude, but the magnetoresistance did not disappear completely in the same time interval considered for the HED-TIEs. This could be due to the TIPS-pentacene layer being thicker for the OFETs, which confers longer time stability in ambient. The degradation of the devices in ambient atmosphere can be attributed to the penetration of oxygen and/or water molecules in the TIPS-pentacene film, additionally accelerated by white light illumination. Vollmer *et al.* showed⁷⁷, by investigating the occupied electronic states using ultraviolet photoemission spectroscopy, that the diffusion of molecular oxygen and water from the ambient into pentacene layers is reversible when the air exposure takes place in the dark or under visible light. The exposure to ambient under UV illumination leads to a reaction, most probably with singlet oxygen and/or ozone⁷⁷. As the magnetoresistance measurements are performed in presence of white light with a spectrum ranging from 400 nm to 700 nm, it is believed that different parts of the wavelength spectra can have different contributions to the device degradation. It was also shown by Jurchescu *et al.*⁷² that pentacene single crystals behave differently when the electrical conductivity is measured in ambient or dry air, with and without illumination. As discussed in chapter 4, a decrease in photoluminescence was observed caused by the diffusion of oxygen/water in TIPS-pentacene films in the HED-TIEs which was reversible⁴⁰ and the recovery of the photoluminescence was found to be much faster under nitrogen purging and for a single wavelength illumination. Figure 5.9 illustrates the role of water molecules in the disappearance of observed magnetoresistance. To verify the role of water molecules diffusion into the TIPS-pentacene film in the deterioration of the magnetoresistance, an OFET was prepared by drop-coating a substrate with the same TIPS-pentacene solution as used for the preparation of the devices discussed before but now diluted (1:1) in deionized water. As shown in figure 5.9 (a), the magnitude of the photocurrent of the freshly prepared device was found to be only 6 % (compared to 60 % for the device prepared with non-diluted solution, shown in 5.8 (a) whereas the magnetoresistance disappeared completely in this case. The output characteristics of such a device showed a drastic change in the line shape compared to the TIPS-pentacene transistor prepared from water-free solution.

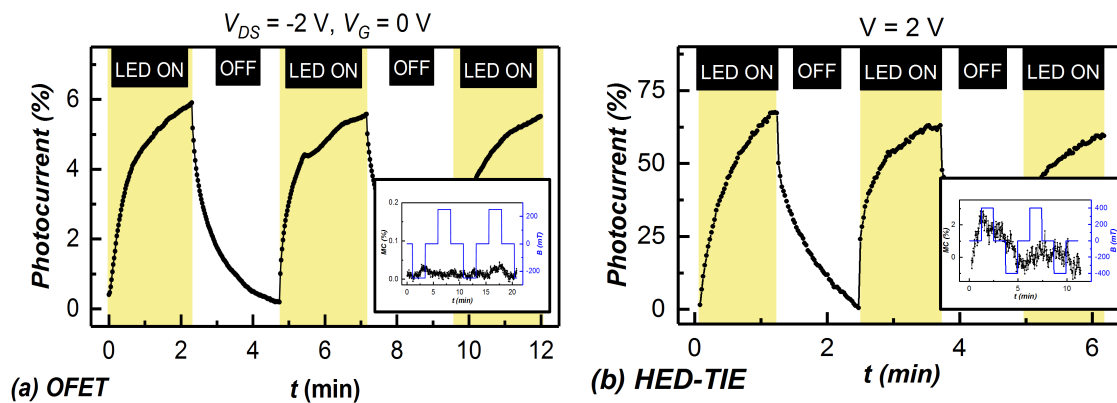


Figure 5.9 (a) Light switching of OFET prepared by drop-coating of TIPS-pentacene diluted in water. The inset shows absence of the magnetoresistance in such an OFET. (b) Degraded light switching behaviour of a TIPS-pentacene HED-TIE after two days of exposure to the ambient atmosphere. The inset shows the response to applied magnetic field. Figure taken from ref.⁸⁴.

Figure 5.10(a) shows the output characteristics of TIPS-pentacene OFET. P-type conduction behaviour is observed, as expected for TIPS-pentacene. On the other hand, when the OFET is prepared with TIPS-pentacene solution diluted in water, the OFET characteristics (shown in figure 5.10(b)) can be observed to degrade drastically. The current amplitude increases approximately four times in the OFETs prepared with TIPS-pentacene solution diluted in water.

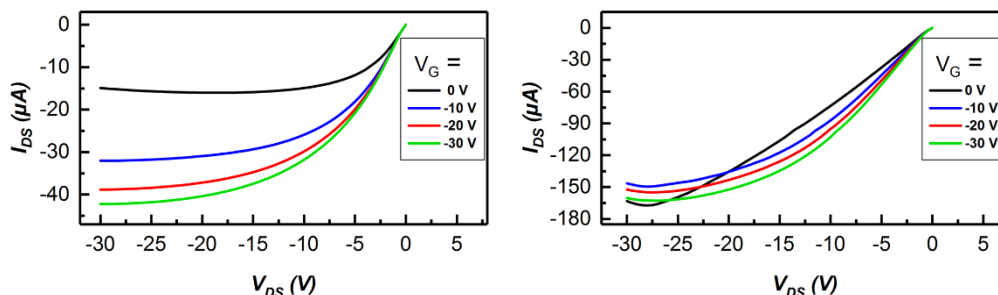


Figure 5.10 (a) Output characteristics of TIPS-pentacene OFET. (b) Output characteristics of an OFET prepared from same TIPS-pentacene solution, diluted in water (1:1). Figure taken from ref.⁸⁴.

The current-voltage characteristics of a HED-TIE is shown in figure 5. 11. The same device was measured freshly after sample preparation and after approximately two days of sample preparation (after OMAR disappeared) and compared. The current amplitude in HED-TIE was found to increase when it is exposed to ambient in similar scale as the OFETs with and without water in solution.

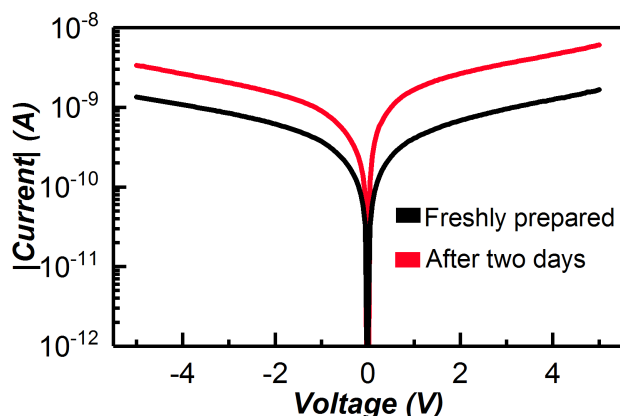


Figure 5.11 Output characteristics of the TIPS-pentacene based HED-TIE device, measured for freshly prepared sample and after two days of sample preparation. Figure taken from ref.⁸⁴.

This experiment shows that TIPS-pentacene exhibits a degradation in electrical properties upon water incorporation in the films. We assume that the water molecules in the film shift the energy level of the singlet and triplet states of the e-h pairs and thereby change the probability of intermixing between these two states. In the changed energy landscape of the excited electronic states, the effect of the magnetic field on the singlet/triplet intermixing could become negligible, resulting in the drastic reduction in magnetoresistance.

When two HED-TIEs with different channel dimensions were compared, the device with larger channel volume was found to exhibit better OMAR magnitude, faster switching, as well as slower degradation of the OMAR. Figure 5.12 shows the OMAR response of two different devices with channel width of 40 μm and channel lengths of 200 nm and 300 nm respectively. These two devices were fabricated using the “trench-refill approach” as described in chapter 2. The magnitude of the observed OMAR was much higher in this case; $\sim 6\%$ for the device with 200 nm channel length and $\sim 12\%$ for the device with 300 nm channel length. The reason behind obtaining higher OMAR in case of 300 nm channel length device might be related to the amount of material inside the trench. If the trench opening is larger, more amount of material will go inside the trench leading to more number of photo-generated carriers under illumination and hence a higher OMAR. As the overall volume of the organic channel material was much less in this case compared to the devices as shown in figure 5.8 (channel width of 40 μm instead of 500 μm), the OMAR in these devices were found to disappear within a day after sample preparation. This also supports the hypothesis for the faster degradation of OMAR in HED-TIEs compared to the OFETs. It should be noted that

only for the devices from this particular sample, positive magnetoresistance or negative magnetoconductance was observed. There are couple of possibilities which can explain this phenomenon: i) due to minor variation in the sample preparation, the crystalline structure of the TIPS-pentacene film might have been different which might have led to the sign change in OMAR, as reported earlier for Alq₃ films upon annealing¹²³, ii) as discussed earlier, in e-h pair model behind OMAR mechanism, the conduction might be in a regime where the current responds oppositely to a change in recombination⁹⁹ or iii) it can be a superposition of two different OMAR models, one dominating the other in particular case⁹⁹.

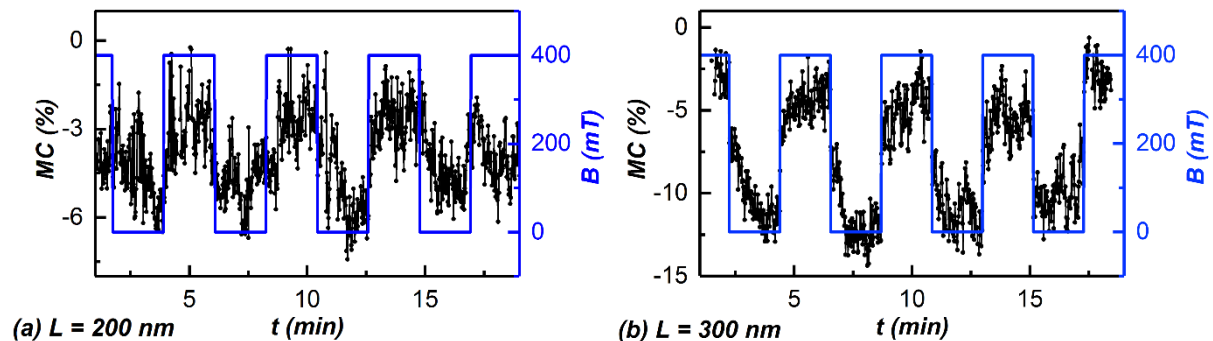


Figure 5.12 Comparison of OMAR magnitude in TIPS-pentacene based HED-TIE devices with two different channel lengths. The sample surface was illuminated with white light LED. Both devices have channel width of 40 μm and channel lengths of (a) 200 nm and (b) 300 nm.

The other model that could explain the sign change is the bipolaron model. This model is based on unipolar transport and electron and hole mobilities can be separately influenced by the applied magnetic field⁹⁹. The current is mostly unipolar and the majority carriers cause the OMAR. Above the transition voltage minority charge electron injection sets in and the minority charge carriers dominate the magnetoconductance. It is possible for the minority charges to dominate the magnetoconductance due to the compensation of space charge when the device becomes bipolar since the sum of the relative mobility changes in electrons and holes determines the sign of magnetoconductance. However, it needs further experiments and/or modelling to identify the actual reason behind the observed sign change in OMAR.

5.4 Summary and outlook

To summarize, light induced negative magnetoresistance was demonstrated in freshly prepared solution processed TIPS-pentacene planar devices of two different architectures, measured under ambient atmosphere. Organic magnetoresistance was demonstrated for the first time in solution processed devices and under ambient atmosphere. The HED-TIEs with smaller electrode gap yielded in twice as much photocurrent and magnetoresistance compared to commercial OFETs, and also showed faster switching response time. Although TIPS-pentacene is supposed to be air stable, the influence of ambient atmosphere was found to cause diminishing of the magnetoresistance and the photocurrent of the fabricated devices within a period of two days after sample preparation. The overall current amplitude of the device output current was found to increase by approximately a factor of 4. Previously it was observed that there is a decrease in photoluminescence caused by the diffusion of oxygen/water in TIPS-pentacene films in the HED-TIEs. This was found to be reversible and the photoluminescence could be recovered much faster under nitrogen purging and for single wavelength illumination⁴⁰. We assume the degradation in magnetoresistance and photocurrent of the TIPS-pentacene based devices is due to incorporation of water molecules in the TIPS-pentacene film when it is exposed to ambient. To support this hypothesis, an OFET with the very same TIPS-pentacene solution but diluted in deionized water was prepared and characterized. The absence of magnetoresistance in this OFET was shown along with a reduction, but not complete disappearance of the photocurrent of the device. It is suggested that usage of a suitable capping layer for protecting the organic layer could increase the lifetime of such devices, when used as magnetoresistive sensors working under ambient atmosphere.

As an outlook to further research work, different organic materials can be tried for obtaining OMAR from such a fabricated device. Ferromagnetic electrodes along with suitable channel materials can also be used instead of gold electrodes for obtaining magnetoresistance from spin injection from the electrodes to the channel material, not as intrinsic material property which is observed in OMAR. Devices as shown in ref.⁹⁵ could be fabricated using the HED-TIE technology by conventional UV-lithography, instead of the electron beam lithography used in this report. GMR devices could also be fabricated by using the shadowing technique as used in ref.⁴⁵ for deposition of two

different metals with distinct switching fields on two different electrodes. It is also possible to combine the light-sensing and magnetic-sensing properties of HED-TIEs, by using different illumination of different wavelength regime and studying the corresponding light-induced magnetoresistance when an external magnetic field is applied. For this purpose, it is extremely important to control the stability issue of the channel material under ambient atmosphere to make the results comparable with each other and thus more conclusive. It is also important to study the material degradation and the corresponding electrical conduction behaviour of the channel material in ambient and/or in dry air under different wavelength illumination as it was previously discussed that different wavelengths affect the material properties in different ways.

Chapter 6

Summary and outlook

In this dissertation, a new fabrication technology was proposed for fabrication of planar hybrid electronic devices with trench isolated electrodes (**HED-TIE**). The technology used conventional photolithography (365 nm) and was demonstrated to be capable of fabricating electrode gap dimensions in the range of ~100 nm.

For fabrication of patterns in the range of ~100 nm, usually electron beam lithography is used which is an expensive and time consuming technique. This makes it unsuitable for wafer-scale production for industrial applications. The other alternatives which are used in general are nano-stencil lithography or nanoimprint lithography. Both of these techniques can indeed be applicable on wafer level but the fabrication of stencil or the stamp itself uses expensive techniques like electron beam lithography or ion beam lithography through a very complex process flow. Thus the proposed HED-TIE technology can have lot of potential in cost-effective and wafer level fabrication of planar hybrid devices using conventional photolithography and other standard techniques used for silicon microtechnology. It can be scaled up for high volume manufacturing on 200 mm or 300 mm wafers. The technology is a one-mask process and offers lot of flexibilities in tuning the device architecture, device dimensions, the electrode or channel materials used, depending on the application of the HED-TIEs. The HED-TIE technology is compatible with various deposition techniques of the active transport channel, such as solution processing techniques (inkjet printing, spin-coating, drop-coating, or the 'doctor blade' method), stamping or vacuum deposition by thermal evaporation. The channel material option is not restricted to organic channels. Other materials such as polymers, oxides, or even 2D materials (graphene, MoS₂, WSe₂ etc.) can be implemented in the highly flexible fabrication process flow. The HED-TIE technology offers full accessibility of the active transport channel to external stimuli such as light or gases. This type of device structures can find a wide range of applications in spintronic devices, waveguides, photodetectors, or gas sensors, depending on the channel material and/or combination with the electrode material used for fabricating the devices.

The fabrication technology of the HED-TIEs was demonstrated using two different fabrication approaches: (a) trench refill approach and (b) spacer approach. Firstly, sub-

micron trenches with dimensions in the range of 850 nm to 1050 nm were patterned on silicon substrates. In the trench refill approach, a thick layer of LPCVD SiO_x layer was deposited to partially refill the trenches and thus achieving the desired electrode gap dimensions in the range of ~100 nm to 300 nm. This LPCVD SiO_x layer was also used as the isolation layer between the electrodes. Deposition of such a thick (~800 nm) LPCVD SiO_x on structures with different aspect ratios led to process parameter variations. The thickness of the LPCVD layer on the electrode areas was found to be higher than the trench area resulting in cone shaped trench openings. Therefore, it was necessary to modify the technology to have a better control on the process parameter variations and the trench geometry. Spacer approach was then proposed for overcoming the issues with process parameter variations and was successfully demonstrated for obtaining better control over the fabricated trench geometry. In spacer approach, an additional APCVD SiO_x layer was introduced in the process flow to alter the hard mask geometry even before the deep reactive etching of Si was carried out for fabricating the trenches. Introduction of the spacer layer in the fabrication process flow, reduced the thickness of the isolation layer from ~800 nm to ~130 nm. Both thermally grown oxide and APCVD oxides were tried out as the isolation layer as both were found to be suitable for producing the desired trench geometry. Finally, thermally grown oxide was chosen over APCVD oxide because of its better isolation properties and better electrical response of the fabricated devices. The electrical isolation of the fabricated structures was tested prior to the deposition of the organic materials to ensure that the measured device current is obtained indeed from the channel material and not from any contribution from leakage currents. Typically, > 97% of fabricated devices were found to have proper isolation between the electrodes.

To demonstrate the compatibility of the HED-TIE technology with both thermally evaporated and solution processed organic channel materials, thermally evaporated metal free phthalocyanine (H₂Pc) HED-TIEs and solution processed 6,13-bis(triisopropylsilylethynyl) pentacene or commonly known as TIPS-pentacene based HED-TIEs were fabricated and characterized. The thermally evaporated H₂Pc formed a “free-standing” membrane between the electrodes whereas the TIPS-pentacene solution went deep inside the trench and thus forming the transport channel between the electrodes. The basic electrical properties of fabricated HED-TIEs were discussed for devices with both solution-processed and evaporated channel materials. The device currents were found to increase with decreasing the electrode gaps of the

devices. The $\log(J)$ vs $\log(V)$ plots exhibited slope >2 indicating a trap dominated SCLC behaviour (where J is the current density and V is the applied voltage). The J vs $1/L^3$ plot followed the estimated linear behaviour for the thermally evaporated channel devices whereas an inconsistency was observed for solution processed devices with larger channel lengths. This difference between the solution processed and thermally evaporated channels was attributed to degree of filling of the trenches with the channel material. In case of solution processing, the amount of solution going inside the trench for devices with different channel length can vary, influencing the active channel area and hence the device current density. The device currents were found to increase drastically when the effective channel volume of the devices were increased by introducing interdigitated electrodes and thus by increasing the channel width from 50 μm up to 5000 μm .

TIPS-pentacene being a well-known photosensitive material, TIPS-pentacene based HED-TIEs were first demonstrated to have possible application as hybrid photodetectors. Photosensing properties of fabricated HED-TIEs were systematically studied with HED-TIEs of two different channel lengths and under different illuminations of different wavelength regime. To investigate the photosensing properties, three laser lines: 632.8 nm (1.96 eV, red), 514.7 nm (2.41 eV, green), and 325 nm (3.81 eV, ultraviolet) were used for illumination of the active area of the devices from the top. The HED-TIEs were found to generate photocurrents under all illumination wavelengths but the switching time constant and the switching line-shape varied depending on the illumination wavelengths. The HED-TIEs were found to be suitable to be used as hybrid photodetectors working in red wavelength regime. The TIPS-pentacene was found to be photo-oxidized in air. The effect was more prominent under UV-illumination. Photoluminescence studies showed this effect to be reversible when purged with nitrogen.

To tune the photosensing properties of the fabricated devices further, gold nanoparticles were added in the TIPS-pentacene matrix and photosensing properties were investigated using 632.8 nm (1.96 eV, red) and 514.7 nm (2.41 eV, green) laser lines. The photosensing properties were found to be tuned depending on the size of the nanoparticles in TIPS-pentacene matrix. However, the nanoparticles in TIPS-pentacene matrix were not stable after two months and the photo-switching properties were found to degrade drastically. The nanoparticle dispersion in ethanol itself

degraded within a year. The stability of the synthesised nanoparticles needs to be improved to fabricate HED-TIEs with tuneable photosensing properties.

TIPS-pentacene based HED-TIEs were also demonstrated to be possible to use as magnetoresistive sensors. For the first time, light induced organic magnetoresistance was obtained in solution processed planar hybrid devices, measured under ambient air and at room temperature. Two types of device architectures were used for this purpose: (a) commercial OFETs and (b) HED-TIEs fabricated in this work. The device channel area was illuminated using a white light LED. The photo-switching properties and the magnetoresistance of the devices were thoroughly investigated and the device performance of commercial OFETs and HED-TIEs were compared. For both light and magnetic field switching, the HED-TIE devices were found to respond faster whereas the OFETs exhibited a slower carrier relaxation. This was attributed to higher electric fields and shorter charge carrier transit times in the shorter channels of the HED-TIEs (~ 100 nm) compared to that of OFETs ($20 \mu\text{m}$). Moreover, the magnitude of switching in HED-TIE devices for both light and magnetic field was found to be twice as much as OFETs. The observed magnetoresistance was attributed to the presence of electron-hole pairs under illumination as the magnetoresistive effect was found to be scaled with the photocurrent. However, the observed magnetoresistance was found to disappear after two days of sample preparation in the HED-TIEs. The magnitude of photocurrent was also found to reduce by $\sim 50\%$ after two days. In the OFETs, the magnetoresistance did not disappear completely but the magnitude of the magnetic field switching was drastically degraded along with degradation in the photocurrent magnitude. This degradation in the device performance was attributed to incorporation of water moles in the TIPS-pentacene film under ambient atmosphere. This hypothesis was further proved by fabricating an OFET with the same TIPS-pentacene solution but diluted in water. This showed absence of magnetoresistance and a reduced magnitude of photocurrent. Protecting the active area of the devices with a suitable capping layer can make these solution-processed devices suitable for being used as magnetic sensors working in ambient atmosphere.

In future, HED-TIE devices can be fabricated using different channel materials like polyoxymethylene (POM), 2D materials or other organic materials and different application areas can be explored. Initial trial on direct stamping of 2D materials on the channel area of HED-TIEs led to reproducibility issues. The stamped flakes were not found to have proper wetting with the gold electrodes and thus resulted in inconsistent

electrical response. The experiments for using 2D flakes as the channel material were carried out in collaboration with the group of Prof. Eugenio Coronado in Valencia. As the HED-TIEs were demonstrated to exhibit OMAR, in the next step, spintronic devices involving spin injection from ferromagnetic electrodes can be fabricated. A possibility of fabricating GMR devices based on HED-TIEs can also be explored by combining the HED-TIE technology and the shadowing technique used in ref.⁴⁵ for deposition of two different metal layers on electrodes of planar devices. Last but not the least, the HED-TIE technology can be implemented on wafer-scale by using techniques like inkjet-printing or spin-coating for the deposition of organic channel materials.

References

- (1) Dediu, V. A.; Hueso, L. E.; Bergenti, I.; Taliani, C. Spin Routes in Organic Semiconductors. *Nat. Mater.* **2009**, *8*, 707–716.
- (2) Villanueva, L. G.; Vazquez-Mena, O.; Martin-Olmos, C.; Savu, V.; Sidler, K.; Brugger, J. Resistless Fabrication of Nanoimprint Lithography (NIL) Stamps Using Nano-Stencil Lithography. *Micromachines* **2013**, *4*, 370–377.
- (3) Yun, H.; Kim, S.; Kim, H.; Lee, J.; McAllister, K.; Kim, J.; Pyo, S.; Sung Kim, J.; Campbell, E. E. B.; Hyoung Lee, W.; Stencil Nano Lithography Based on a Nanoscale Polymer Shadow Mask: Towards Organic Nanoelectronics. *Sci. Rep.* **2015**, *5*, 10220.
- (4) Cao, Y.; Cai, K.; Hu, P.; Zhao, L.; Yan, T.; Luo, W.; Zhang, X.; Wu, X.; Wang, K.; Zheng, H. Strong Enhancement of Photoresponsivity with Shrinking the Electrodes Spacing in Few Layer GaSe Photodetectors. *Sci. Rep.* **2015**, *5*, 8130.
- (5) Murtaza, G.; Ahmad, I.; Chen, H.; Wu, J. Study of 6,13-Bis(tri-Isopropylsilylethynyl) Pentacene (TIPS-Pentacene Crystal) Based Organic Field Effect Transistors (OFETs). *Synth. Met.* **2014**, *194*, 146–152.
- (6) Feng, L.; Tang, W.; Zhao, J.; Yang, R.; Hu, W.; Li, Q.; Wang, R.; Guo, X. Unencapsulated Air-Stable Organic Field Effect Transistor by All Solution Processes for Low Power Vapor Sensing. *Sci. Rep.* **2016**, *6*, 20671.
- (7) Gunduz, B.; Yakuphanoglu, F. Effects of UV and White Light Illuminations on Photosensing Properties of the 6,13-Bis(triisopropylsilylethynyl)pentacene Thin Film Transistor. *Sensors Actuators A Phys.* **2012**, *178*, 141–153.
- (8) Clemens, J. T. *Bell Labs Technical Journal*. Silicon Microelectronics Technology. **1997**, 76–102.
- (9) Zirngibl, M.; Bischoff, J. C.; Theron, D.; Ilegems, M. A Superlattice GaAs / InGaAs-on-GaAs Photodetector for 1.3 μm Applications. *IEEE Electron Device Letters*, *10*, **1989**, 336–338.
- (10) Müller, J. E.; Grave, T.; Siweris, H. J.; Kärner, M.; Schäfer, A.; Tischer, H.; Riechert, H.; Schleicher, L.; Verweyen, L.; Bangert, A.; Kellner, W.; Meier, T. A GaAs HEMT MMIC Chip Set for Automotive Radar Systems Fabricated by Optical Stepper Lithography. *IEEE Journal of Solid State Circuits*, **1997**, *32*, 1342–1349.

- (11) Eaton, W. P.; Smith, J. H. Micromachined Pressure Sensors : Review and Recent Developments, *Smart Mater. Struct.*, **6**, **1997**, 530-539
- (12) Eley, D. D. Phthalocyanine as Semiconductors. *Nature* **162**, **1948**, 819.
- (13) Helfrich, W.; Schneider, W. G. Recombination Radiation in Anthracene Crystals. *Phys. Rev. Lett.* **1965**, **14**, 229–232.
- (14) Pope, M.; Kallmann, H. P.; Magnante, P. Electroluminescence in Organic Crystals. *J. Chem. Phys.* **1963**, **38**, 2042.
- (15) Yang, Y.; Wudl, F. Organic Electronics: From Materials to Devices. *Adv. Mater.* **2009**, **21**, 1401–1403.
- (16) Ratner, M. A Brief History of Molecular Electronics. *Nat. Nanotechnol.* **2013**, **8**, 378–381.
- (17) Madec, M. B.; Crouch, D.; Llorente, G. R.; Whittle, T. J.; Geoghegan, M.; Yeates, S. G. Organic Field Effect Transistors from Ambient Solution Processed Low Molar Mass Semiconductor–insulator Blends. *J. Mater. Chem.* **2008**, **18**, 3230.
- (18) Dierckx, W.; Oosterbaan, W. D.; Bolsée, J.C.; Cardinaletti, I.; Maes, W.; Boyen, H.G.; D’Haen, J.; Nesladek, M.; Manca, J. Organic Phototransistors Using poly(3-Hexylthiophene) Nanofibres. *Nanotechnology* **2015**, **26**, 65201.
- (19) Schumann, S.; Hatton, R. A.; Jones, T. S. Organic Photovoltaic Devices Based on Water-Soluble Copper Phthalocyanine. *J. Phys. Chem. C* **2011**, **115**, 4916–4921.
- (20) Clark, M. D.; Jespersen, M. L.; Patel, R. J.; Leever, B. J. Ultra-Thin Alumina Layer Encapsulation of Bulk Heterojunction Organic Photovoltaics for Enhanced Device Lifetime. *Org. Electronics*, **2014**, **15**, 1–8.
- (21) Kim, S.J.; Lee, J.S. Flexible Organic Transistor Memory Devices. *Nano Lett.* **2010**, **10**, 2884–2890.
- (22) Scott, J. C.; Bozano, L. D. Nonvolatile Memory Elements Based on Organic Materials. *Adv. Mater.* **2007**, **19**, 1452–1463.
- (23) Yu, X.; Zhou, N.; Lin, H.; Buchholz, D. B.; Yu, J.; Chang, R. P. H.; Marks, T. J.; Facchetti, Flexible Spray-Coated TIPS-Pentacene Organic Thin-Film Transistors as Ammonia Gas Sensors. *J. Mater. Chem. C* **2013**, **1**, 6532–6535.
- (24) Xue, J.; Forrest, S. R. Carrier Transport in Multilayer Organic Photodetectors: I. Effects of Layer Structure on Dark Current and Photoresponse. *J. Appl. Phys.* **2004**, **95**, 1869–1877.

- (25) Stoppa, M.; Chiolerio, A. Wearable Electronics and Smart Textiles: A Critical Review. *Sensors*, **2014**, 11957–11992.
- (26) Zeng, W.; Shu, L.; Li, Q.; Chen, S.; Wang, F.; Tao, X. M. Fiber-Based Wearable Electronics: A Review of Materials, Fabrication, Devices, and Applications. *Adv. Mater.* **2014**, 26, 5310–5336.
- (27) Weber, J.; Potje-Kamloth, K.; Haase, F.; Detemple, P.; Völklein, F.; Doll, T. Coin-Size Coiled-up Polymer Foil Thermoelectric Power Generator for Wearable Electronics. *Sensors Actuators, A Phys.* **2006**, 132, 325–330.
- (28) Bansal, A. K.; Hou, S.; Kulyk, O.; Bowman, E. M.; Samuel, I. D. W. Wearable Organic Optoelectronic Sensors for Medicine. *Adv. Mater.* **2015**, 27, 7638–7644.
- (29) Nishioka, M.; Lee, Y. B.; Goldman, A. M.; Xia, Y.; Frisbie, C. D. Negative Magnetoresistance of Organic Field Effect Transistors. *Appl. Phys. Lett.* **2007**, 91, 92117.
- (30) Maliakal, A.; Raghavachari, K.; Katz, H.; Chandross, E.; Siegrist, T. Photochemical Stability of Pentacene and a Substituted Pentacene in Solution and in Thin Films. *Chem. Mater.* **2004**, 16, 4980–4986.
- (31) Galbiati, M. Molecular Spintronics: From Organic Semiconductors to Self Assembled Monolayers. *Springer Thesis* **2016**.
- (32) Yang, C. Y.; Cheng, S. S.; Ou, T. M.; Wu, M. C.; Wu, C. H.; Chao, C. H.; Lin, S. Y.; Chan, Y. J. Pentacene-Based Planar and Vertical-Type Organic thin Film Transistor. *IEEE Trans. Electron Devices* **2007**, 54, 1633–1636.
- (33) Desai, P.; Shakya, P.; Kreouzis, T.; Gillin, W. P.; Morley, N. A.; Gibbs, M. R. J. Magnetoresistance and Efficiency Measurements of Alq₃-Based OLEDs. *Phys. Rev. B* **2007**, 75, 94423.
- (34) Jin, S. H.; Jung, K. D.; Shin, H.; Park, B.-G.; Lee, J. D. Grain Size Effects on Contact Resistance of Top-Contact Pentacene TFTs. *Synth. Met.* **2006**, 156, 196–201.
- (35) Majumdar, S.; Majumdar, H. S.; Laiho, R.; Österbacka, R. Comparing Small Molecules and Polymer for Future Organic Spin-Valves. *J. Alloys Compd.* **2006**, 423, 169–171.
- (36) Haick, H.; Cahen, D. Contacting Organic Molecules by Soft Methods: Towards Molecule-Based Electronic Devices. *Acc. Chem. Res.* **2008**, 41, 359–366.
- (37) Cesar, C.; Bufon, B.; Diego, J.; Espinoza, A.; Thurmer, D. J.; Bauer, M.;

- Deneke, C.; Zschieschang, U.; Klauk, H.; Schmidt, O. G. Strained Nanomembranes. *Nano* **2011**, *11*, 3727–3733.
- (38) Knopfmacher, O.; Hammock, M. L.; Appleton, A. L.; Schwartz, G.; Mei, J.; Lei, T.; Pei, J.; Bao, Z. Highly Stable Organic Polymer Field-Effect Transistor Sensor for Selective Detection in the Marine Environment. *Nat. Commun.* **2014**, *5*, 2954.
- (39) Zhang, C.; Chen, P.; Hu, W. Organic Field-Effect Transistor-Based Gas Sensors. *Chem. Soc. Rev.* **2015**, *44*, 2087–2107.
- (40) Banerjee, S.; Büلز, D.; Solonenko, D.; Reuter, D.; Deibel, C.; Hiller, K.; Zahn, D.; Salvan, G. HED-TIE: A Wafer Scale Approach for Fabricating Hybrid Electronic Devices with Trench Isolated Electrodes. *Nanotechnology* **2017**, *28*, 195303 (9pp).
- (41) Maximov, I.; Sarwe, E. L.; Beck, M.; Deppert, K.; Graczyk, M.; Magnusson, M. H.; Montelius, L. Fabrication of Si-Based Nanoimprint Stamps with Sub-20 Nm Features. *Microelectron. Eng.* **2002**, *61–62*, 449–454.
- (42) Ansari, K.; Van Kan, J. A.; Bettiol, A. A.; Watt, F. Fabrication of High Aspect Ratio 100 Nm Metallic Stamps for Nanoimprint Lithography Using Proton Beam Writing. *Appl. Phys. Lett.* **2004**, *85*, 476–478.
- (43) Taniguchi, J.; Koga, K.; Kogo, Y.; Miyamoto, I. Rapid and Three-Dimensional Nanoimprint Template Fabrication Technology Using Focused Ion Beam Lithography. *Microelectron. Eng.* **2006**, *83*, 940–943.
- (44) Min, S. Y.; Kim, T. S.; Kim, B. J.; Cho, H.; Noh, Y. Y.; Yang, H.; Cho, J. H.; Lee, T. W. Large-Scale Organic Nanowire Lithography and Electronics. *Nat. Commun.* **2013**, *4*, 1773.
- (45) Grünewald, M.; Kleinlein, J.; Syrowatka, F.; Würthner, F.; Molenkamp, L. W.; Schmidt, G. Large Room-Temperature Magnetoresistance in Lateral Organic Spin Valves Fabricated by in Situ Shadow Evaporation. *Org. Electron.* **2013**, *14*, 2082–2086.
- (46) Reuter, D.; Bertz, A.; Billep, D.; Scheibner, D.; Dötzel, W.; Gessner, T. In-Process Gap Reduction of Capacitive Transducers. *Sensors Actuators A.* **2006**, *126*, 211–217.
- (47) Shaw, K. A.; Zhang, Z. L.; MacDonald, N. C. SCREAM-I: A Single Mask, Single Crystal Silicon, Reactive Etching Process for Microelectromechanical Structures. *Sens. Actuators A* **1994**, *40*, 63–70.

- (48) Banerjee, S. Laterally Stacked Organic Trench Devices for Magnetoresistive Sensors, *Chemnitz University of Technology*, **2014**.
- (49) Marty, F.; Rousseau, L.; Saadany, B.; Mercier, B.; Français, O.; Mita, Y.; Bourouina, T. Advanced Etching of Silicon Based on Deep Reactive Ion Etching for Silicon High Aspect Ratio Microstructures and Three-Dimensional Micro- and Nanostructures. *Microelectronics J.* **2005**, *36*, 673–677.
- (50) El-Nahass, M. M.; Farid, A. M.; Attia, A. A.; Ali, H. A. M. Electrical Transport Properties of Thermally Evaporated Phthalocyanine (H_2Pc) Thin Films. *Egypt. J. Solids*, **2005**, 217–230.
- (51) Azim-Araghi, M. E.; Baedi, J.; Goodarzi, L. M. Electrical and Optical Properties of an Organic Semiconductor Metal-Free Phthalocyanine ($C_{32}H_{18}N_8$). *European Phys. J. Appl. Phys.* **2012**, *58*, 30201.
- (52) Gao, F.; Feng, X.; Yang, L.; Chen, X. New Sandwich-Type Lanthanide Complexes Based on Closed-Macrocyclic Schiff Base and Phthalocyanine Molecules. *Dalton Trans.*, **2016**, 45,7476–7482.
- (53) Park, Y. S.; Chung, S.; Kim, S. J.; Lyu, S. H.; Jang, J. W.; Kwon, S. K.; Hong, Y.; Lee, J. S. High-Performance Organic Charge Trap Flash Memory Devices Based on Ink-Jet Printed 6,13-Bis(triisopropylsilylethynyl) Pentacene Transistors. *Appl. Phys. Lett.* **2010**, *96*, 213107.
- (54) Davis, R. J.; Lloyd, M. T.; Ferreira, S. R.; Bruzek, M. J.; Watkins, S. E.; Lindell, L.; Sehati, P.; Fahlman, M.; Anthony, J. E.; Hsu, J. W. P. Determination of Energy Level Alignment at Interfaces of Hybrid and Organic Solar Cells under Ambient Environment. *J. Mater. Chem.* **2011**, *21*, 1721.
- (55) Hakeem, A.; Murtaza, G.. Structural, Optical, Electrochemical, Thermal and Elctrical Properties of 6 , 13-bIS (triisopropylsilylethynyl). *Digest Journal of Nanomaterials and Biostructures*, **2017**, *12*, 349–360.
- (56) Schroder, D. K. *Semiconductor Material and Device Characterization 2nd Ed.*; 1998.
- (57) Rose, A. Space-Charge-Limited Currents in Solids. *Phys. Rev.* **1955**, *97*, 1538–1544.
- (58) Wright, G. T. Mechanisms of Space-Charge-Limited Current in Solids. *Solid. State. Electron.* **1961**, *2*, 165–189.
- (59) Mark, P.; Helfrich, W. Space-Charge-Limited Currents in Organic Crystals. *J. Appl. Phys.* **1962**, *33*, 205-215.

- (60) Senthilarasu, S.; Sathyamoorthy, R.; Lalitha, S.; Subbarayan, A. Space Charge Limited Current Conduction in ZincPhthalocyanine (ZnPc) Thin Films. *Solid. State. Electron.* **2005**, *49*, 813–817.
- (61) Park, J. G.; Vasic, R.; Brooks, J. S.; Anthony, J. E. Characterization of Functionalized Pentacene Field-Effect Transistors and Its Logic Gate Application. *J. Appl. Phys.* **2006**, *100*, 44511.
- (62) Dacuña, J.; Salleo, A. Modeling Space-Charge-Limited Currents in Organic Semiconductors: Extracting Trap Density and Mobility. *Phys. Rev. B* **2011**, *84*, 195209.
- (63) Ma, X. Q. and J. C. and D. Trap-Free Space-Charge-Limited Electron Transport in Amorphous tin(IV) Phthalocyanine Dichloride Thin Film. *J. Phys. D. Appl. Phys.* **2010**, *43*, 215402 (5pp).
- (64) Agrawal, R.; Kumar, P.; Ghosh, S.; Mahapatro, A. K. Thickness Dependence of Space Charge Limited Current and Injection Limited Current in Organic Molecular Semiconductors. *Appl. Phys. Lett.* **2008**, *93*, 73311.
- (65) Ostroverkhova, O.; Platt, A. D.; Shepherd, W. E. B.; Day, J.; Anthony, J. E. Optical and Electronic Properties of Functionalized Pentacene and Anthradithiophene Derivatives. *Proceedings SPIE* **2009**, *7413*, 74130A.
- (66) Liu, N.; Tian, H.; Schwartz, G.; Tok, J. B. H.; Ren, T. L.; Bao, Z. Large-Area, Transparent, and Flexible Infrared Photodetector Fabricated Using P-N Junctions Formed by N-Doping Chemical Vapor Deposition Grown Graphene. *Nano Lett.* **2014**, *14*, 3702–3708.
- (67) Lopez-Sanchez, O.; Lembke, D.; Kayci, M.; Radenovic, A.; Kis, A. Ultrasensitive Photodetectors Based on Monolayer MoS₂. *Nat. Nanotechnol.* **2013**, *8*, 497–501.
- (68) Chen, C.; Qiao, H.; Lin, S.; Luk, C. M.; Liu, Y.; Xu, Z.; Song, J.; Xue, Y.; Li, D.; Yuan, J.; Yu, W.; Pan, C.; Lau, S. P.; Bao, Q. Highly Responsive MoS₂ Photodetectors Enhanced by Graphene Quantum Dots. *Sci. Rep.* **2015**, *5*, 11830.
- (69) Arisi, E.; Bergenti, I.; Dediu, V.; Loi, M. A.; Muccini, M.; Murgia, M.; Ruani, G.; Taliani, C.; Zamboni, R. Organic Light Emitting Diodes with Spin Polarized Electrodes. *J. Appl. Phys.* **2003**, *93*, 7682–7683.
- (70) Gupta, R. K.; Aydin, M. E.; Yakuphanoglu, F. Photoconducting and Electrical Properties of Al/TIPS-Pentacene/p-Si/Al Hybrid Diode for Optical Sensor

- Applications. *Synth. Met.* **2011**, *161*, 2355–2360.
- (71) Yakuphanoglu, F.; Gunduz, B. Effects of Channel Widths, Thicknesses of Active Layer on the Electrical and Photosensing Properties of the 6,13-Bis(triisopropylsilylethynyl) Pentacene Transistors by Thermal Evaporation Method: Comparison Study. *Synth. Met.* **2012**, *162*, 1210–1239.
- (72) Jurchescu, O. D.; Baas, J.; Palstra, T. T. M. Electronic Transport Properties of Pentacene Single Crystals upon Exposure to Air. *Appl. Phys. Lett.* **2005**, *87*, 052102.
- (73) Li, Z.; Wang, W.; Greenham, N. C.; McNeill, C. R. Influence of Nanoparticle Shape on Charge Transport and Recombination in Polymer/nanocrystal Solar Cells. *Phys. Chem. Chem. Phys.* **2014**, *16*, 25684–25693.
- (74) Jin, Z.; Wang, J. PIN Architecture for Ultrasensitive Organic Thin Film Photoconductors. *Sci. Rep.* **2014**, *4*, 5331.
- (75) Baek, E.; Pregl, S.; Shaygan, M.; Römhildt, L.; Weber, W. M.; Mikolajick, T.; Ryndyk, D. A.; Baraban, L.; Cuniberti, G. Optoelectronic Switching of Nanowire-Based Hybrid Organic/oxide/semiconductor Field-Effect Transistors. *Nano Res.* **2015**, *8*, 1229–1240.
- (76) Grollman, R. R.; Shepherd, W. E. B.; Robertson, A.; Paudel, K. R.; Anthony, J. E.; Ostroverkhova, O. Photophysics of Organic Semiconductors: From Ensemble to the Single-Molecule Level. *Proc. SPIE*, **2015**, *8*, 93600V.
- (77) Vollmer, A.; Jurchescu, O. D.; Arfaoui, I.; Salzmann, I.; Palstra, T. T. M.; Rudolf, P.; Niemax, J.; Pflaum, J.; Rabe, J. P.; Koch, N. The Effect of Oxygen Exposure on Pentacene Electronic Structure. *Eur. Phys. J. E* **2005**, *17*, 339–343.
- (78) Li, S.; Meng Lin, M.; Toprak, M. S.; Kim, D. K.; Muhammed, M. Nanocomposites of Polymer and Inorganic Nanoparticles for Optical and Magnetic Applications. *Nano Rev.* **2010**, *1*, 5214.
- (79) Andrew N. Shipway Eugenio Katz, I. W. Nanoparticle Arrays on Surfaces for Electronic, Optical, and Sensor Applications. *ChemPhysChem* **2000**, *1*, 18–52.
- (80) Schmid, G. Large Clusters and Colloids. Metals in the Embryonic State. *Chem. Rev.* **1992**, *92*, 1709–1727.
- (81) Toshima, N.; Yonezawa, T. Bimetallic Nanoparticles—novel Materials for Chemical and Physical Applications. *New J. Chem.* **1998**, 1179-1201.
- (82) Ahmadi, T. S.; Wang, Z. L.; Green, T. C.; Henglein, A.; El-Sayed, M. A. Shape-

- Controlled Synthesis of Colloidal Platinum Nanoparticles. *Science*, **1996**, 272, 1924 -1925.
- (83) Park, Y. S.; Chung, S.; Kim, S. J.; Lyu, S. H.; Jang, J. W.; Kwon, S. K.; Hong, Y.; Lee, J. S. High-Performance Organic Charge Trap Flash Memory Devices Based on Ink-Jet Printed 6,13-Bis(triisopropylsilylethynyl) Pentacene Transistors. *Appl. Phys. Lett.* **2010**, 96, 213107.
- (84) Banerjee, S.; Bülz, D.; Reuter, D.; Hiller, K.; Zahn, D. R. T.; Salvan, G. Light-Induced Magnetoresistance in Solution-Processed Planar Hybrid Devices Measured under Ambient Conditions. *Beilstein J. of Nanotechnol.*, **2017**, 8, 1502–1507.
- (85) Fert, A. The Present and the Future of Spintronics. *Thin Solid Films* **2008**, 517, 2–5.
- (86) Parkin, S.; Member, S.; Jiang, X. I. N.; Kaiser, C.; Panchula, A.; Roche, K.; Samant, M. Magnetically Engineered Spintronic Sensors and Memory. *Proc. of the IEEE*, **2003**, 91.
- (87) Makarov, A.; Windbacher, T.; Sverdlov, V.; Stamps, R. L.; Breikreutz, S.; Åkerman, J. Low-Power Non-Volatile Spintronic Memory: STT-RAM and beyond. *J. Phys. D: Appl. Phys.* 46 (**2013**) 074003 (10pp).
- (88) Iba, S.; Saito, H.; Spiesser, A.; Watanabe, S.; Jansen, R.; Yuasa, S.; Ando, K. Spin Accumulation and Spin Lifetime in P-Type Germanium at Room Temperature. *Applied Physics Express* 5 (**2012**) 053004.
- (89) Suzuki, T.; Sasaki, T.; Oikawa, T.; Shiraishi, M.; Suzuki, Y.; Noguchi, K. Room-Temperature Electron Spin Transport in a Highly Doped Si Channel. *Applied Physics Express* 4 (2011) 023003.
- (90) Wang, F. J.; Xiong, Z. H.; Wu, D.; Shi, J.; Vardeny, Z. V. Organic Spintronics : The Case of Fe / Alq 3 / Co Spin-Valve Devices. *Synth. Met.*, 155 (**2005**) 172–175.
- (91) Parkin, S. S. P.; Li, Z. G.; Smith, D. J. Giant Magnetoresistance in antiferromagnetic Co/Cu multilayers. *Appl. Phys. Lett.* **58**, 2710 (1991).
- (92) Dieny, B.; Speriosu, V. S.; Metin, S.; Parkin, S. S. P.; Gurney, B. A.; Baumgart, P.; Wilhoit, D. R. Magnetotransport Properties of Magnetically Soft Spin-Valve Structures (Invited) *Journal of Applied Physics* 69, 4774 (**1991**).
- (93) Baibich, M. N.; Broto, J. M.; Fert, a.; Van Dau, F. N.; Petroff, F.; Eitenne, P.; Creuzet, G.; Friederich, a.; Chazelas, J. Giant Magnetoresistance of

- (001)Fe/(001)Cr Magnetic Superlattices. *Phys. Rev. Lett.* **1988**, *61*, 2472–2475.
- (94) Binasch, G.; Grünberg, P.; Saurenbach, F.; Zinn, W. Enhanced Magnetoresistance in Layered Magnetic Structures with Antiferromagnetic Interlayer Exchange. *Phys. Rev. B.*, **1989**, *39*, 4828–4830.
- (95) Dediu, V.; Murgia, M.; Maticotta, F. C. C.; Taliani, C.; Barbanera, S. Room Temperature Spin Polarized Injection in Organic Semiconductor. *Solid State Commun.* **2002**, *122*, 181–184.
- (96) Xiong, Z. H.; Wu, D.; Vardeny, Z. V.; Shi, J. Giant Magnetoresistance in Organic Spin-Valves. *Nature* **2004**, *427*, 821–824.
- (97) Petta, J. R.; Slater, S. K.; Ralph, D. C. Spin-Dependent Transport in Molecular Tunnel Junctions. *Phys. Rev. Lett.*, *93*, 13, **2004**, 136601(4).
- (98) Wang, T. X.; Wei, H. X.; Zeng, Z. M.; Han, X. F.; Hong, Z. M.; Shi, G. Q. Magnetic / Nonmagnetic / Magnetic Tunnel Junction Based on Hybrid Organic Langmuir-Blodgett films. *Appl. Phys. Lett.* *88*, 242505, **2006**.
- (99) Wagemans, W.; Koopmans, B. Spin Transport and Magnetoresistance in Organic Semiconductors. *Phys. Status Solidi B* *248*, No. 5, 1029–1041 (**2011**).
- (100) Jiang, J. S.; Pearson, J. E.; Bader, S. D. Absence of Spin Transport in the Organic Semiconductor Alq₃. *Phys. Rev. B.*, *77*, 035303, **2008**.
- (101) Mermer, Ö.; Veeraraghavan, G.; Francis, T. L.; Wohlgenannt, M. Large Magnetoresistance at Room-Temperature in Small-Molecular-Weight Organic Semiconductor Sandwich Devices. *Solid State Commun.* **2005**, *134*, 631–636.
- (102) Mermer, Ö.; Veeraraghavan, G.; Francis, T. L.; Sheng, Y.; Nguyen, D. T.; Wohlgenannt, M.; Köhler, A.; Al-Suti, M. K.; Khan, M. S. Large Magnetoresistance in Nonmagnetic π -Conjugated Semiconductor Thin Film Devices. *Phys. Rev. B* **2005**, *72*, 205202.
- (103) Francis, T. L.; Mermer, O. ; Veeraraghavan, G.; Wohlgenannt, M. Large Magnetoresistance at Room Temperature in Semiconducting Polymer Sandwich Devices. *New J. Phys.* **2004**, *6*, 1–8.
- (104) Zhang, S.; Rolfe, N. J.; Desai, P.; Shakya, P.; Drew, A. J.; Kreouzis, T.; Gillin, W. P. Modeling of Positive and Negative Organic Magnetoresistance in Organic Light-Emitting Diodes. *Phys. Rev. B.*, *86*, 075206, **2012**, 75206.
- (105) Reichert, T.; Saragi, T. P. I. Photoinduced Magnetoresistance in Organic Field-Effect Transistors. *Appl. Phys. Lett.* **2011**, *98*, 2–4.

- (106) Reichert, T.; Saragi, T. P. I. Photoinduced Negative Magnetoresistance in 6,13-Bis(triisopropylsilylethynyl)-Pentacene Field-Effect Transistors. *Org. Electron.* **2012**, *13*, 377–383.
- (107) Bloom, F. L.; Wagemans, W.; Kemerink, M.; Koopmans, B. Separating Positive and Negative Magnetoresistance in Organic Semiconductor Devices. *Phys. Rev. Lett.* **2007**, *99*, 1–4.
- (108) Martin, J. L.; Bergeson, J. D.; Prigodin, V. N.; Epstein, a. J. Magnetoresistance for Organic Semiconductors: Small Molecule, Oligomer, Conjugated Polymer, and Non-Conjugated Polymer. *Synth. Met.* **2010**, *160*, 291–296.
- (109) Niedermeier, U.; Vieth, M.; Pätzold, R.; Sarfert, W.; Seggern, H. Von; Enhancement of Organic Magnetoresistance by Electrical Conditioning. *Appl. Phys. Lett.* *92*, 193309 (**2008**).
- (110) Bagnich, S. A.; Niedermeier, U.; Melzer, C.; Sarfert, W.; Von Seggern, H. Origin of Magnetic Field Effect Enhancement by Electrical Stress in Organic Light Emitting Diodes. *J. Appl. Phys.* **2009**, *105*.
- (111) Sheng, Y.; Nguyen, T. D.; Veeraraghavan, G.; Mermer, Ö.; Wohlgenannt, M.; Qiu, S.; Scherf, U. Hyperfine Interaction and Magnetoresistance in Organic Semiconductors. *Phys. Rev. B - Condens. Matter Mater. Phys.* **2006**, *74*, 45213.
- (112) Bobbert, P. A.; Wagemans, W.; Oost, F. W. A. Van; Koopmans, B.; Wohlgenannt, M. Theory for Spin Diffusion in Disordered Organic Semiconductors. *Phys. Rev. Lett.*, *102*, **2009**, 156604, 1–4.
- (113) Bobbert, P. A. Organic Semiconductors: What Makes the Spin Relax? *Nat Mater* **2010**, *9*, 288–290.
- (114) Nguyen, T. D.; Sheng, Y.; Wohlgenannt, M.; Anthopoulos, T. D. On the Role of Hydrogen in Organic Magnetoresistance : A Study of C₆₀ Devices. *Synth. Met.* **2007**, *157*, 930–934.
- (115) Bobbert, P. a.; Nguyen, T. D.; Van Oost, F. W. a; Koopmans, B.; Wohlgenannt, M. Bipolaron Mechanism for Organic Magnetoresistance. *Phys. Rev. Lett.* **2007**, *99*, 1–4.
- (116) Wagemans, W.; Bloom, F. L.; Bobbert, P. A.; Wohlgenannt, M.; Koopmans, B.; A Two-Site Bipolaron Model for Organic Magnetoresistance. *Journal of Applied Physics* *103*, 07F303 (**2008**).
- (117) Prigodin, V. N.; Bergeson, J. D.; Lincoln, D. M.; Epstein, A. J. Anomalous

- Room Temperature Magnetoresistance in Organic Semiconductors. *Synth. Met.* **2006**, *156*, 757–761.
- (118) Bergeson, J. D.; Prigodin, V. N.; Lincoln, D. M.; Epstein, A. J. Inversion of Magnetoresistance in Organic Semiconductors. *Phys. Rev. Lett.*, *100*, **2008**, 67201.
- (119) Desai, P.; Shakya, P.; Kreouzis, T.; Gillin, W. P. Magnetoresistance in Organic Light-Emitting Diode Structures under Illumination. *Phys. Rev. B*, *76*, 235202 **2007**.
- (120) Ern, V; Merrifield, R. E. Magnetic Field Effect on Triplet Exciton Quenching in Organic Crystals. *Phys. Rev. Lett.* **1968**, *21*, 609–611.
- (121) Johnson, R. C.; Merrifield R. E. Effects of Magnetic Fields on the Mutual Annihilation of Triplet Excitons in Anthracene Crystals. *Phys. Rev. B*, *1*, *2* **1970**, 896-902.
- (122) Buelz, D. Development of a Hall Measurement Substrate for Organic Semiconductors, *TU Chemnitz*, **2018**.
- (123) Kang, H.; Lee, I. J; Yoon, C. S. Sign Change in the Organic Magnetoresistance of Tris (8-Hydroxyquinolinato) Aluminum upon Annealing. *Appl. Phys. Lett.* *100*, 073302 (**2012**)

List of figures

Figure 1.1 (a) Representation of the structure for band transport. If the overlap between molecules is strong enough, the overlap of bonding and anti-bonding π orbitals leads to the formation of energy bands formed by a quasi-continuum of states. (b) Representation of the structure for hopping transport. In an amorphous material disorder leads to a dispersion of localized states. Transport occurs by hopping and it is assisted by phonons. Figure adapted from ref.³¹.

Figure 1.2 Schematic diagram of vertical and planar type hybrid electronic device structures.

Figure 2.1 Schematic of the fabrication process flow for fabricating nanostencils and how the nanostencil is used for fabricating nanostructured patterns on substrates. Figure adapted from ref.².

Figure 2.2 Schematic of thermal nanoimprint lithography process. T_g denotes the glass transition temperature of the thermoplastic polymer.

Figure 2.3 Schematic representation of the device architectures of conventional planar device (left) and HED-TIE (right).

Figure 2.4 Schematic representation of the fabrication process flow of the HED-TIEs using “trench refill approach”. Figure taken from ref.⁴⁰.

Figure 2.5 XSEM image of fabricated HED-TIEs with (a) solution processed TIPS-pentacene channel and (b) thermally evaporated H_2Pc channel. Figure taken from ref.⁴⁰.

Figure 2.6 XSEM image of fabricated structures with two types of trench refill oxide layer:

(a) thermally grown SiO_2 layer and (b) LPCVD SiO_x layer.

Figure 2.7 Molecular structure of metal free phthalocyanine molecule. Figure adapted from ref.⁵²

Figure 2.8 Photograph of an array of HED-TIE structures with gold electrodes. The inset shows scanning electron microscopic top-view of a HED-TIE with $W = 30 \mu m$ and channel length $L = 210 \text{ nm}$, after the evaporation of a nominal 300 nm phthalocyanine film thickness. Figure taken from ref.⁴⁰.

Figure 2.9 Molecular structure of TIPS-pentacene.

Figure 2.10 Comparison of the Raman spectra of the TIPS-pentacene powder and the drop-coated film (excitation wavelength used: 514.7 nm). Figure taken from ref.⁴⁰.

Figure 2.11 Photograph of a silicon chip with an array of gold TIE structures prior to deposition of the organic film. The inset shows an optical microscopic image of a fabricated device with channel width $W = 40 \mu\text{m}$ and channel length $L = 210 \text{ nm}$ after drop-coating with TIPS-pentacene solution. Figure taken from ref.⁴⁰.

Figure 2.12 Schematic illustration of “trench-refill approach” (left) and “spacer approach” (right) for fabricating HED-TIEs. In “trench refill approach”, the electrode gap is determined by the thickness of the trench refill layer. In “spacer approach”, an APCVD oxide layer is used to alter the hard mask geometry for reducing the electrode gaps even before the trenches are etched.

Figure 2.13 Schematic representation of the fabrication process flow of the HED-TIEs using “spacer approach”.

Figure 2.14 XSEM image of fabricated HED-TIE structure using spacer approach, prior to deposition of the organic channel.

Figure 2.15 XSEM image of HED-TIE structure with thermally grown SiO_2 isolation layer: (a) zoomed in view of the trench opening and (b) complete view of fabricated HED-TIE structure.

Figure 2.16 XSEM image of the trench opening after deep etching of silicon is carried out, showing the notches at the trench opening.

Figure 2.17 XSEM image of HED-TIE structure with LPCVD SiO_x isolation layer: (a) zoomed in view of the trench opening and (b) complete view of fabricated HED-TIE structure.

Figure 2.18 XSEM image of HED-TIE structure with APCVD SiO_x isolation layer: (a) zoomed in view of the trench opening and (b) complete view of fabricated HED-TIE structure.

Figure 3.1 Dependence of the current density (J), on the applied voltage (V), for Al/SnCl₂Pc/Al devices at various thicknesses of SnCl₂Pc. Figure taken from ref.⁶³.

Figure 3.2 Dependence of the current density (J), on the applied voltage (V), for H₂Pc samples of different thickness (a) 138, (b) 201, (c) 253 and (d) 312 nm. Figure taken from ref.⁵⁰.

Figure 3.3 Characteristic shape of J - V plot of ITO/CuPc/Al devices exhibiting SCLC conduction. Figure taken from ref.⁶⁴.

Figure 3.4 The schematic of the device layout of the HED-TIE devices.

Figure 3.5 The schematic of transport channels of the HED-TIE devices with interdigitated electrodes showing a device with single finger (left) and a device with multiple fingers (right).

Figure 3.6 The current-voltage characteristics of solution processed TIPS-pentacene based HED-TIEs for devices with 120 nm and 300 nm transport channels. The channel width for both devices is kept at 40 μm .

Figure 3.7 The $\log(J)$ vs $\log(V)$ plot of solution processed TIPS-pentacene based HED-TIEs indicating trap dominated SCLC conduction.

Figure 3.8 The current density (J) vs. $1/L^3$ (where L = device channel length) plot for TIPS-pentacene based devices with channel width of 40 μm . The dotted line indicates the expected behaviour assuming space charge limited current conduction.

Figure 3.9 The current-voltage characteristics of HED-TIEs with thermally evaporated H_2Pc transport channels. The channel length is varied as 120 nm, 170 nm, 210 nm, 250 nm and 300 nm whereas the channel width for all devices is kept at 30 μm .

Figure 3.10 The $\log(J)$ vs $\log(V)$ plot of HED-TIEs with thermally evaporated H_2Pc as channel materials. The curves were found to exhibit a slope >2 , indicating trap dominated SCLC conduction.

Figure 3.11 The current density (J) vs. $1/L^3$ (where L = device channel length) plot for H_2Pc based devices with channel width of 30 μm . The dotted line indicates the expected behaviour assuming space charge limited current conduction.

Figure 3.12 Current-voltage characteristics of solution processed TIPS-pentacene based interdigitated HED-TIEs for devices with 100 nm, 150 nm and 200 nm transport channels. The large channel width of all devices (5000 μm) was realised by using interdigitated electrodes with 100 finger structures of 50 μm each.

Figure 3.13 Current-voltage characteristics of solution processed TIPS-pentacene based HED-TIEs for devices with 50 μm , 500 μm and 5000 μm channel widths. The channel length for all the devices is 100 nm. The current is found to scale linearly with the device channel widths as shown in the inset.

Figure 4.1 The output characteristics of the TIPS-pentacene-OTFT transistor (a) under UV and (b) comparison of the dark and UV conditions at various gate voltages. Figure taken from ref.⁷.

Figure 4.2 The output characteristics of the TIPS-pentacene-OTFT transistor (a) under 100 mW/cm^2 white light illumination and (b) comparison of the dark and white light illumination conditions at $V_g = -6$ V. Figure taken from ref.⁷.

Figure 4.3 UV-Vis spectra of a TIPS-pentacene film drop-coated on quartz substrate.

Figure 4.4 Schematic diagram of the photosensing experiments. The active channel of the fabricated HED-TIE is illuminated from top. Figure taken from ref.⁴⁰.

Figure 4.5 (a) Photocurrent density (J_{ph}) plotted over the applied voltage for three different laser lines. (b)-(d) J_{ph} over time at a constant bias voltage of 0.5 V, while the illumination was switched on and off every 30 s. Illumination wavelengths used are (b) 632.8 nm, (c) 514.7 nm, and (d) 325 nm. Figure taken from ref.⁴⁰.

Figure 4.6 The variation of the time constant with the excitation wavelength. (a) τ_1 (the time constant responsible for the instantaneous device response) vs wavelength and (b) τ_2 (the time constant representing the slower photocurrent decay due to trapping and de-trapping of the carriers vs wavelength).

Figure 4.7 The photoluminescence spectra of the TIPS-pentacene channel. Excitation wavelength is 325 nm. A laser beam with the power of 180 μ W was focused on the HED-TIE channel using a 10x objective. Initial PL measurements were carried out in N_2 ambient followed by air and N_2 ambient again. Figure taken from ref.⁴⁰.

Figure 4.8 The area under PL spectra plotted over time to show the decay in PL intensity while the channel material is exposed to air. Figure taken from ref.⁴⁰.

Figure 4.9 Size distribution of the synthesized gold nanoparticles.

Figure 4.10 Absorption spectra of: (a) gold nanoparticles and (b) TIPS-pentacene. The green and red lines indicate the laser lines used for the photosensing experiments.

Figure 4.11 Exemplary current-voltage characteristics of TIPS-pentacene based HED-TIEs with and without gold nanoparticles in the channel.

Figure 4.12 Current-voltage characteristics of TIPS-pentacene based HED-TIEs diluted in ethanol for two different configurations of the voltage terminals.

Figure 4.13 Current-voltage characteristics in dark and under red and green illumination: (a) TIPS-pentacene based HED-TIE, (b) TIPS-pentacene based HED-TIE with Au NP_1, (c) TIPS-pentacene based HED-TIE with Au NP_2 and (d) HED-TIE with TIPS-pentacene solution diluted in ethanol.

Figure 4.14 J_{ph} over time for TIPS-pentacene based HED-TIE at a constant bias voltage of 1 V, while the illumination was switched on and off every 30 s. Illumination wavelengths used are (a) 632.8 nm and (b) 514.7 nm.

Figure 4.15 J_{ph} over time for TIPS-pentacene based HED-TIE, with TIPS-pentacene diluted in ethanol, at a constant bias voltage of 1 V, while the illumination was switched

on and off every 30 s. Illumination wavelengths used are (a) 632.8 nm and (b) 514.7 nm.

Figure 4.16 J_{ph} over time for TIPS-pentacene based HED-TIE with Au NP_1 in the channel matrix, at a constant bias voltage of 1 V, while the illumination was switched on and off every 30 s. Illumination wavelengths used are (a) 632.8 nm and (b) 514.7 nm.

Figure 4.17 J_{ph} over time for TIPS-pentacene based HED-TIE with Au NP_2 in the channel matrix, at a constant bias voltage of 1 V, while the illumination was switched on and off every 30 s. Illumination wavelengths used are (a) 632.8 nm and (b) 514.7 nm.

Figure 5.1 (a) LSMO/6T/LSMO planar spintronic device as published by Dediu *et al.* in ref. [12]. Electron beam lithography was used for patterning electrode gap dimensions of 100 – 500 nm. (b) Magnetoresistance as a function of device channel length at applied magnetic field of 0.3 T. Figures taken from ref.⁹⁵.

Figure 5.2 (a) Magnetoconductance in TIPS-Pentacene OFET recorded at VDS = -2 V and VG = 0 V, measured under illumination and external magnetic field (60 mT). (b) Zoomed in view of part 1 showing the dark current measured under influence of magnetic field. (c) Zoomed in view of part 2 showing the photocurrent measured under influence of magnetic field. (d) The corresponding photocurrent change when the light is kept on. Figures taken from ref.¹⁰⁶.

Figure 5.3 The spin of a polaron on a pentacene molecule interacting with the hyperfine fields from the hydrogen nuclei (illustrated by arrows). The polaron spin precesses around the sum of hyperfine fields from surrounding hydrogen nuclei and the external magnetic field. Figure adapted from ref.⁹⁹.

Figure 5.4 Illustration of the particle interactions that are considered in the different OMAR models. Figure taken from ref.⁹⁹.

Figure 5.5 (a, b) Illustration of spin-blocking in bipolaron. Two particles with parallel spins cannot form an intermediate bipolaron. (c, d) Illustration of spin precession of two neighbouring spins in (c) only the local hyperfine fields B_{hf} and (d) in the total field B_{tot} , the sum of the local hyperfine field and the external field B. (e, f) Corresponding energy diagrams. (e) Without an external field, the hyperfine field mixes the singlet S and all three triplets, T_+ , T_0 , and T_- . (f) An external field Zeeman splits the triplets. Mixing occurs only between S and T_0 . Figure taken from ref.⁹⁹.

Figure 5.6 Diagram of possible routes for recombination of free electrons and holes to the ground state, by first forming an e–h pair which turns into an exciton. The different transitions are explained in the text. Figure adapted from ref.⁹⁹.

Figure 5.7 Schematic diagram of the experimental setup: (a) Commercial bottom contact OFET substrates (b) Planar device structure with trench isolated electrodes (HED-TIE). Figure taken from ref.⁸⁴.

Figure 5.8 Light switching behaviour of TIPS-pentacene based (a) organic field effect transistor (OFET) and (b) hybrid electronic device with trench isolated electrodes (HED-TIE). Light induced magnetoresistance in TIPS-pentacene obtained from both types of planar devices: (c) OFET and (d) HED-TIE device. Figure taken from ref.⁸⁴.

Figure 5.9 (a) Light switching of OFET prepared by drop-coating of TIPS-pentacene diluted in water. The inset shows absence of the magnetoresistance in such an OFET. (b) Degraded light switching behaviour of a TIPS-pentacene HED-TIE after two days of exposure to the ambient atmosphere. The inset shows the response to applied magnetic field. Figure taken from ref.⁸⁴.

Figure 5.10 (a) Output characteristics of TIPS-pentacene OFET. (b) Output characteristics of an OFET prepared from same TIPS-pentacene solution, diluted in water (1:1). Figure taken from ref.⁸⁴.

Figure 5.11 Output characteristics of the TIPS-pentacene based HED-TIE device, measured for freshly prepared sample and after two days of sample preparation. Figure taken from ref.⁸⁴.

Figure 5.12 Comparison of OMAR magnitude in TIPS-pentacene based HED-TIE devices with two different channel lengths. The sample surface was illuminated with white light LED. Both devices have channel width of 40 μm and channel lengths of (a) 200 nm and (b) 300 nm.

List of tables

Table 4.1 Summary of the photosensing properties of the TIPS-pentacene HED-TIEs of two different channel lengths and under three different single wavelength illumination. All the J_{ph} mentioned are measured at a fixed bias of 0.5 V.

Table 4.2 Summary of the photosensing properties of the TIPS-pentacene HED-TIEs with and without gold nanoparticles in the channel matrix and under two different single wavelength illumination. All the J_{ph} mentioned are measured at a fixed bias of 1 V.

List of abbreviations

UV	Ultraviolet
HED	Hybrid electronic devices
TIE	Trench isolated electrodes
HED-TIE	Hybrid electronic devices with trench isolated electrodes
H₂Pc	Metal free phthalocyanine
TIPS-pentacene	6,13-bis(triisopropylsilylethynyl) pentacene
Si	Silicon
GaAs	Gallium Arsenide
OLED	Organic light emitting diodes
OFET	Organic field effect transistors
OPV	Organic photovoltaics
OSC	Organic semiconductors
HOMO	Highest unoccupied molecular orbital
LUMO	Lowest unoccupied molecular orbital
OTFT	Organic thin film transistor
EBL	Electron beam lithography
NSL	Nanostencil lithography
NIL	Nanoimprint lithography
LPCVD	Low pressure chemical vapour deposition
PECVD	Plasma enhanced chemical vapour deposition
APCVD	Atmospheric pressure chemical vapour deposition
MEMS	Microelectromechanical systems
2D	Two dimensional
SiN	Silicon nitride
KOH	Potassium hydroxide
SiO₂	Silicon dioxide
SiO_x	Silicon oxide
SF₆	Sulphur hexafluoride
C₄F₈	Octafluorocyclobutane
CF₄	Tetrafluoromethane
HF	Hydrofluoric acid
STS	Surface Technology Systems
Cr	Chromium
SEM	Scanning electron microscopy
XSEM	Cross-sectional scanning electron microscopy
AFM	Atomic force microscopy
SCLC	Space charge limited current
SnCl₂Pc	Tin (IV) phthalocyanine dichloride
ITO	Indium tin oxide
CuPc	Copper phthalocyanine
Al	Aluminium

List of abbreviations

Au	Gold
Ca	Calcium
I-V	Current-voltage
J-V	Current density-voltage
CdSe	Cadmium selenide
P3HT	Poly(3-hexylthiophene)
PL	Photoluminescence
N₂ ambient	Nitrogen ambient
UV-Vis	Ultraviolet-visible
Au NP	Gold nanoparticles
TP	TIPS-pentacene
MR	Magnetoresistance
GMR	Giant magnetoresistance
TMR	Tunnelling magnetoresistance
OMAR	Organic magnetoresistance
OSPD	Organic spintronic device
6T	Sexithiophene
LSMO	Lanthanum strontium manganite
Alq₃	Tris (8-hydroxyquinolato) aluminium
PPV	Poly (p-phenylene vinylene)
C₆₀	Carbon-60
MC	Magnetoconductance
LED	Light emitting diodes
MoS₂	Molybdenum disulphide
WSe₂	Tungsten diselenide
POM	Polyoxymethylene

Acknowledgements

I am grateful to Prof. Dr. Dietrich R. T. Zahn for giving me the opportunity to do my Ph.D in the Semiconductor Physics group of Chemnitz University of Technology. A special thanks to him for being so supportive throughout my studies and for believing in me.

I would like to thank my supervisor, Prof. Dr. Georgeta Salvan, for her never-ending support and constant guidance which helped me to go through various ups and downs during the entire phase of my Ph.D. She has not only been a great supervisor but also a friend, philosopher and guide in every possible way. Her guidance made me evolve as a better researcher as well as a better human being.

I would like to thank Dr. Danny Reuter for supervising the device fabrication part of this dissertation. It was him who gave me the opportunity to be a part of the DFG project “Towards Molecular Spintronics” five years back. I started working as a student research assistant during my MSc and continued since then in this research unit. I can never forget that Dr. Danny Reuter and Prof. Dr. Karla Hiller gave me the opportunity to work with them, knowing I was partially crippled back then. It definitely gave me the strength and confidence I needed to complete my studies, fighting against my chronic illness.

A special thanks goes to Prof. Dr. Carsten Deibel for his valuable inputs about the electrical characterization part. I remember having long discussions with him, asking stupid questions but he always answered all of my doubts with a smile on his face.

I would like to thank Mr. Daniel Bülz for developing the software for the electrical measurements, for helping me with the graphics of experimental set up and for being always there with me, whenever I needed to have long discussions about some experimental results or, for fixing broken experimental setups.

I would like to thank Mr. Falk Schwenzer, Mr. Michael Rennau, Mr. Patrick Schwarz and Mrs. Cornelia Kowol for helping me with the wafer handling during fabrication processes, the electrical test measurements, the wafer dicing and wire-bonding and SEM imaging, respectively.

I would like to thank Dr. Volodymyr Dzhagan and Mr. Dmytro Solonenko for helping me with the Raman measurements whenever needed.

I would like to thank our lab engineer, Mr. Axel Fechner, for helping me with fixing the equipment whenever something went wrong.

Acknowledgements

I would like to thank Mrs. Sybille Raschke and Mrs. Jane Eisentraut for helping me with all the administrative paperwork throughout my Ph.D.

I would like to thank Alexandra Raevskaya for providing gold nanoparticle dispersions from University of Kiev, Ukraine which was used for a part of the work described in this dissertation.

I express my sincere gratitude to all the people working at the Fraunhofer ENAS, Center for Microtechnologies (ZfM) and Institute of Physics of Chemnitz University of Technology, who contributed in some way to this work.

I am grateful to group of Prof. Eugenio Coronado from University of Valencia for helping us with exploring other possible applications of HED-TIEs by using 2D flakes as channel materials.

I am thankful for the financial support provided by Deutsche Forschungsgemeinschaft Reseach Unit FOR 1154 "Towards Molecular Spintronics" to support me during my Ph.D studies.

I can never forget the support I have received from all of our research group members (our HLPH family) throughout my stay in this group. You all have truly been a family, far away from my family and hometown. I really enjoyed the time I spent in this group. Thanks to my friends Jing Guo, Jana Kalbacova and Constance Schmidt for making the most frustrating times a lot easier to go through.

I would like to thank my parents for what I am today. Even though I grew up in a remote corner of India, they always taught me to dream big since my childhood days. The most important lesson which I learned from them is, "NEVER GIVE UP". I would like to thank my sister for her constant support in every possible way, whenever I needed it. Last but not the least, thanks to Sandeep, my husband. Sandeep, you are the one who had to take all the frustrations whenever experiments did not work or when I felt home-sick or whatever. You happily compromised the most beautiful phase of our married life staying 10,000 km away from each other, so that I can accomplish my dream of finishing my doctoral studies. I know it was not easy for any of you to allow me to stay alone, knowing my health condition. Thank you for believing in me, for giving me the unconditional love which helped me to build up the confidence to fight against all odds, to overcome all challenges thrown at me by my "fibromyalgia" and for repeatedly making me believe "I CAN DO IT".

List of Publications

- S. Banerjee, D. Bülz, D. Solonenko, D. Reuter, C. Deibel, K. Hiller, D. R. T. Zahn and G. Salvan, “HED-TIE: A wafer-scale approach for fabricating hybrid electronic devices with trench isolated electrodes”, *Nanotechnology* **28** (2017) 195303 (9pp)
- S. Banerjee, D. Bülz, D. Reuter, K. Hiller, D. R. T. Zahn and G. Salvan, “Light induced magnetoresistance in solution processed planar hybrid devices measured under ambient conditions”, *Beilstein Journal of Nanotechnology* 2017, **8**, 1502-1507
- A. G. Milekhin, O.P. Cherkasova, S.A. Kuznetsov, I.A. Milekhin, E.E. Rodyakina, A.V. Latyshev, S. Banerjee, G. Salvan, D.R.T. Zahn, “Nanoantenna-assisted plasmonic enhancement of IR absorption by vibrational modes of organic molecules” *Beilstein Journal of Nanotechnology* 2017, **8**, 975–981
- S. Banerjee, D. Bülz, D. Reuter, K. Hiller, D. R. T. Zahn and G. Salvan, “Modified HED-TIE: Introduction of spacers for better geometrical control of the fabricated hybrid electronic devices with trench isolated electrodes”, *manuscript to be submitted to IOP Nanotechnology*
- S. Banerjee, P. F. Siles, V. Dzaghan, N. Uhlig, A. Khalladi, T. Ruffer, H. Lang, M. Devarajulu, O. G. Schmidt, G. Salvan, D.R.T. Zahn, “Improvement of device performance after chemical purification of commercially available cobalt phthalocyanine molecules”, *manuscript to be submitted to Beilstein Journal of Nanotechnology*

List of Conference Presentations and Posters

- S. Banerjee, D. Bülz, D. Reuter, V. Dzhagan, A. Raevskaya, C. Deibel, K. Hiller, D. R. T. Zahn and G. Salvan, *“Tunable photosensing properties of hybrid trench devices using Au nanoparticles in TIPS-pentacene matrix”*, ICSFS 2016, Chemnitz, Germany
- D. Bülz, S. Banerjee, D. Reuter, D. R. T. Zahn and G. Salvan, *“Photoelectrical characterization of lateral four terminal organic devices”*, ICSFS 2016, Chemnitz, Germany
- A. Milekhin, L. Sveshnikova, S.A. Kuznetsov, E.E. Rodyakina, I.A. Milekhin, A.V. Latyshev, O.P. Cherkasova, S. Banerjee, G. Salvan and D.R.T. Zahn, *“Surface-enhanced Raman Scattering and Infrared Absorption by Thin Organic Layers on Arrays of Au Nanoantennas”* ECOF 2015, Genova, Italy
- S. Banerjee, D. Bülz, D. Solonenko, D. Reuter, C. Deibel, K. Hiller, T. Gessner, D. R. T. Zahn and G. Salvan, *“Photosensitive organic-inorganic hybrid trench devices for sensor applications”*, 13th ECME 2015, Strasbourg, France
- D. Bülz, F. Lüttich, S. Banerjee, D. R. T. Zahn, G. Salvan, *“The influence of morphology and interface treatment in 6,13-bis(triisopropylsilylethynyl)-pentacene field-effect transistors”* ICOE2015, Paris, France
- S. Banerjee, D. Bülz, D. Reuter, K. Hiller, T. Gessner, D. R.T. Zahn, and G. Salvan, *“Phthalocyanines/Au-hybrid trench devices, a comparative study of solution processed and thermally evaporated molecular channels”* DPG-Frühjahrstagung 2015, TU Berlin
- D. Bülz, S. Banerjee, D. R. T. Zahn and G. Salvan, *“The influence of magnetic fields on organic field effect transistors under illumination”* DPG-Frühjahrstagung 2015, TU Berlin
- S. Banerjee, P. Richter, D. Bülz, O.D. Gordan, D. Reuter, K. Hiller, T. Geßner, D.R.T. Zahn, G. Salvan, *“Trench technology—an alternative approach for fabricating laterally stacked hybrid devices”*, Elecmol 14, Strasbourg, France, 2014

- S. Banerjee, P. Richter, D. Bülz, D. Reuter, K. Hiller, T. Gessner, D. R.T. Zahn, and G. Salvan, "*Organic lateral spin devices fabricated by trench technology*", DPG-Frühjahrstagung 2014, TU Dresden
- P. Richter, S. Banerjee, C. Schulze, D. Reuter, K. Hiller, M. Albrecht, D. R.T. Zahn and G. Salvan, "*Magneto-optical characterization of organic/inorganic heterostructures for lateral spintronic devices*" OSI 10, Chemnitz, Germany, 2013

Selbstständigkeitserklärung

Ich erkläre, dass ich die vorliegende Arbeit selbständig und nur unter Verwendung der angegebenen Literatur und Hilfsmittel angefertigt habe.

Chemnitz, den 11.12.2017

Sreetama Banerjee

MSc. Sreetama Banerjee

Curriculum Vitae

SREETAMA BANERJEE

Date of Birth 05.09.1986
Place of Birth Raghunathganj, India
Nationality Indian

Education

Chemnitz University of Technology, Saxony, Germany

Doctor of Philosophy, Natural Science March 2014 – December 2017

- Dept.: Physics
- Thesis Title: *HED-TIE: A wafer-scale approach for fabricating hybrid electronic devices with trench isolated electrodes and its application in sensing devices.*

Chemnitz University of Technology, Saxony, Germany

Master of Science (Micro and Nano Systems) October 2011- February 2014

- Dept.: Electrical Engineering and Information Technology
- German Grade Points- 1.9
- Master's Thesis: *Laterally stacked organic trench devices for magnetoresistive sensors.*

Heritage Institute of Technology, WBUT, Kolkata, India

Bachelor of Technology (Electronics & Communication Engg.) August 2004 - June 2008

- Grade Points- 8.14
- Bachelor's Thesis: *Development of an automatic lift based on logic gates.*

Academic Qualification

STANDARD / SCHOOL	BOARD	YEAR OF PASSING	PERCENTAGE
12 th , B. R. D. Sen H.S. School	WBCHSE	2004	82.0%
10 th , Raghunathganj Girls' H.S. School	WBBSE	2002	84.5%